miss

by Ridhima Sharma

Submission date: 12-Jan-2026 02:10AM (UTC+0530)
Submission ID: 2855174452
File name: plag_report_final.docx (25.01M)
Word count: 27807
Character count: 160203

Abstracts

Chapter-1

This chapter provides an overview of adsorption and semiconductor photocatalysis as effective strategies for wastewater treatment, with a focus on fly ash–TiO_2–metal–zeolite hybrid materials. It discusses the environmental impact of industrial effluents and the drawbacks of conventional remediation technologies. The chapter highlights the role of fly ash as an inexpensive, porous support, its functionalization with TiO_2 to enhance photocatalytic activity, and subsequent performance improvements achieved through metal doping and zeolite incorporation. A critical review of recent studies illustrates how these components work synergistically to broaden light absorption, and enhance charge separation, and improve catalyst durability for degrading dyes. Methods for material synthesis, structural and optical characterization, and performance evaluation are summarized. The chapter concludes by identifying existing research gaps and emphasizing the need for advanced hybrid composites capable of achieving superior efficiency under visible and solar light irradiation.

Chapter-2

This study emphasizes the need to achieve both high photocatalytic efficiency and strong adsorption capacity in a catalyst to ensure complete removal of fuchsine blue dye (FB) from wastewater. In this work, TiO_2 and fly ash–TiO_2 composites (0.5–5wt%) were prepared using a sol–gel method combined with wet impregnation, and their performance was evaluated for combined processes of adsorption and photocatalytic degradation of fuchsin blue dye. The materials were characterized using XRD, UV–DRS, SEM, EDS, Raman spectroscopy, and N_2 adsorption analysis. Adsorption and degradation experiments were conducted to evaluate the effects of pH (2–10), adsorbent dosage (1–9 mg), contact time (30–180 min), and initial dye concentration (5–30 mg/L) on FB dye removal efficiency. Among the tested samples, the 5wt% fly ash–TiO_2 composite exhibited the highest adsorption capacity of 20.32 mg/g and achieved 76% FB dye removal. These results indicate that adsorption occurs primarily through monolayer coverage on a homogeneous surface, consistent with the Langmuir isotherm, and proceeds according to pseudo-first-order kinetics. Under UV irradiation, the same 5wt% fly ash–TiO_2 composite reached a maximum photocatalytic degradation of 88% after 180 minutes, following pseudo-first-order kinetics. The catalyst demonstrated excellent reusability, maintaining its dye removal performance consistent over five consecutive cycles.

Chapter-3

In this study, copper (Cu) photo-deposited fly ash-TiO_2 composites (FT-$Cu_{0.5-2}$) with Cu content ranging from 0.5 to 2wt% were synthesized to evaluate their adsorption and photocatalytic activity toward the degradation of fuchsin blue (FB) dye under visible light as well as natural sunlight. Structural characterization was performed using X-ray diffraction (XRD) and diffuse reflectance spectroscopy (DRS), while morphological and surface chemical analyses were carried out through high-resolution transmission electron microscopy (HR-TEM), X-ray photoelectron spectroscopy (XPS), and N_2 adsorption Brunauer-Emmett-Teller (BET) analysis. These confirmed the successful fabrication of fly ash-TiO_2 (FT) and Cu-modified composites (FT-$Cu_{0.5-2}$). Copper nanoparticles, with sizes in range between 7 and 17 nm, were uniformly distributed on the FT composite surface. The impact of various adsorption parameters, including FB dye concentration, adsorbent dose, solution pH, and contact duration was systematically investigated. Following 180 minutes of adsorption in the dark, the 1wt% Cu-loaded FT composite (FT-Cu_1) showed the highest dye removal efficiency of 77% and fitted well to the Langmuir adsorption model. A notable enhancement in photocatalytic activity was observed for FT-Cu_1, which achieved 92% FB degradation under sunlight and 94% under visible light, compared to the unmodified FT catalyst with only 68% and 71% removal, respectively. This enhancement in removal efficiency is attributed to the synergistic interaction between Cu, fly ash, and TiO_2 components. The presence of Cu improved the separation of photogenerated electron-hole pairs and broadened visible light absorption by introducing intermediate energy states within the TiO_2 bandgap. The degradation pathway of FB dye was elucidated via trapping experiments using hole scavengers and detection of intermediate species through High-Resolution Mass Spectrometry (HRMS). Additionally, the FT-Cu composite exhibited strong photostability and could be reused effectively, maintaining approximately 83% degradation efficiency after five consecutive cycles, demonstrating its potential for sustainable treatment of organic contaminants.

Chapter-4

In this work, copper photo-deposited fly ash–TiO_2 (FT-Cu_1) composites were modified with ZSM-5 zeolite at loadings of 1%, 3%, and 5% by weight, designated as 1ZFT-Cu_1, 3ZFT-Cu_1, and 5ZFT-Cu_1, respectively. These composites were investigated for their capability to adsorb and photo catalytically degrade crystal violet (CV) dye under visible and solar light exposure. Characterization techniques including UV-Vis diffuse reflectance spectroscopy (DRS), field emission scanning electron microscopy (FE-SEM), X-ray diffraction (XRD), and BET surface

area analysis revealed that the addition of ZSM-5 enhanced crystallinity, minimized particle aggregation, and improved visible light absorption of the composites. Among the samples, the 3wt% ZSM-5-loaded composite (3ZFT-Cu_1) exhibited the best photocatalytic performance, achieving dye removal efficiencies of 98% under visible light and 95% under solar irradiation, using a catalyst dosage of 5 mg, initial dye concentration of 5 mg/L, a contact time of 180 minutes, and solution pH 9. The adsorption process fitted well with the Freundlich isotherm model, indicating multilayer adsorption, while the degradation kinetics followed a pseudo-first-order rate. The superior activity is credited to the synergistic interaction of copper doping, the porous structure of ZSM-5, and the fly ash support, which collectively enhanced light absorption and dye uptake. The 3ZFT-Cu_1 composite also showed commendable stability, retaining 84% of its degradation efficiency after five cycles of reuse. Free radical trapping studies using hole scavengers elucidated the photocatalytic degradation pathway of CV dye, highlighting the composite's effectiveness under visible light for potential wastewater treatment application.

Chapter-1

Introduction and literature review

1.1 Introduction

Rapid technological advancements and transformations in human lifestyles have greatly accelerated the emergence of intricate environmental and social issues. To lessen these negative effects, it is now crucial to develop prompt and efficient remedial techniques. The increasing demand for water, caused by industrialisation, agricultural development, and population growth, has increased wastewater output, demanding good resource management [1]. The pervasive increase in pollution has become a serious global issue that is negatively damaging the marine environment and people's health [2]. Improper treatment of industrial effluents generated from diverse sectors such food and beverage processing, paper and pulp manufacturing, textiles, dyeing, and chemical industries has resulting in the continuous discharge of large volumes of contaminated wastewater into natural water bodies, streams, and rivers [3]. Dyes, owing to their complex chemical structures, pose a substantial threat to aquatic ecosystems, with adverse effects on human health, as well as plant and animal life [4]. Some synthetic dyes are known to negatively affect vital organs such as the kidneys, liver, heart, brain, nerve system, skin, and certain compounds within this group may also act as mutagens or carcinogens. Several physical, chemical, and biological approaches have been developed to mitigate water pollution [5,6]. Methods that are very effective in eliminating big particles and solids include coagulation [7], membrane filtration, biofiltration [8], and electrochemical oxidation [9]. However, their high operating costs and the requirement for proper secondary waste management prevent these methods from being widely used. Among the emerging alternative techniques, adsorption and photocatalytic degradation have gained significant prominence[10]. These techniques have garnered significant interest due to their eco-friendly nature, high reproducibility, and effectiveness in eliminating persistent organic contaminants[11].

1.1.1 Adsorption & Photocatalytic Degradation

Adsorption is extensively employed because of its straightforward operation, cost-effectiveness, and excellent removal efficiency [12]. Various materials, including activated carbon[13], zeolites[14], fly ash [15], and lignocellulose-based substances[16], have demonstrated remarkable performance in water purification processes. However, adsorption faces key limitations, including the requirement for adsorbent regeneration, challenges in managing secondary waste, and a reduction in performance after multiple cycles of reuse [17]. Unlike adsorption, photocatalytic degradation facilitates the breakdown of organic contaminants under sunlight exposure, effectively minimizes the generation of secondary waste[18]. Widely investigated photocatalytic materials comprise ZnO [19], WO_3 [20], g-C_3N_4 [21], and a range of TiO_2-based semiconductors that have been doped or structurally modified to enhance their performance. The synergistic integration of adsorption and photocatalysis offers an efficient strategy for removing organic pollutants. Initially, pollutants are adsorbed onto the material, preventing photocatalyst surface fouling. Upon light exposure, photocatalysis then mineralizes the adsorbed contaminants into harmless byproducts like CO_2 and H_2O, regenerating the catalyst surface and enhancing long-term efficiency and sustainability [22].

1.1.2 Utilization of fly ash as support

Fly ash, a waste product from coal combustion, is increasingly recognized as a low-cost and widely available support material in pollution control technologies. The synergy of its porosity, high surface area, and reactive surface sites makes it an excellent host matrix for binding photocatalytic and adsorptive materials [23]. Fly ash serves as an effective support material, promoting better dispersion, enhanced durability, and improved reusability of active agents such as TiO_2, ZnO, and metal nanoparticles. Its aluminosilicate structure provides good ion-exchange capacity and mechanical stability under different environmental conditions. Employing fly ash in this role not only boosts the effectiveness of contaminant removal processes but also contributes to sustainable material reuse and environmental conservation [24].

1.1.3 Limitations of fly in pollutant removal

Although fly ash holds considerable potential for pollutant removal, its practical application is limited by several challenges. A major concern is the risk of releasing toxic metals and other harmful substances inherently present in raw fly ash, which can introduce secondary

contamination. Furthermore, inconsistencies in its physicochemical properties such as composition, particle size, and surface morphology due to variations in fuel type and combustion conditions, may lead to unpredictable treatment performance. In its unmodified form, fly ash often exhibits limited adsorption efficiency for certain contaminants, necessitating chemical or physical activation to improve its functionality. These modifications, however, can increase both the operational complexity and overall treatment cost. Additional issues such as difficulty in recovering the material after treatment, reduced effectiveness over repeated cycles, and the need for environmentally sound disposal methods also pose significant barriers to its large-scale use in wastewater treatment[24,25].

1.1.4 Fly ash-TiO_2 (FT) composite for improved photocatalytic activity

The combination of titanium dioxide (TiO_2) with fly ash has gained attention as an effective method to enhance photocatalytic efficiency and mitigate the individual shortcomings of both materials. TiO_2 is a well-established photocatalyst due to its high oxidative strength, chemical inertness, and capability to degrade various organic contaminants under light irradiation[26]. Nevertheless, its practical deployment faces several constraints, including limited surface area, rapid recombination of photogenerated charge carriers, and challenges in post-treatment separation.

Utilizing fly ash as a supporting material for TiO_2 (shown in **Scheme 1.1**), addresses many of these limitations. The inherent porosity and extensive surface area of fly ash promote uniform dispersion of TiO_2 particles, which improves light utilization and interaction with pollutants. Immobilizing TiO_2 on the fly ash matrix also enhances catalyst durability, reduces nanoparticle aggregation, and facilitates recovery and reuse[27]. Additionally, the naturally occurring metal oxides and silica in fly ash may further aid in photocatalytic efficiency by assisting in charge separation or acting as co-active sites[28]. The resulting composite harnesses both the adsorption potential of fly ash and the photocatalytic power of TiO_2, presenting a cost-effective and environmentally friendly solution for treating wastewater contaminated with recalcitrant organic compounds.

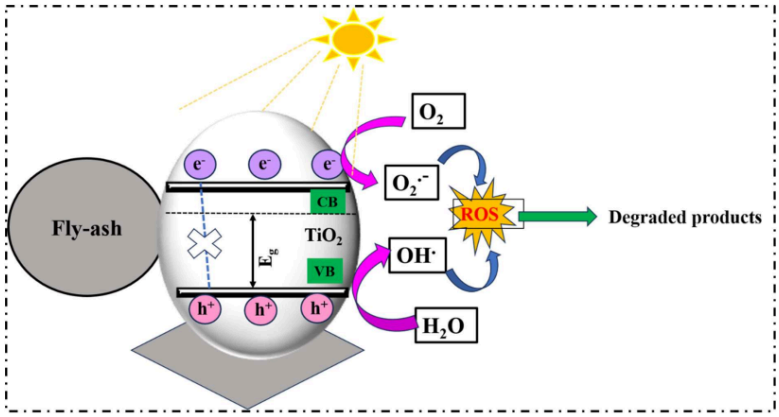

Scheme 1.1 A schematic illustration of the photocatalytic mechanism over fly ash-TiO_2 (FT) Composite

1.1.5 Cu photo-deposited fly ash-TiO_2 composite (FT-Cu) for Visible-Light Activation

Metal doping of fly ash–TiO_2 composites (shown in **Scheme 1.2**) offers a compelling strategy to boost photocatalytic efficiency under visible light irradiation. Since pristine TiO_2 is primarily active under UV light due to its wide band gap (~3.2 eV), introducing transition metals like Cu, Fe, Ag, or Ni can create intermediate electronic states that facilitate visible-light activation [29–31] Among these, copper stands out by forming Cu^{+}/Cu^{2+} redox pairs, which enhance charge separation and act as effective electron traps, thereby minimizing recombination. Additionally, copper's strong affinity with TiO_2 and its economic viability make it more favorable than many other dopants [32]. Supporting the composite on fly ash further enhances surface area, improves TiO_2 dispersion, and provides structural durability. Together, the adsorption properties of fly ash, the oxidative degradation ability of TiO_2, and the extended light responsiveness from metal doping create a synergistic system for efficient pollutant removal under ambient light conditions.

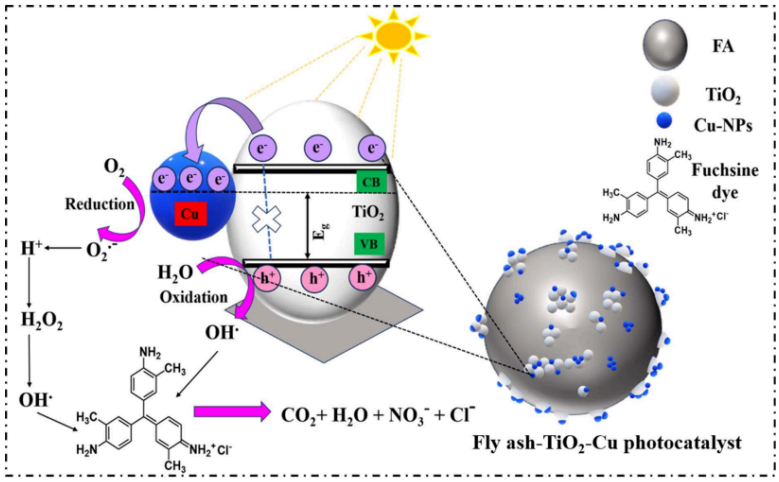

Scheme 1.2 The proposed mechanism of fuchsin blue dye degradation by copper doped fly ash-TiO_2 (FT-Cu) under visible-solar light**.**

1.1.6 Zeolite (ZSM-5) modified fly ash-TiO_2-metal (ZFT-Cu) composite

In the development of multifunctional materials for environmental remediation, the addition of zeolites to composite systems has garnered considerable attention. The integration of zeolites, particularly ZSM-5, into fly ash–TiO_2–metal composites significantly augment their photocatalytic and adsorptive efficiency. ZSM-5, known for its high surface area, well-organized microporous framework, and strong ion-exchange capacity, facilitates the accumulation of pollutants near the reactive sites, thereby increasing contact efficiency [33]. Its presence in the composite promotes enhanced dispersion of TiO_2 and metal dopants while maintaining structural porosity for improved light penetration. Additionally, the acidic nature and cation-exchange properties of ZSM-5 can influence the electronic characteristics of the composite, aiding in better charge carrier separation and redox reactions. This synergistic effect contributes to improved catalytic performance, structural stability, and long-term reusability under solar or visible-light-driven pollutant degradation conditions [34].

The synthesis of multifunctional hybrid composites combining fly ash, TiO_2, metal dopants, and zeolites has emerged as an effective approach for addressing complex water pollution challenges. Each component plays a complementary role: fly ash acts as a porous [35], low-cost support that enhances the dispersion and anchoring of active photocatalytic materials; TiO_2

serves as the core semiconductor, capable of generating reactive species for pollutant degradation. However, pure TiO_2 exhibits photocatalytic activity predominantly under UV irradiation owing to its wide bandgap, and its efficiency is further limited by the rapid recombination of photogenerated charges [36, 37]. To address these limitations, metal doping especially with elements like Cu is employed to induce localized energy states inside the band structure, hence improving visible light absorption.

Incorporating ZSM-5 zeolites into the fly ash-TiO_2-Cu composite further improves the efficiency of the composite by offering a high surface area, uniform pore distribution, and strong adsorption capacity. These properties enable effective concentration of pollutants near catalytic sites and contribute to improved light penetration and mass transfer [38]. (shown in **Scheme 1.3**).

Overall, this synergistic material design not only improves the degradation of recalcitrant organic pollutants in wastewater but also supports sustainable remediation strategies by utilizing industrial byproducts like fly ash. Such hybrid systems are promising candidates for practical applications in wastewater treatment, especially under visible or solar light conditions.

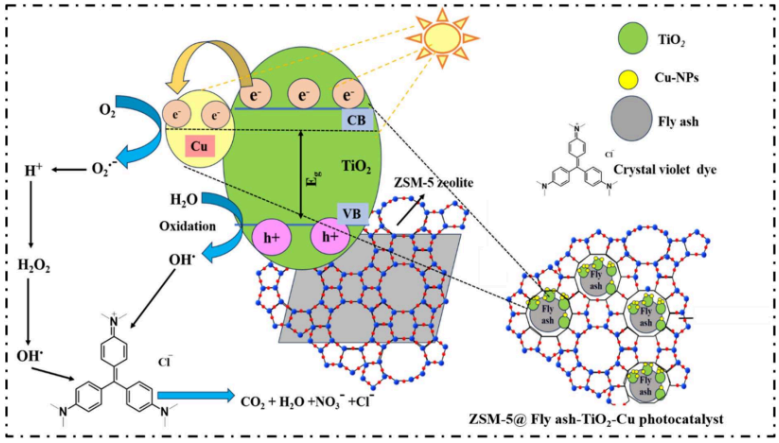

Scheme 1.3 The photocatalytic degradation mechanism of crystal violet dye by ZFT-Cu composite.

1.1.7 Literature Survey

A wide range of studies has reported the application of fly ash–TiO_2 composites, metal-doped fly ash–TiO_2 systems, and zeolite-modified fly ash–TiO_2 composites for the adsorption and photocatalytic removal of various pollutants, including dyes, antibiotics, pesticides, and pharmaceuticals. Representative findings from these studies are summarized in **Table 1.1.**

Mpelane et al.[39] prepared a C–TiO_2–coal fly ash (CFA) nanocomposite using the sol–gel method, followed by immobilization onto a polyacrylonitrile (PAN) membrane through phase inversion. The incorporation of carbon and the high specific surface area of the composite (114 m^2/g) contributed to its outstanding photocatalytic efficiency. When tested under sunlight for 300 minutes, the material achieved degradation rates of 99.8% for methyl orange (MO) and 99.2% for gentian violet (GY), highlighting its potential for solar-driven wastewater treatment.

Tu et al.[40] developed a fly ash cenosphere (FAC)-supported TiO_2 composite using a wet mechanical grinding method, enabling even distribution of nano-TiO_2 across the FAC surface. This photocatalyst effectively removed 98% of methyl orange from aqueous solutions and performed on par with commercial P25 TiO_2, all while utilizing a reduced amount of TiO_2. The study highlights its potential as a more economical and efficient option for real-world wastewater treatment applications**.**

Sawunyama et al. [41]synthesized a cost-effective ceramic membrane by modifying coal fly ash with TiO_2 and ZnO through co-pressing and sintering techniques. The resulting composite showed notable photocatalytic activity under visible light, removing around 77% of tetracycline within 100 minutes. It also maintained about 73% of its efficiency after five consecutive cycles, highlighting its durability and potential for repeated use. The synergistic integration of ZnO and TiO_2 onto the fly ash matrix improved both light harvesting and charge separation, making it a viable and sustainable option for eliminating antibiotics from contaminated water sources.

Song et al. [42]synthesized a floating photocatalyst by incorporating iron (Fe) and nitrogen (N) co-doped TiO_2 onto fly ash cenospheres through a sol–gel process. The Fe–N–TiO_2/FAC composite exhibited notable photocatalytic activity under visible light, achieving 92.6% degradation of Rhodamine B in 6 hours. The co-doping effectively broadened the light absorption spectrum and enhanced charge separation efficiency.

Lin and Ali[43] synthesized a Fe^{3+}-doped ZnO/TiO_2 photocatalyst using the calcination method for dye removal. The optimized composite achieved 90.68% removal of methyl orange under

incandescent light and 97.14% under sunlight after 4 hours, demonstrating high photocatalytic efficiency.

Visa et al.[44] produced a Pt/TiO_2–fly ash zeolite composite using a mild hydrothermal synthesis. The material was applied for industrial dye removal, achieving about 25% removal of Brilliant Blue and 43.9% of brilliant red under sunlight in 360 minutes, which increased to 80.7% and 93.4%, respectively, when H_2O_2 was added.

Aghajari et al.[45] developed a nanocomposite photocatalyst comprising Ag-doped Fe–ZSM-5 supported on TiO_2 through a combination of hydrothermal synthesis and sol–gel methods. This multifunctional material was tailored for the degradation of Reactive Red 195 (RR195) dye under natural sunlight exposure. The inclusion of silver and iron into the ZSM-5@TiO_2 framework enhanced the photocatalyst's surface characteristics and light absorption in the visible region. Under optimized conditions (pH 3 and 400 mg/L dosage), the system achieved around 98% degradation of RR195 within 2 hours, while maintaining effective performance over several reuse cycles.

Cahyanti et al. [46] synthesized an Fe-doped TiO_2/zeolite H-A composite via the impregnation method to enhance photocatalytic performance. The incorporation of Fe into the TiO_2/zeolite structure improved light absorption and charge separation efficiency. When applied for methylene blue degradation under UV irradiation, the photocatalyst achieved approximately 89.6% removal within 50 minutes, demonstrating its high efficiency for dye wastewater treatment.

Sambakanya et al. [47] synthesized a carbon-doped TiO_2–SnO_2 nanocomposite supported on coal fly ash (C-TiO_2-SnO_2/CFA) via a sol-gel method subsequently calcined at 550 °C. The photocatalyst was applied for dye degradation, achieving 97.75 % removal of methyl orange and 99.25 % removal of methylene blue within 3 h under visible light.

Raashid et al.[48] synthesized a dual-catalyst system comprising TiO_2 as a photocatalyst and Fe-coated 4 Å zeolite as an ozonation catalyst for the degradation of CONFIDOR pesticide (imidacloprid). Under UV irradiation (253.7 nm, 250 W/m²) and an ozone flow rate of 100 mg/h, the combined catalytic process achieved over 99 % removal of imidacloprid within 20 minutes, demonstrating a 1.4-fold higher degradation rate compared to TiO_2 alone.

Ramutshatsha-Makhwedzha et al. [49] prepared a magnetic Fe_3O_4@TiO_2@zeolite nanocomposite using a sol–gel method, combining the magnetic properties of Fe_3O_4 for easy separation, the adsorption ability of TiO_2, and the high surface area and ion-exchange capacity of zeolite. The material was applied for the removal of levofloxacin from water, achieving a

removal efficiency of 92.43–96.95 % and maintaining good reusability up to five adsorption–desorption cycles.

Mergenbayeva et al.[50] prepared TiO_2/zeolite (TZ) and TiO_2/ZSM-5 (TZSM) composites via mechanical mixing and impregnation for SMX degradation, achieving 100 % removal in 10 min under UV light with a rate constant of 0.501 min^{-1} (2.08× higher than TiO_2) and ~67 % mineralization within 120 min.

Li et al. [51] synthesized a CTAB-modified Mo-doped TiO_2 coated on fly ash cenosphere (CTAB-Mo-TiO_2/FAC) via a sol–gel method. The photocatalyst showed an extended absorption range (200–800 nm) and abundant oxygen vacancies, enabling enhanced visible-light activity. At a dosage of 2 g/L, it achieved 99.75 % removal of methylene blue (MB) within 60 min, compared to 42 % for Mo-TiO_2/FAC and 24 % for TiO_2/FAC.

Kanakaraju et al. [52] prepared a copper-doped TiO_2/fly ash composite (Cu–TiO_2/FA) using adsorption–photocatalysis synergy, optimized via response surface methodology. Under visible light, at 2 g/L dosage and 5 ppm methyl orange (MO), it achieved 99.91 % removal of MO in 100 min, demonstrating a "capture-and-destroy" mechanism.

Gong et al. [53] developed an Ag-nanoparticle embedded magnetic fly ash composite (AgNPs/MCFA) by impregnation–reduction–sintering. Under visible light, it removed 99.89 % methyl orange in 15 min, with degradation rate constant k = 0.3133 min^{-1}, and retained >90 % efficiency after five reuse cycles.

Table 1.1 Summary of recent studies on fly ash-supported photocatalysts for dye and pollutant degradation under various light sources.

S. No.	Photocatalyst	Pollutant(s)	Source of Light	Degradation / Removal Efficiency	Ref.
1	TiO_2-doped mesoporous silica (TDMS) from CFA	Rhodamine B, Acid Orange II	Not specified	99.9% (RhB), 99.9% (AOII) in 6 h; TOC removal 90.3% / 84.1%	[54]
2	TiO_2/ZSM-5 (Z-T, 450 °C)	Methyl orange (MO)	UV light	~99%	[55]
3	Na-Y/TiO_2–Pd	Methylene blue (MB)	Visible light	> 98%	[56]
4	NaP-zeolite@TiO_2 sheets	Methylene blue (MB)	Solar light	99.6% in 2 h; > 90% COD reduction	[57]
5	Fe-TiO_2/BEA zeolite	Tetracycline	Visible light	100% in 90 min (3 wt% Fe)	[58]

S. No.	Photocatalyst	Pollutant(s)	Source of Light	Degradation / Removal Efficiency	Ref.
			(50 W blue LED)		
6	CdS/TiO_2/CeO_2 on zeolite	Methylene blue (MB)	71 Visible light	~99.9% (synthetic); ~78.7% (sewage); ~86% retained after 4 cycles	[59]
7	TiO_2/HZSM-5	Methyl orange (MO)	UV light	82.4% after 3 reuse cycles	[60]
8	X-zeolite/TiO_2 from CFA	Methylene blue (MB)	71 Visible light	98.36% (0.36 g/L, 30 min adsorption + 100 min photocatalysis)	[61]
9	TiO_2–zeolite composites (from CFA)	Methyl orange (MO)	UV light	82.4%	[62]
10	TiO_2-modified fly ash (MFA)	Cd(II), Pb(II)	Adsorption (no light)	94.3% (Cd), 93.1% (Pb)	[63]
11	Fe-TiO_2/HY zeolite	Methylene blue (MB)	Visible light	> 98% (10 wt% Fe-TiO_2/HY); UV degradation with TiO_2/HY	[64]
12	TiO_2-N/zeolite-NaY	Methylene blue (MB)	UV light	Up to 99% in 3 h	[65]
13	Z@Ag/TiO_2	Cd^{2+} adsorption	Not specified	~99% (198 mg/L Cd^{2+}); ~168 mg/L adsorption capacity	[66]
14	CuO/Ag-zeolite (CAZ)	Methylene blue (MB)	Not specified	~99% (0.10 CAZ); 70.4 mg g^{-1} adsorption; antibacterial vs. *S. aureus*	[67]
15	TiO_2/Fe_2O_3/zeolite	Cyanide	UV/H_2O_2	89% (zeolite); 97% (PAC); 1.3× faster rate	[68]
16	TiO_2 + Fe-zeolite (ozonation)	Acid Red 1 dye	UV/O_3	95% in 9 min (5 min with Fe-zeolite); TiO_2 alone 28% in 15 min	[69]
17	Cu-TiO_2/zeolite/PMMA tablets	Methylene blue (MB)	Simulated solar	21% degradation (240 min); zeolite/PMMA adsorbed 69% MB	[70]
18	TiO_2/clinoptilolite	Crystal violet	Not specified	89% in 100 min (pseudo-first-order kinetics)	[71]
19	TiO_2/zeolite	Malachite Green	UV light	82–66% adsorption; 92–	[72]

S. No.	Photocatalyst	Pollutant(s)	Source of Light	Degradation / Removal Efficiency	Ref.
				90% combined removal	
20	Ag_2O@Y zeolite	Ranitidine	Simulated sunlight	97.5% in 75 min (neutral pH)	[73]

1.2 Research Gaps

Based on the literature survey, the following gaps have been identified:

1. Limited studies have explored the use of TiO_2–fly ash–metal–zeolite composites as adsorbent/photocatalyst is less commonly done.
2. Adsorbents/Photocatalysts like TiO_2-fly ash metals- nonmetals- have not been used much to remove these organic pollutants such as (antibiotics, EDCs, dyes etc).
3. Very few literatures are available on adsorptive removal of organic pollutants like EDCs and antibiotics using TiO_2-fly ash metal- zeolite composite.

1.3 Objectives

The main aim of this research is to develop and evaluate a range of adsorbents/photocatalysts for the removal of hazardous organic pollutants from aqueous solutions. The specific objectives are:

1. To synthesize and characterize fly ash–TiO_2 hetero-composites.
2. To investigate the effect of metal incorporation into fly ash–TiO_2 composites on their adsorption capacity and photocatalytic efficiency.
3. To assess the impact of zeolite incorporation into fly ash–TiO_2–metal composites on the photocatalytic degradation of organic contaminants.

1.4 Characterization of fly ash–TiO_2 hetero-composites.

Freshly prepared Copper-deposited fly ash–TiO_2 composites, and ZSM-5 zeolite-loaded fly ash–TiO_2–copper composites were characterized by different techniques such as XRD, FESEM, BET, DRS, XPS and Raman spectroscopy to evaluate their structural, morphological, optical, and surface properties, as outlined below.

1.4.1 X-ray diffraction (XRD) analysis

The crystal structure of the synthesized materials was examined using a Smart Lab SE X-ray diffractometer with Cu-Kα radiation (λ = 1.54 Å) as the source. The equipment was operated at 45 kV to provide sufficient X-ray intensity for clear diffraction peaks. Data collection was carried out within a 2θ range of 5° to 80°, allowing the detection of both low- and high-angle reflections. A slit width of 10 mm was used to maintain beam precision, while the step size was fixed at 0.01° to ensure high-resolution measurements. The scan rate was maintained at 5° per minute to obtain accurate and well-defined diffraction patterns for phase identification and structural analysis.

1.4.2 Morphological analysis

Field Emission Scanning Electron Microscopy (FESEM, JEOL JSM-7600F, Japan) operating at 30 kV was employed to examine the surface morphology and microstructural features of the prepared catalysts. The elemental composition and spatial distribution of elements were determined using Energy Dispersive Spectroscopy (EDS, Bruker). In addition, detailed lattice and particle structure were visualized through High-Resolution Transmission Electron Microscopy (HRTEM, JEOL JEM-2100, Japan).

1.4.3 Surface area and pore size analysis

The surface area and pore size characteristics of the prepared samples were determined using the Brunauer–Emmett–Teller (BET) method on an Autosorb iQ analyzer (Quantachrome Instruments, version 3.01, USA). Before measurement, the samples were subjected to vacuum degassing to eliminate any adsorbed gases or moisture, ensuring precise results. Nitrogen adsorption–desorption isotherms were obtained at 77 K (liquid nitrogen temperature), and the resulting data were used to calculate the specific surface area, mean pore diameter, and total pore volume.

1.4.4 Optical absorption and band gap analysis

The optical properties of the synthesized samples were examined using a Diffuse Reflectance Spectrophotometer (JASCO V-750, Japan) to evaluate their light absorption behavior and band gap characteristics. Barium sulfate ($BaSO_4$) was employed as a reference standard due to its nearly perfect diffuse reflectance, ensuring precise baseline correction. The measurements were carried out over a wavelength range of 400–800 nm, covering the visible light spectrum. This enabled detailed analysis of absorbance and reflectance profiles, which were subsequently used to estimate the optical band gap energies of the samples through Tauc plot analysis.

1.4.5 XPS analysis

The oxidation states and chemical environments of the constituent elements in the composite were determined using X-ray Photoelectron Spectroscopy (XPS) on a Thermo Fisher Scientific NEXSA system (UK). The analysis was performed under ultra-high vacuum conditions, employing a monochromatic Al Kα X-ray source.

1.4.6 Raman analysis

Raman spectroscopy was carried out using a LabRAM HR micro-Raman spectrometer (Horiba) outfitted with a 532 nm laser for excitation.

1.5 Adsorption and photocatalytic studies

The adsorption and photocatalytic performance of the prepared fly ash–TiO_2, copper-deposited fly ash–TiO_2, and ZSM-5 zeolite–loaded fly ash–TiO_2–copper composites was evaluated by assessing their effectiveness in removing organic pollutants. The pollutant removal mechanism involves two successive stages:

1.5.1 Adsorption Studies

The adsorption capacity of the synthesized photocatalysts toward various organic pollutants was evaluated in the absence of light. A measured quantity of the photocatalyst was introduced into separate test tubes containing aqueous solutions of the target pollutants. These mixtures were stirred in dark conditions to avoid any photoreactions. At predetermined time intervals, samples were withdrawn and subjected to ultracentrifugation to isolate the catalyst particles. The concentration of residual pollutants in the supernatant was determined using a UV–visible spectrophotometer (JASCO V-750) by recording and comparing the absorption spectra before and after the adsorption process. To elucidate the adsorption mechanism, experimental data were fitted to the Langmuir and Freundlich isotherm models. Additionally, pseudo-first-order and pseudo-second-order kinetic models were applied to predict and analyze the adsorption kinetics. Detailed descriptions of the procedures, equations, and calculations are provided in the corresponding sections.

1.5.2 Photocatalytic Degradation Analysis

The photocatalytic degradation experiments for different pollutants were carried out in individual test tubes, each containing a known quantity of photocatalyst dispersed in 5–10 mL of the pollutant's aqueous solution. Prior to light exposure, the mixtures were stirred in the dark

to establish adsorption–desorption equilibrium at the interface between the catalyst surface and pollutant molecules. Subsequently, the samples were irradiated with visible LED light (50 W, WIPRO Garnett B22, intensity ~100 W/m², λ > 365 nm) housed within a wooden chamber. At predetermined intervals, aliquots were withdrawn, and the photocatalyst particles were removed via ultracentrifugation. The concentration of the remaining pollutants in the supernatant was determined using UV–visible spectroscopy. Photodegradation efficiency and kinetic parameters for each photocatalyst were calculated using the methods and equations described in the subsequent chapters. The reaction intermediates generated during the photocatalytic degradation were identified using high-resolution mass spectrometry (Waters QTOF mass spectrometer equipped with an XEVO G2 XS UPLC system and coupled to APCI and ESI ionization sources, 10 min retention time).

Chapter-2

Utilization of fly ash–TiO_2 composites for efficient adsorption and photodegradation of fuchsin blue dye

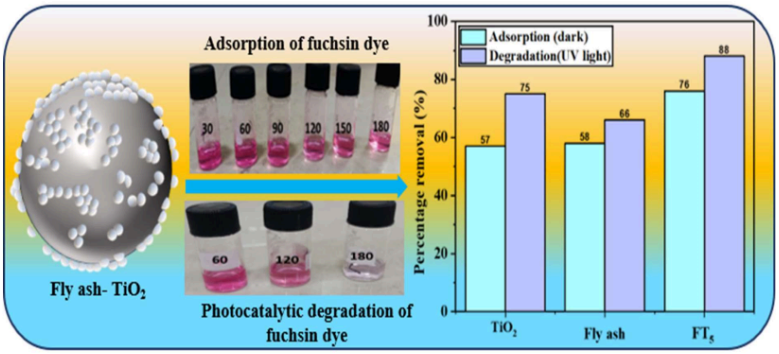

Schematic summary

2.1 Introduction

Coal power stations significantly meet the world's energy needs [1]. Fly ash is a solid waste produced in huge from the combustion of raw coal in power plants [2]. The amount of coal fly

ash produced annually is expected to be 750 million tonnes and is only used in some industries to the extent of 25% [1]. Coal fly ash is one of many industrial solid wastes (by-products) that are an attractive and low-cost adsorbent with good specific surface area, porosity, and particle size due to its ability to adsorb a variety of hazardous and non-biodegradable dyes from coloured effluents[3,4]. Fly ash is improperly handled, stored, and disposed which causes significant contamination to the earth, air, water, and even living creatures. The environment is contaminated, and human health is at risk when untreated fly ash from power plant chimneys is released into the atmosphere [5,6]. As a result, recycling fly ash has sparked a lot of interest in research scientists to find sustainable and environmentally friendly ways to deal with this waste product [7]. The composite material made up of fly ash and TiO_2 is reported to show improved photocatalytic properties [8–10]. The fly ash provides a large surface area for dye adsorption and accelerates photocatalytic processes when combined with TiO_2 nanoparticles. By incorporating fly ash, the composite photocatalyst becomes more durable and stable, increasing its capacity for reuse. The TiO_2 nanoparticles in the composite photocatalyst are activated when exposed to UV light [11,12]. The absorbed light energy creates electron-hole pairs in the TiO_2, leading to the generation of reactive oxygen species, such as superoxide radicals and hydroxyl radicals (•OH). The reactive oxygen species interact with the dye molecules that have been adsorbed, oxidizing them to generate smaller, less harmful chemicals [13,14]. Recent research on the production and application of photocatalysts has focused mostly on titanium dioxide (TiO_2) due to its exceptional performance, chemical stability, and lack of toxicity [15].

Over the last decades, FA/TiO_2 composites have been studied as an affordable adsorbent for eliminating different water pollutants during wastewater treatment [3,4]. Gilja et al.[13] synthesized TiO_2/ treated FA nanocomposites to increase the specific surface area for removing reactive Red 45 (RR45) azo dye via photocatalytic treatment with UV-A light. The study found that all FA1/TiB nanocomposite photocatalysts have high photosensitivity, with 96% of discolouration. Mpelane et al.[16] utilized the sol-gel technique to synthesize the C-TiO_2-CFA nanocomposite, which was then immobilized on a PAN membrane by the phase inversion method. Carbon doping and the nanocomposite's huge surface area (114 m^2/g) resulted in excellent photodegradation efficiency (99.8% and 99.2% for MO and GY, respectively) under sunlight irradiation, in 300 min. Tu et al. [14] employed a wet mechanical grinding approach to produce an FA-TiO_2 composite using nano TiO_2 and FACs to remove 98% methyl orange. Duta and Visa [17] effectively synthesized TiO_2/FA

novel substrate in a hydrothermal process for concurrent heavy metal (Cd^{2+} and Cu^{2+}) and surfactant (1- hexadecyl trimethylammonium bromide – HTAB and dodecyl benzenesulfonate – SDBS) elimination, optimised conditions led to excellent removal efficiency (over 90%) for heavy metals and surfactants. Kanakaraju [18] synthesized a Cu/TiO_2/FA composite using the wet impregnation method to achieve a 99% removal of methyl orange under visible light.

For instance, dyes are hazardous pollutants that must be removed [19]. Basic fuchsin (BF), or magenta or Fuchsin dye, is a synthetic dye from the triarylmethane class [20]. Although widely used in textile mills, the cationic dye is not biodegradable when disposed of with wastewater [21]. Releasing fuchsin dye into water will significantly harm the ecosystem and endanger human health [22]. Continuous exposure to this dye may result in headaches, vertigo, muscular cramps, disorders in the digestive system, gastrointestinal discomfort, nausea, and vomiting [23,24]. The dye's aromatic rings are extremely stable, which leads to considerable bioaccumulation. As a result, it is critical to eliminate it from the water using an easy, inexpensive, and efficient method [25]. Fuchsin removal from wastewater systems is a serious issue that needs to be researched and addressed because of its poor biodegradability, toxicity, carcinogenicity, and odour [26]. However, the adsorption and degradation of fuchsin dye by TiO_2-fly ash composite has not been reported anywhere.

The current studies describe the synthesis, characterization, comparative adsorption, and photocatalytic degradation of fuchsin dye by TiO_2, fly ash, and fly ash-TiO_2 composites. TiO_2 was synthesized using the sol-gel method, and FA-TiO_2 composites were prepared using the wet-impregnation method with TiO_2 concentrations ranging from 0.5 to 5wt%.

2.2 Experimental section

2.2.1 Chemicals and reagents

Titanium Butoxide $Ti(OC_4H_9)_4$, Di decyl dimethyl ammonium chloride ($C_{22}H_{48}ClN$) were purchased from Sigma-Aldrich (India), Acetic acid ($C_2H_4O_2$), Ethanol (C_2H_5OH), FB dye ($C_{20}H_{19}N_3.HCl$) were obtained from Loba Chemie (India). Fly ash (FA) was obtained from Rajpura Power Plant (India). Ultrafiltration equipment Milli-Q (Millipore) produced double-distilled water (D.I.).

2.2.2. Synthesis of TiO_2

TiO_2 was synthesized by the sol-gel method displayed in Scheme S1. Solution A was made by dissolving 10 mL of titanium butoxide in anhydrous ethanol. Under vigorous stirring (250

rpm), 10 mL of 3M acetic acid was added dropwise to the solution and agitated for another 15 minutes. At room temperature, 1.1 mL didecyl dimethyl ammonium chloride, 30 mL anhydrous ethanol, and 10 mL distilled water were combined for 15 min to get Solution B. Eventually, solution B was gradually added to solution A. The resulting mixture was then aggressively stirred with a magnetic stirrer at (600 rpm) for 45 minutes. The liquid in the Erlenmeyer flask was then cooked for an additional 24 h at 70°C in the oven, producing a clear solution. The resulting TiO_2 sample underwent a de-ionized water rinse, was dried at 100°C for 12 hours, and then was subjected to a 3 h calcination process at 400°C [13].

2.2.3 Synthesis of FA-TiO_2 (FT) Composites

FA-TiO_2 composites with different weight percentages of TiO_2 were prepared by the wet-impregnation method (shown in **Scheme 2.1**). 10g of fly ash was ultrasonically dispersed in a beaker containing 100 ml of distilled water. Then a specified amount of TiO_2 (0.05g, 0.1g, 0.3g and 0.5 g) was added. The mixture was stirred at 600 rpm for 2 h followed by filtration and drying in an oven at 70°C for 24 h. The FA-TiO_2 composite catalyst containing 0.5wt%, 1wt%, 3wt% and 5wt% of TiO_2 are named as $FT_{0.5}$, FT_1, FT_3 and FT_5 respectively [27].

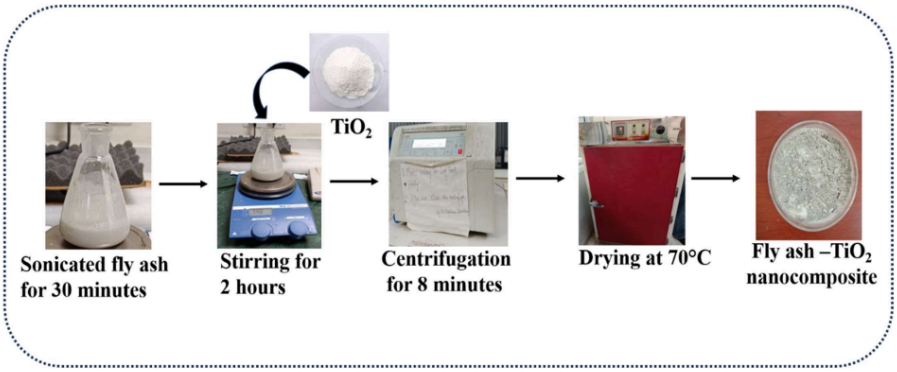

Scheme 2.1 Schematic presentation of the synthesis of the fly ash-TiO_2 nanocomposites.

2.2.4 Catalyst Characterization

The X-ray diffraction patterns of the synthesized materials were performed using an X-ray powder diffraction PAN Analytical-Xpert-PRO machine outfitted with a Cu-Kαradiation source (1.54), functioning at 45kV, with a diffraction angle (2θ) extending from 5°- 80° and a scan rate of 5°/min. Raman spectroscopic observations were conducted using a Labram HR,

Horiba micro-Raman spectrometer with a 532nm laser excitation. Surface area and porosity were determined using the BET N_2 adsorption-desorption isotherm at 77.3 K using a surface analyzer Quanta chrome Nova-1000. Furthermore, the BJH method was used to investigate pore size distribution. Field Emission Scanning Electron Microscopy (JEOL JSM-7600F operating at 30kV) (FESEM) was used to describe the surface morphology of the catalyst. Elemental mapping and analysis were done using an energy-dispersive X-ray spectrometer (EDS). Utilizing a reference of $BaSO_4$, the optical properties were assessed using a diffuse reflectance spectrophotometer (DRS, Avantes). High-Resolution Mass Spectroscopy (Waters, QTOF mass spectrometer equipped with XEVO G2 XS UPLC combined with APCI and ESI ionization source with negative and positive mode scans at various intervals, retention duration of 10 min) was employed to identify degradation products, which provided insightful information about the photocatalytic degradation pathway.

2.2.5 The point of zero charge (PZC) of composite

The point of zero charge is a significant physicochemical parameter since it shows the pH at which the adsorbent's surface will have zero net charge. The point zero charges of the FT_5 composite were computed using the solid addition technique using 0.002 M cetrimide ($C_{19}H_{42}Br_N$) and 0.1 M KCl solutions. In this approach, 25 mL of 0.002 M cetrimide and 25 mL of 0.1 M KCl solution were placed in test tubes, and the preliminary pH of the various solutions was roughly adjusted between 2 and 10 using 0.1 M NaOH and 0.1 M HCl solutions. Following that, 5 mg of FT_5 composite was added individually to each test tube, resulting in a suspension that was kept for 3 hours and allowed to equilibrate with constant shaking. After 3 hours, filter the solution and properly determine the ultimate pH. Figure S2 shows a graph that compares the change between the initial and final pH ($\Delta pH = pH_i - pH_f$) The point of zero charge was determined from the point of intersection.

2.2.6 Adsorption of FB dye

The adsorption behaviour of TiO_2, FA (Fly ash), and various FT composites (0.5wt%, 1wt%, 3wt, and 5wt% of TiO_2) was studied with a 10 ml pollutant solution. The effect of various parameters such as fuchsin dye concentration (5-30 mg/L) adsorbent amount (1-9 mg), and contact time (30-180) minutes was studied. In the dark, a magnetic stirrer was used to mix and agitate a series of test tubes containing 10 ml of pollutant solution at various concentrations and the required amount of adsorbent. After agitating each test tube for a specific period, it was removed, and 10 ml of its aqueous sample was taken and centrifuged to separate the adsorbent.

A UV-visible spectrophotometer was used to determine the amount of adsorbate in the supernatant at its maximum absorbance (λ_{max} = 546 nm for FB dye). The adsorbent's adsorption efficiency (adsorbed mass per unit mass, mg/ g) was determined by using the formula:

$$\text{Adsorption capacity} = Q_e = (C_o - C_e) \times \frac{V}{W} \quad (1)$$

where C_o denotes the initial concentration (mg/L) of fuchsin dye, C_e denotes the FBs equilibrium concentration in the solution (mg/L), W denotes the amount of adsorbent (g), V denotes the volume of FB solution (L) and Q_e is the adsorbent's efficiency (mg/g) at equilibrium [28] The following equation was used to estimate the percentage (R%) of FB absorbed into adsorbents.

$$\text{Percentage removal of FB dye} = R\% = \left(\frac{C_o - C_e}{C_o}\right) \times 100 \quad (2)$$

C_0 and C_e are the initial and equilibrium concentrations of the fuchsin dye in the solution, and R% is the percentage of the fuchsin dye that has been removed [29].

2.2.7 Photocatalytic degradation of FB dye

The photocatalytic activity of the synthesized materials TiO_2, FA and different TiO_2-FA nanocomposites were evaluated by FB dye degradation. The photocatalytic reaction was carried out in separate test tubes at room temperature; 5 mg of each catalyst was disseminated in 10 mL of FB solution in a typical reaction. The test tubes containing various catalysts were then subjected to UV light (125 W Hg arc, 104 mW/cm^2). After 150 minutes, the samples were removed from each test tube and centrifuged at 9000 rpm for 7 min to remove any residual solid catalyst particles. The optical absorbance spectra of FB dye were analyzed using a UV-vis spectrophotometer at λ_{max} of 546 nm. According to Beer- Lambert's law the concentration is directly proportional to the absorbance, and the following formula was used to calculate the photodegradation efficiency:

$$\text{Rate of FB dye degradation (\%)} = \frac{A_o - A_t}{A_o} \times 100 = \frac{C_o - C_t}{C_o} \times 100$$

(3)

where A_o, C_o stands for the initial FB dye absorbance and concentration at time 0 and A_t, C_t for the absorbance and concentration of FB dye at time t, respectively [30].

2.3 Results and discussion

Catalyst Characterization

2.3.1 X-Ray Diffraction

The XRD spectra of TiO_2 are shown in **Fig. 2.1(a)**. Diffractograms of TiO_2 derived from Titanium-butoxide show anatase crystalline phase (seen 2θ at 25.3° (101), 37.9° (004), 48.3° (200), 54.1° (105), 55.1° (211), 62.8° (204), 69.2° (116), 70.3° (220) and 75.4° (215). A reference to JCPDS Card no. 21-1272, confirms that anatase TiO_2 peaks are found in the spectrum [31]. The X-ray diffractogram of fly ash shows that the phase composition of fly ash has four essential crystalline components: quartz (SiO_2), mullite ($Al_6Si_2O_{13}$), magnetite (Fe_3O_4), and hematite (Fe_2O_3). The typical peaks in the XRD diffractogram at 16.45°, 25.98°, and 26.30° and 20.86°, 26.58°, and 36.55° show the mullite and quartz phases, respectively. There was a good match between the presence of these phases and their respective JCPDS cards: mullite (JCPDS card no.89-2644), quartz (JCPDS card no.89-1962), and hematite (JCPDS card no.33-664). The diffractogram shows a distinctive rise in intensity at angles ranging from 21 to 28° 2θ, as well as the comparatively low intensity of the quartz and mullite phase peaks showing microscopic particle size and a high activity index of FA [32]

The XRD spectra of TiO_2, FA and different (1wt%,3wt% and 5wt% TiO_2) FA- TiO_2 composites were investigated are shown in **Fig. 2.1(b)** Peaks observed at 2θ values of 16.45°, 25.98°, and 26.30° and at 20.86°, 26.58°, and 36.55° in the FA sample correspond to the presence of mullite and quartz phases, respectively. The characteristic peak at 2θ = 25.3° is attributed to pure TiO_2. All the FA diffraction peaks were retained in the FA–TiO_2 composites containing 0.5 wt%, 1 wt%, 3 wt%, and 5 wt% TiO_2. Additionally, a TiO_2-specific peak at 2θ = 25.3° becomes increasingly prominent with higher TiO_2 loadings, confirming the successful incorporation of TiO_2 onto the FA surface and the effective formation of the composite structure.

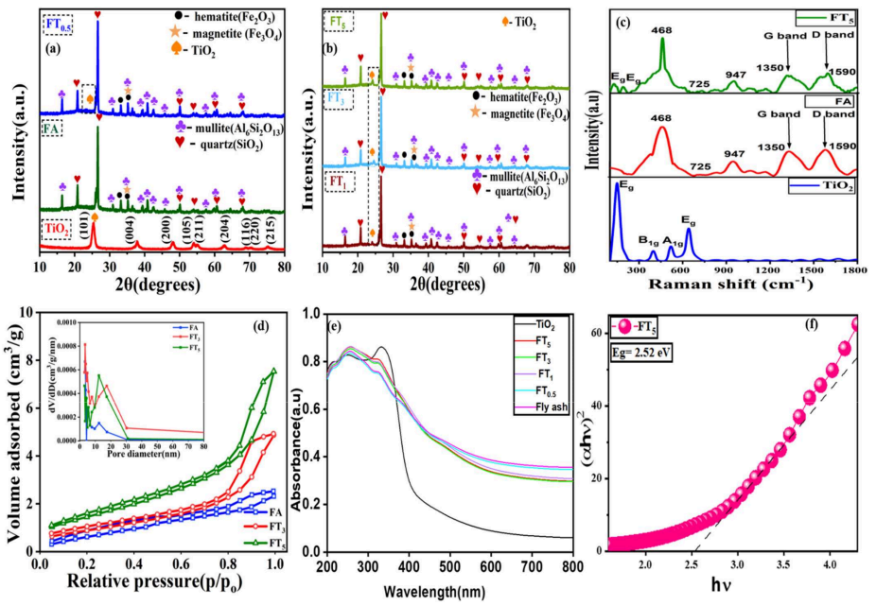

Fig. 2.1 XRD patterns of (a) TiO_2, fly ash (FA), and 0.5wt% TiO_2 loaded FA composites ($FT_{0.5}$), (b) FT_1, FT_3, FT_5 , (c) Raman spectra of TiO_2, fly ash (FA) and FT_5 composite, (d) N_2 adsorption-desorption isotherms, (inset) BJH plot distribution curves of FA, FT_3, and FT_5 nanocomposites,(e) Diffuse Reflectance Spectra of several composites and (f) Tauc Plot of FT_5 composite

2.3.2 Raman analysis

Fig. 2.1(c). shows the Raman spectra of FA, TiO_2 and FT_5 nanocomposite in the range of 200–1800 cm^{-1}. Raman spectroscopy was used to analyze structural defects and show the uneven structure of products. Raman spectra of fly ash showed 2 sharp peaks. arises from disorder-induced vibrations and indicates defects or structural irregularities in the graphitic carbon present, and the G-band near 1590 cm^{-1}, which corresponds to the in-plane vibrational mode of sp^2-bonded carbon atoms and represents more ordered, graphite-like domains associated with symmetry and crystallinity. These peaks confirm the presence of carbonaceous species in fly ash and help assess the degree of structural order within the material. The prominent band of about 467 cm^{-1} indicated the presence of quartz that corresponded to the symmetric Si-O

stretching mode of quartz. The peak at 725 cm^{-1} displayed intra and inter-tetrahedral deformation modes involving tetrahedral cation mobility in fly ash due to silica content. The presence of the mullite phase in fly ash has been shown by a conspicuous band around 960 cm^{-1} [33]Four distinct Raman active modes of anatase TiO_2 with symmetries E_g, B_{1g}, A_{1g}, and E_g were detected at 144, 396, 519, and 638 cm^{-1}, respectively. Raman spectra demonstrated the development of the anatase phase of TiO_2 [34]. Raman spectra of FT_5 nanocomposite showed both TiO_2 and fly ash peaks; however, Raman modes of TiO_2 in FT_5 composite become reduced due to the low concentration of TiO_2 on the surface due to more fly ash coverage.

2.3.3 BET analysis

The BET analysis in **Fig. 2.1 (d)** depicts the N_2 adsorption-desorption isotherms and the associated BJH pore-size distribution curves of fly ash, FT_3, and FT_5 nanocomposites. Following the IUPAC classification, nitrogen (N_2) adsorption-desorption isotherms of fly ash and composites showed type-IV isotherm with significant H3 hysteresis loops, indicating multilayer adsorption on mesoporous surface. The specific surface area, pore volume, and pore sizes of all the samples are reported in **Table 2.1**. The pore size of the samples is predominantly distributed within the 2–10 nm range, confirming their mesoporous characteristics. The analysis further reveals that the TiO_2–fly ash nanocomposites exhibit a substantially greater total pore volume and specific surface area in comparison to raw fly ash. The incorporation of TiO_2 introduces additional active energetic sites for pollutant adsorption and enhances pore accessibility, thereby facilitating faster diffusion of reactants and products. These features collectively contribute to improved photocatalytic performance of the composite material activity[35].

Table 2.1. Pore volume, surface area and pore diameter of TiO_2, fly ash, FT_3 and FT_5 composites.

Photocatalyst	**BET surface area (m^2/g)**	**Pore volume (cm^3/g)**	**Pore diameter (nm)**
TiO_2	99.70	0.195	12.309
Fly ash	1.347	0.003	3.054
FT_3	3.268	0.007	3.411
FT_5	5.434	0.010	7.814

2.3.4 UV-vis diffuse reflectance spectroscopy

UV-vis diffuse reflectance spectra of TiO_2, fly ash, and FT composites (0.5wt%,1wt%,3wt%, and 5wt% TiO_2) are shown in **Fig. 2.1 (e).** The DRS spectra depict peaks with wavelength below 400 nm in the UV region exhibiting transition of electrons from the valance band of (2p) O^{2-} orbital to (3d) Ti^{3+} orbital to the conduction band. The fly ash-TiO_2 composite shows enhanced ultraviolet (UV) light absorption, resulting in a redshift to a longer wavelength. This shift may be attributed to the formation of Si-O-Ti bonds between the TiO_2 and fly ash surfaces. The bandgap of as-prepared composites was estimated using Tauc's equation. Tauc's expression is written as:

$$\alpha h\nu = A(h\nu - E_g)^n \quad (4)$$

Where α denotes the adsorption coefficient, hν indicates the photon's energy, A is a constant, and E_g signifies the bandgap transition that occurs directly or indirectly (n=0.5 for a direct transition and 2 for an indirect transition). The bandgap values were estimated by projecting a straight line to the x-axis in the $(\alpha h\nu)^2$ graph vs. hν. The E_g value formulated to be 2.52 eV for FT_5 composite is depicted in **Fig. 2.1(f),** whereas Eg value of 3.12 eV for TiO_2, 2.84 eV for fly ash, 2.83 eV, 2.79 eV, 2.55eV for $FT_{0.5}$, FT_1, FT_3, composites are shown in **Fig. 2.2 (a-e)**.

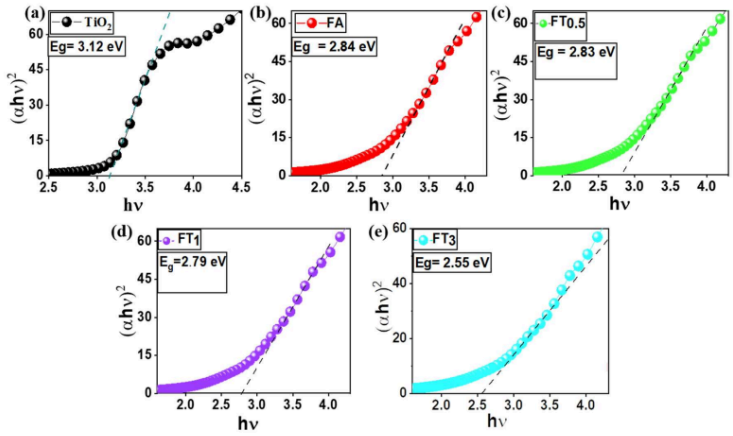

Fig. 2.2 (a-e) Tauc Plot of various photocatalysts.

2.3.5 Scanning Electron Microscopy

SEM analysis was performed to examine the morphology of the materials and their interactions within the composite samples. This provides insight into the structural characteristics of the FA-TiO_2 composites, particularly how varying TiO_2 loading influences the extent of TiO_2 coverage on the FA surface. The SEM images of TiO_2 shown in **Fig. 2.3(a)** reveal that the TiO_2 nanoparticles possess a predominantly spherical morphology. A noticeable degree of particle agglomeration is observed, indicating the tendency of TiO_2 nanoparticles to cluster together due to their high surface energy and nanoscale size. **Fig. 2.3 (b)** showed spherical-shaped FA particles with a smooth surface. SEM micrographs in **Fig. 2.3 (c-f)** show different FT composites with varying TiO_2 concentrations. In **Fig. 2.3 (c)** FT_1 nanocomposite shows FA particles covered partially by TiO_2 particles. **Fig. 2.3 (d)** presents a FT_3 nanocomposite in which TiO_2 concentration is higher, resulting in more TiO_2 coverage on the FA particles. **Fig. 2.3 (e, f)** presents the images of FT_5 nanocomposite, which reveal that the FA particles are even more extensively covered by TiO_2. [13].

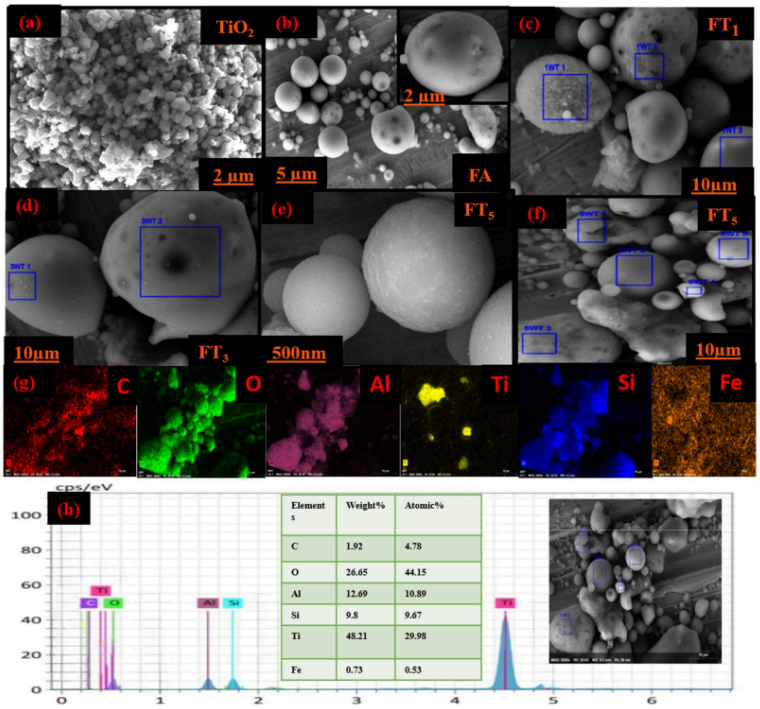

Elements	Weight%	Atomic%
C	1.92	4.78
O	26.65	44.15
Al	12.69	10.89
Si	9.8	9.67
Ti	48.21	29.98
Fe	0.73	0.53

Fig. 2.3 FE-SEM images of (a) TiO_2 (b) FA, (c) FT_1, (d) FT_3, (e,f) FT_5 (g) Elemental mapping, (h) EDS spectra of FT_5.

2.3.6 EDS spectra

Fig. 2.3 (g, h) displays the elemental mapping and EDS spectra of the (5wt% TiO_2 in FA - TiO_2) FT_5 composite, which reflects the atomic and weight proportions of the elements. The elemental mapping verifies the existence of elements such as C, O, Al, Ti, Fe, and Si, shown in red, green, purple, yellow, orange, and blue, respectively. Similarly, their elemental composition is confirmed by EDS spectra. The weight distribution of elements is 4.78, 44.15, 10.89, 9.67, 29.98, and 0.53% for C, O, Al, Si, Ti, and Fe, respectively.

2.4 Adsorption studies

2.4.1 The effect of adsorbent dosage on the removal of FB dye

Fig. 2.4(a) demonstrates a notable improvement in FB dye removal efficiency with increasing catalyst (adsorbent) dosage from 2 mg to 5 mg. Specifically, the removal efficiency increased from 39% to 57% for TiO_2, and from 49% to 59% for FA. For the composites $FT_{0.5}$, FT_1, FT_3, and FT_5, the removal efficiency enhanced from 52% to 65%, 60% to 66%, 63% to 70%, and 69% to 76%, respectively. This trend clearly indicates that higher catalyst loading provides more active surface sites for adsorption and photocatalytic interaction, resulting in greater dye removal performance**.** The removal effectiveness remained unchanged after increasing the dose from 5 mg to 7 mg. This observation suggests that the available active adsorption sites on the adsorbent surface become saturated beyond a dosage of 5 mg. Accordingly, 5 mg was identified as the optimal adsorbent mass for this system. At this dosage, the maximum adsorption capacity of the materials is reached, and further increases in adsorbent quantity do not result in higher dye removal efficiency. Determining the optimum adsorbent dosage is crucial in practical adsorption processes, as it ensures effective pollutant removal while maintaining cost efficiency. In this study, 5 mg of adsorbent was found to be optimal for achieving efficient FB dye removal.

2.4.2 The effect of adsorbate initial concentration on the removal of FB dye

The adsorptive performance of TiO_2, FA, and various FT nanocomposites was tested by varying the concentration of FB dye in the range of 5-30 mg/L, as shown in **Fig. 2.4 (b)**. With the increase of the initial dye concentration of fuchsin blue, removal efficiency gradually increases up to the concentration of 10 ppm. This is because at low concentrations more adsorption sites are available for the dye molecules thereby increasing removal efficiency. The maximum removal efficiency (76%) was obtained at an initial concentration of 10 mg/L. As the concentration of adsorbate increases, the removal efficiency decreases. The reduction in adsorption can be attributed to the progressive saturation of active sites as initial concentration increases. As a result, the ideal concentration of FB adsorption was determined to be 10 ppm for further experiments.

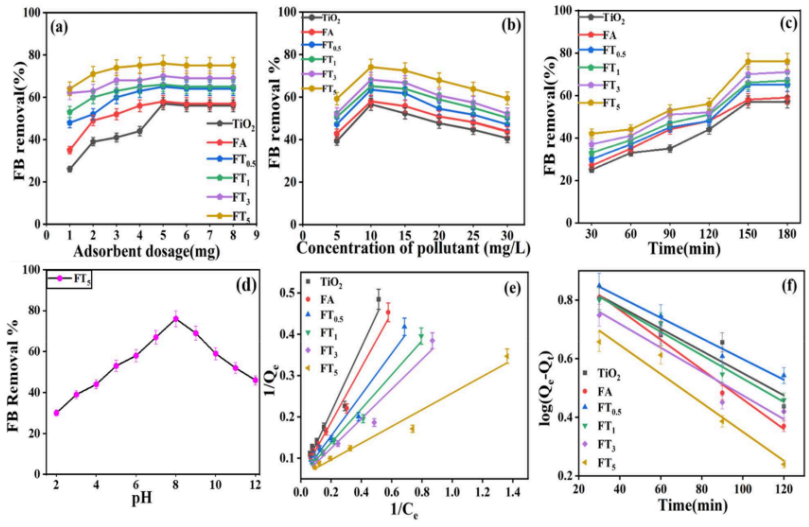

Fig. 2.4 (a) The effect of adsorbent dose on FB removal, (0.005/L) (b) the effect of adsorbate concentration, (10mg/L) (c) the effect of contact time, and (150min) (d) the effect of pH, (e) Langmuir isotherm (f) Pseudo-first-order kinetic model

2.4.3 The effect of contact time on the removal of FB dye

The duration of contact time between the adsorbate (fuchsin blue) and the adsorbents (FT_5) is a critical factor in the process of adsorption. Adsorption initially rises with increase in contact time until equilibrium is reached. The initial concentration of the FB dye in the solution is 10 mg/L. The percentage removal of the dye increased as the contact time between the dye and adsorbent increased. This means that longer contact times led to more efficient removal of the dye from the solution. The rate of adsorption slowed down as the contact time increased. This suggests that adsorption was more rapid in the early stages but gradually approached equilibrium. Equilibrium was reached after 150 minutes of contact. Between 150 min to 180 minutes, removal efficiency of the dye by the various adsorbents (TiO_2, FA, and FT) remained constant due to the saturation of active sites with dye. Compared to FA, TiO_2, and other composites, the FT_5 was the best adsorbent showing 76% fuchsin dye removal. However, all the adsorbents after 150 minutes shown in **Fig. 2.4 (c)** and further increase in contact time did

not improve adsorption behaviour.

2.4.4 The effect of pH on the removal of FB dye

Solution pH is one of the most essential parameters that influence the whole adsorption process. pH refers to the concentration of the hydrogen ion in a solution. Additionally, it may increase surface charges, which may enhance the electrostatic contact between the surface of the adsorbent and the adsorbate. The adsorption of FB over FT_5 composite was investigated in the range of pH 2-pH 10 for 150 min. **Fig. 2.4 (d)** illustrates that the removal efficiency of FB increases progressively as the value ranges from 2 to 10. The maximum removal percentage (76%) of FB by FT_5 was seen at pH 8. The results concluded that the remaining oxygen functional groups distributed on the surface of the composite transmit the negative charge, causing FB adsorption to be greatly reduced under alkaline circumstances. The adsorption happened because of electrostatic forces among the negatively-charged adsorbent and the positive-charged dye molecule because of the protonation of functional groups. At acidic conditions, the surface of the FT_5 composite, gains a positive charge, resulting in significant repellent force between the catalyst and dye molecules leading to a significant reduction in the percentage eradication. Adsorption sites are deprotonated because of static attraction and H bonding., leading to a significant loss of FB at alkaline pH. The point zero charge (pH_{ZPC}) of the FT_5 composite was determined to be 7.4 indicating that the adsorbent surface was negatively charged at $pH > pH_{ZPC}$ and became positively charged at $pH < pH_{ZPC}$ which will assist in improved adsorptive removal. Considering the pH at which maximal dye removal efficiency was attained was larger than pH_{ZPC}, a significant electrostatic interaction between dye molecules and FT_5 Composite has occurred. Therefore, an alkaline environment with a pH of 8 is optimal for the adsorption of FB onto FT_5 [36].

2.4.5 Adsorption equilibrium studies

Adsorption isotherms investigate how pollutant molecules interact with the adsorbent surface at equilibrium. The isotherms of adsorption were studied by altering the initial concentration of FB (5-30 mg/L) at a fixed amount of adsorbent (5 mg). As described by the Langmuir isotherm model, adsorption occurs on surface with uniformly energetic sites, resulting in monolayer adsorption of the adsorbate molecules onto the adsorbent. It is also acknowledged that adjacent molecules that are adsorbed do not interact with one another. The Langmuir adsorption isotherm is written as:

$$\frac{1}{Q_e}=\left(\frac{1}{K_L Q_{max}}\right)\times\frac{1}{C_e}+\frac{1}{Q_{max}} \quad (5)$$

where C_e (mg/L) is the equilibrium adsorbate concentration, Q_e (mg/g) is the equilibrium adsorption capacity of the adsorbent, Langmuir constant, K_L (L/mg), represents the affinity of the adsorbate for the adsorbent, and (mg/g) Q_{max} is the maximum adsorption capacity of the adsorbent before full monolayer formation [37]. The graph was drawn between $1/Q_e$ versus 1/Ce in **Fig. 2.4 (e),** and the intercept and slope were utilized to derive K_L and Q_{max} values. Using dimensionless constant R_L, it is possible to determine the type of adsorption and whether the process is favourable or unfavourable.

$$R_L=\frac{1}{1+K_L C_o} \quad (6)$$

where K_L signifies the Langmuir constant and C_o is the highest concentration of a contaminant initially. The adsorption type is represented by the value of R_L. If $R_L = 1$ (linear), $R_L = 0$ (irreversible), or $R_L > 1$ (unfavourable), $0 < R_L < 1$ (favourable). The Freundlich isotherm assumes the surface of the adsorbent to be heterogeneous and that there are substantial interactions between adsorbate molecules. The adsorption takes place on the surface of the adsorbent by the development of multilayers of adsorbate molecules. The Freundlich isotherm's equation is shown as follows:

$$\log Q_e=\log K_F+\left(\frac{1}{n}\right)\log C_e \quad (7)$$

Adsorption favorability is described by the Freundlich constant, K_F, and the heterogeneity factor, 1/n, where Q_e (mg/g) is the amount of contaminant adsorbed at equilibrium and Ce (mg/L) is the concentration of contaminant in solution at equilibrium. The graph was plotted between log Q_e versus log Ce. Values of n larger than unity suggest that the method is favourable [37]. The Freundlich and Langmuir models adequately predicted the experimental findings, as shown in **Table 2.2**. Compared to the Freundlich model, the Langmuir model appears to be a better fit for describing the adsorption behaviour of the pollutants on the mentioned adsorbents. The K_L values reflect the adsorption equilibrium constants for each adsorbent. The R_L values in the range of 0-1 indicate favourable adsorption, which supports the suitability of the Langmuir model for describing the adsorption process. Overall, for all the adsorbents, the correlation coefficient (R^2) values for the Langmuir model (0.9584–0.9830) were found to be closer to unity than those for the Freundlich model (0.9276–0.9562), indicating a better fit of the Langmuir isotherm. The Freundlich parameter "n >1" in **Table 2.2**. suggests that adsorption is non-linear and favours higher concentrations of the solute.

Table 2.2. Adsorption isotherm parameters for removal of FB dye over TiO_2, FA, and FT composites.

	Langmuir model				Freundlich model		
Adsorbent	**Q_{max} (mg/g)**	**K_L (L/mg)**	**R_L**	**R^2**	**K_F [mg/g.(L/mg)]$^{1/n}$**	**n**	**R^2**
TiO_2	18.182	0.070	0.3221	0.9584	1.6368	1.590	0.9339
FA	18.382	0.081	0.2890	0.9811	1.8125	1.576	0.9562
$FT_{0.5}$	18.552	0.107	0.2360	0.9628	2.3480	1.717	0.9276
FT_1	18.382	0.132	0.2016	0.9830	2.6187	1.716	0.9473
FT_3	19.230	0.144	0.1871	0.9649	2.9573	1.778	0.9285
FT_5	20.325	0.235	0.1241	0.9713	4.1266	1.956	0.935

2.4.6 Adsorption kinetics

To investigate the mechanism of the adsorption process of FB dye onto FA-TiO_2 composites, the experimental kinetic data was tested using the pseudo-first-order, pseudo-second-order kinetic models. The linear form of Lagergren's pseudo-first-order rate equation can be expressed as follows. [38]

$$\log(Q_e - Q_t) = \log Q_e - \frac{k_1}{2.303} t \quad (8)$$

where Q_t and Q_e denote adsorption rates (mg/g) at time t (min) and equilibrium, correspondingly, and k_1 is the first-order rate constant (min). **Fig. 2.4 (f)** shows the log (Q_e-Q_t) vs t plot for the FB linear regression equation for the pseudo-second-order model as follows:

$$\frac{t}{Q_t} = \frac{1}{k_2 Q_e^2} + \frac{t}{Q_e} \quad (9)$$

where k_2 represents the rate constant for the 2nd order and Q_e and Q_t denote amounts of pollutant adsorbed per gram of adsorbent (mg/g) at equilibrium and time t (min), respectively[39]. The 2nd-order kinetic model posits that the rate-limiting phase is chemisorption, which entails the exchange or movement of electrons among adsorbent and adsorbate. The first- and second-order kinetics parameters were calculated using the slope and intercept shown in the graphs, as shown in **Table 2.3**. Compared to the second-order model, the first-order model was shown to have a rate constant which is simultaneously bigger and nearer to unity. It demonstrates that the adsorption of FB dye onto TiO_2, FA, and FA-TiO_2 composites is governed by first-order kinetics.

Table 2.3. Kinetic model parameters for removal of FB dye over various photocatalysts

Adsorbent	Pseudo-first-order Model			Pseudo-second-order Model		
	Q_e (mg/g)	k_1 (min^{-1})	R^2	Q_e (mg/g)	k_2 (g/mg. min)	R^2
TiO_2	8.499	0.0087	0.9091	8.453	0.00128	0.8599
FA	11.402	0.0117	0.9841	16.638	0.00081	0.9621
$FT_{0.5}$	15.100	0.0080	0.9839	18.416	0.00066	0.8964
FT_1	18.407	0.0092	0.9774	18.348	0.00076	0.9126
FT_3	18.967	0.0094	0.9094	18.975	0.00077	0.8928
FT_5	22.698	0.0113	0.9482	20.040	0.0077	0.8836

2.5 Photocatalytic degradation of FB dye

Variations in the UV–visible absorption spectra of the FB dye solution treated with the FT_5 composite at different irradiation times are shown in **Fig. 2.5 (a, b).** The characteristic maximum absorption peak of FB occurs at 546 nm, and its intensity gradually decreases with increasing illumination, indicating progressive adsorption and photocatalytic degradation. Photocatalytic degradation using the FT_5 composite achieved an 88% reduction in dye concentration, whereas adsorption alone resulted in only 76% removal. This indicates that degradation is more effective than adsorption for complete elimination of fuchsin dye. Additionally, experiments performed without a catalyst showed that only 14% of FB underwent photolysis after 180 minutes of UV irradiation, demonstrating the high stability of the dye in the absence of a photocatalyst.

Table 2.4 Kinetic parameters of pseudo first order model over various photocatalysts

Photocatalyst	Pseudo-first-order Model	
	k_1	R^2
TiO_2	0.001	0.9907
FA	0.0005	0.9912
$FT_{0.5}$	0.0007	0.9948
FT_1	0.0007	0.9895
FT_3	0.0013	0.9833
FT_5	0.0016	0.9956

UV–visible absorption spectra of FB dye after photodegradation using bare and TiO_2-loaded

FA nanocomposites under 180 minutes of UV irradiation are shown in **Fig. 2.5 (c).** The absorption intensity depends on the TiO_2 concentration in the composite. TiO_2 loading significantly enhanced the photoactivity of fly ash, with 5wt% TiO_2 showing the highest catalytic efficiency, beyond which additional loading did not yield further improvement. To determine the optimal TiO_2 loading on fly ash for effective FB degradation, the time-dependent photodegradation profiles **(Fig. 2.5(d))** and the corresponding kinetic plots **(Fig. 2.5(e))** were analyzed. The results demonstrate that the degradation kinetics conform to a pseudo-first-order model, in accordance with the given equation (10).

$$\ln (C_o / C_t) = kt \qquad (10)$$

Where C_0 is the initial concentration of the FB dye in the solution at time 0, C_t refers to the FB dye concentration at time t. k represents the rate constant (min^{-1}), and t indicates the reaction time [30]. In this highly dilute system, the absorbance intensity ratio A_t at irradiation time t is proportional to the initial absorbance A_0 at $t = 0$, which can be ensured by adjusting the FB concentration ratio C_0/C_t. The pseudo-first-order rate constants and the corresponding squared linear correlation coefficients (R^2) for TiO_2, FA, $FT_{0.5}$, FT_1, FT_3, and FT_5 are summarized in **Table 2.4.** The histogram in **Fig. 2.5 (f)** compares the percentage removal of fuchsin blue dye by TiO_2, fly ash, and various FT composites during the dark adsorption and degradation process under UV light.

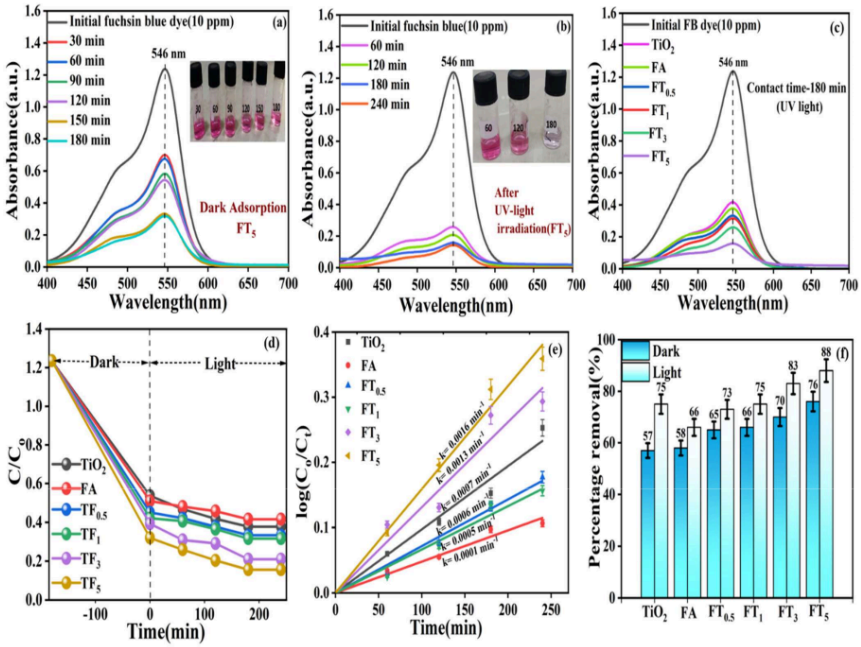

Fig. 2.5 Changes in UV absorption spectra of fuchsin blue dye (a) dark adsorption (b) after photocatalytic degradation by 5wt% TiO_2-loaded FA nanocomposite under UV irradiation, and (c) after 180 minutes by different wt% TiO_2-loaded FA composites, (d) time course kinetic plots of fuchsin dye in dark and light, (e) Pseudo first-order model, (f) histogram representing comparison of percentage removal of fuchsin blue dye under dark and light irradiation

2.6 Degradation pathway analysis

HRMS analysis was done to analyze the mass(m) /charge(z) ratio and identify the molecular formula. The precise m/z measurement for the fuchsin ion 330 was 330.0928. The degradation pathways of basic fuchsin (also known as fuchsin) are described as shown in **Fig. 2.6 (a, b)** determined by mass spectrometry analysis, two potential degradation pathways for this dye. These pathways represent how basic fuchsin molecules can degrade into various intermediates

and eventually into simpler, inorganic compounds like water (H_2O) and carbon dioxide (CO_2) under the influence of different reactions involving demethylation, hydroxylation, ring-opening reactions, and oxidation. Through pathway 1 Fuchsin (m/z = 365.91) undergoes demethylation to form Product B (m/z = 316.18). Product B undergoes another demethylation step to yield Product C (m/z = 302.17). Product C undergoes a ring-opening reaction with reactive oxygen species ($\bullet O_2^-$ and •OH) to generate Product D (m/z = 205.11). Product D is subsequently oxidized to form Product E i.e., 3-Heptynoic acid (m/z = 126.07). Product E 3-Heptynoic acid m/z = 126.07) is finally mineralized to H_2O, CO_2, and some inorganic ions. In pathway 1, the other side of product C (m/z = 302.17) undergoes the ring-opening reaction, transforms into product H (m/z = 282.16), and finally transforms into CO_2 and H_2O.

Through pathway 2, Product A (m/z = 330.09), which is produced by the ionization of fuchsin, goes through hydroxylation, i.e., the addition of a hydroxyl group, to form Product F i.e., carbinol of Pararosaniline (m/z = 347.21). Product F is oxidized to give Product G (m/z = 223.14). Product G is eventually mineralized to H_2O, CO_2, and certain inorganic ions [40].

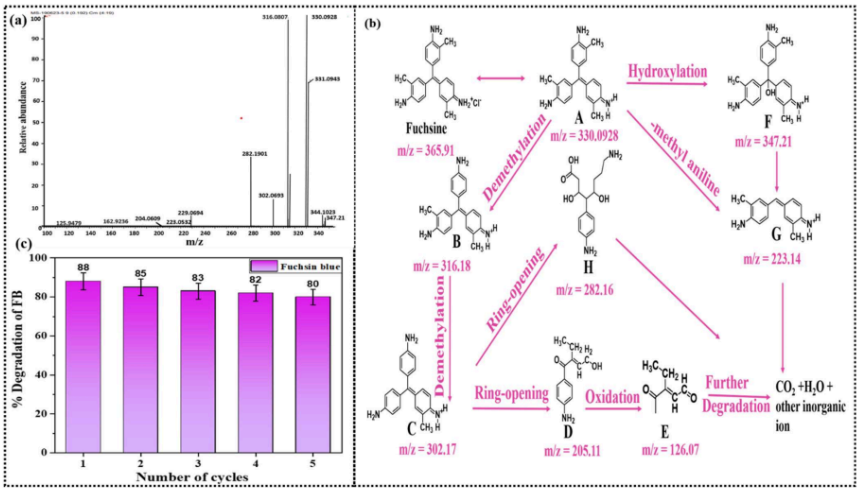

Fig. 2.6 (a) High-Resolution Mass Spectroscopy, (b) degradation pathway of fuchsin blue dye after degradation by FT_5 nanocomposite, (c) Reusability studies of FT_5 nanocomposite.

2.7 Reusability studies

In the first UV irradiation cycle, the FT_5 composite (5 wt% FA–TiO_2) achieved an 88% reduction in FB dye concentration over 180 minutes. This result highlights the excellent photocatalytic performance of the material and its suitability for dye removal applications. Interestingly, the degradation efficiency remains close even after five successive cycles of UV irradiation displayed in **Fig. 2.6 (c).** This suggests that the photo-catalytic activity of the composites remains almost stable and does not significantly degrade over multiple uses. The stable degradation efficiency observed over multiple cycles indicates that the FT_5 composite has a high re-usability performance. It can be used repeatedly without a substantial drop in its catalytic activity. Furthermore, an ICP-OES analysis was done to estimate the amount of metal ions (Al and Fe) leached from the composite. After 5 cycles of photocatalytic degradation, the concentration of Fe was 1.40 ppm, instead of 1.69 ppm before degradation. Aluminium metal concentrations were 2.53ppm before the procedure and 2.08ppm after five degradation cycles. This minimal leaching is further confirmed by a lower drop in removal efficiency in the re-usability test. This shows that the composites are stable and reusable. The high re-usability of the composite is attributed to the formation of Si-O-Ti linkages between FA (presumably a silica-based material) and TiO_2. These linkages immobilize the TiO_2 component, preventing its loss during the photocatalytic reactions. This immobilization of TiO_2 helps maintain the composite's catalytic activity over successive cycles. The FT_5 composite appears to be an efficient and repeatedly reusable photocatalyst for the degradation of FB dye.

2.8 Plausible Mechanism

The photocatalytic degradation of FB dye (shown in **Scheme 2.2)** involves a complex series of reactions where TiO_2 plays a critical role in generating reactive species that break down the dye molecules. At the same time, FA assists in adsorbing and retaining these pollutants on its surface, leading to enhanced degradation efficiency. Initially, FA binds to pollutant molecules (FB dye) in the solution and adsorbs them onto its surface. This adsorption is the first step in concentrating the pollutant molecules for subsequent degradation. Simultaneously, the TiO_2 loaded onto the surface of FA is exposed to UV light enhancing the movement of electrons from the valence band to the conduction band of TiO_2 [14]. This electron excitation is a crucial step in initiating the photocatalytic process. Positive holes form as electrons move from the VB to the CB. These positive holes are highly reactive species that can participate in oxidative reactions. The excited electrons in the CB of TiO_2 are trapped on the TiO_2 surface by oxygen molecules, leading to the formation of peroxide radicals ($O_2^{\cdot-}$). Simultaneously, the positive

holes can oxidize water molecules adsorbed on the TiO_2 surface, generating hydroxyl radicals (OH^-). These peroxide radicals and hydroxyl radicals are potent oxidative species. The peroxide radicals ($O_2^{\cdot-}$) and hydroxyl radicals ($OH^{\cdot}$) oxidize FB dye molecules in the solution. This oxidation process facilitates the breakdown of FB into simpler, less harmful organic molecules. FA is crucial in retaining free radicals (such as $O_2^{\cdot-}$ and $OH^{\cdot}$) on its surface. This retention enhances the rate of FB breakdown on the TiO_2 surface because the free radicals continue to react with FB in proximity. Over time, peroxide and hydroxyl radicals' oxidative reactions may eventually oxidize Fuchsin dye into harmless inorganic molecules like CO_2 and H_2O. The improved photocatalytic degradation efficiency observed with FT nanocomposites is attributed to the synergistic impact of FA's adsorption efficiency and TiO_2's photocatalytic activity. FA concentrates the pollutant molecules on its surface, making them more accessible to the TiO_2 photocatalyst, initiating the degradation process.

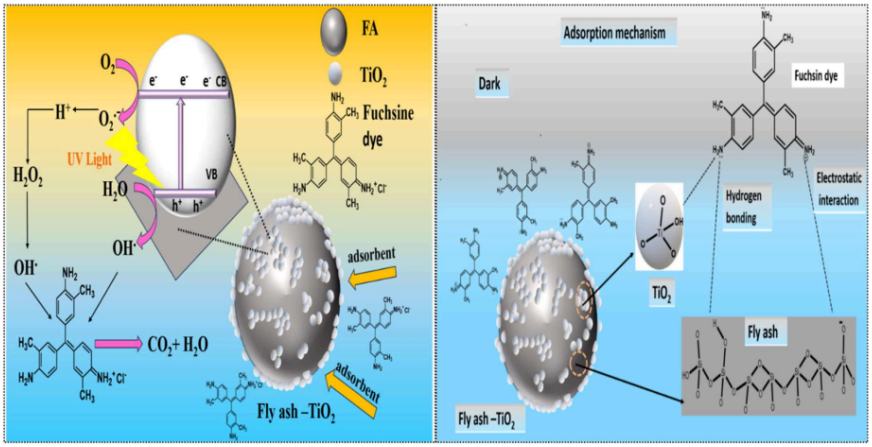

Scheme 2.2. The proposed adsorption and photocatalytic mechanisms of a FT nanocomposite under UV light irradiation.

2.9 Conclusion

Fly ash and TiO_2 (FT) composites were synthesized using a sol–gel method combined with wet impregnation. The maximum adsorptive removal of FB dye (76%) was achieved over FT_5 composite at an initial dye concentration of 10 mg/L within 150 minutes as compared to TiO_2

which exhibited an adsorption efficiency of 57%. The adsorption data were found to fit the Langmuir isotherm more accurately than the Freundlich model, indicating that monolayer adsorption predominated and suggesting a specific and well-defined adsorption mechanism for FB removal. Furthermore, the FT_5 composite exhibited the highest photocatalytic activity, achieving an 88% degradation of FB dye within 180 minutes of UV irradiation in contrast to TiO_2, which showed 75% degradation. The photocatalytic degradation kinetics followed a pseudo-first-order model, which is typically employed to describe such processes and provides a quantitative measure of the degradation rate. The photocatalyst exhibited remarkable stability and maintained its performance across four consecutive cycles of degradation, which can be attributed to the formation of Si–O–Ti linkages between fly ash and TiO_2. These chemical bonds effectively immobilize TiO_2 on the fly ash surface, thereby minimizing catalyst leaching during operation.

Chapter-3

Influence of copper deposition on fly ash–TiO_2 composites for combined adsorption and visible-solar photocatalytic degradation of fuchsin blue

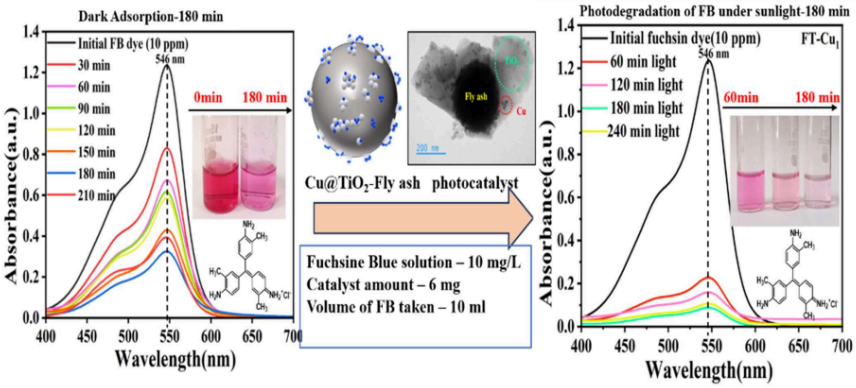

Schematic summary

3.1 Introduction

Environmental integrity and public health are significantly impacted by the harmful effects of

industrial dye pollution in wastewater. These dyes, widely used in many industries, including leather and textiles, showed significant resistance to deterioration, extending their longevity in the environment [1]. Unregulated dye pollution harms the ecosystem over time, affecting the aesthetics of water bodies and endangering aquatic life [2]. A decrease in biodiversity may result from the toxic, mutagenic, or even carcinogenic effects of certain dyes, which put marine life in danger [3]. Therefore, employing an environmentally and economically sustainable technique is essential to remove all colour molecules from wastewater before it is released into the environment[4,5]. Its high toxicity, carcinogenicity, and lack of biodegradability make it a hazardous contaminant [6]. Fuchsin blue dye contact may result in serious health complications such as headaches, skin and respiratory tract irritations, vertigo, and vomiting [7]. This dye has poor biodegradability and is toxic and carcinogenic; it must be eliminated from wastewater before discharge into the water effluents to reduce environmental contamination [8].

Several approaches have been developed for the extraction and elimination of contaminants from wastewater, including membrane separation, biological oxidation process, chemical precipitation, ion exchange, photocatalytic degradation, and adsorption[9,10]. Nevertheless, these techniques have drawbacks such as high operating costs, energy consumption, poor selectivity, regeneration, and reusability problems [11]The adsorption process is extensively employed in wastewater treatment because of its ease of operation, environmental friendliness, excellent efficacy, and minimal energy requirement [12,13]. Photocatalysis is a promising and eco-friendly advanced oxidation approach for treating wastewater. Photocatalysis can degrade many contaminants, comprising substances resistant to conventional treatment methods, and convert them into non-toxic substances like water and carbon dioxide. This method can drastically save operating expenses because it uses relatively little energy, especially when sunlight is employed as the light source. Photocatalysis reduces the possibility of secondary contamination because it does not involve chemical additives and yields nontoxic byproducts [14]. Adsorption combined with photocatalysis is a novel way to combine the benefits of both technologies while minimizing the limitations of each one alone[15]. There are disadvantages to using adsorption and photocatalysis independently, including expensive adsorbent renewal as well as the potential risk of secondary pollution due to insufficient degradation of contaminants or exhausted adsorbents [16]. The combination of adsorbent and photocatalyst cut the expense and frequency of adsorbent regeneration. Adsorbents can be regenerated in situ, increasing their lifespan, and decreasing waste through the photocatalytic destruction of contaminants directly on their surface. Adsorbents and photocatalysts can work together to enhance photocatalytic activity. TiO_2 has emerged among the most researched photocatalysts

due to its remarkable chemical stability, significant photosensitivity, and low toxicity[17]. TiO_2 is less efficient under normal sunlight because a limited part of the solar spectrum falls within the UV region. Wide band gap and exclusive sensitivity to UV light activation (e.g., TiO_2 anatase <390 nm with a band gap energy of 3.2 eV), make its practical implementation difficult, especially in solar-driven photocatalysis [18–20]. A bathochromic shift, which narrows the band gap, can be induced in the TiO_2 lattice by adding metal [21], (Fe, Cu, V, etc.) dopants. This modification causes TiO_2 to absorb visible light, enhancing its efficiency under solar radiation and boosting its photocatalytic activity beyond the UV spectrum. Among the various transition metal dopants, copper (Cu) has been extensively researched and is highly recommended for doping TiO_2 to achieve superior performance. Additionally, copper is relatively less toxic, an essential and abundant element [22], and is more cost-effective than other dopants such as silver [23]. Incorporating Cu into the TiO_2 lattice modifies the band gap and inhibits the recombination of photo-induced electron-hole pairs, increasing catalytic activity [24].

To address the challenge of difficult recovery, TiO_2 can be loaded onto various carriers, including activated carbon fibers [25], silica [26], and fly ash [27]. Fly ash exhibits several benefits compared to other carriers: inexpensive, readily available, non-toxic, and resistant to high temperatures, exhibiting a substantial surface area, small particle size, and excellent dispersibility in solution. These properties facilitate simple recycling and prevention of secondary pollution [28]. Additionally, fly ash embodies the principle of "using waste to treat waste," making it an ideal carrier for TiO_2 [29]. Fly ash-TiO_2 composites, due to the porous structure and high surface area of fly ash, exhibit excellent adsorption characteristics, which enhance their overall performance in pollutant removal. The ability to perform both adsorption and photocatalysis significantly broadens usefulness in environmental remediation processes. The photocatalytic activity of Fly ash-TiO_2 composites for FB dye removal was 88% compared to the removal of 75% over bare TiO_2 as determined in the previous work, which is currently under review.

Studies have reported that over the past few decades numerous studies utilising metal (Ag/Cu /Fe/Pt)-TiO_2, TiO_2 loaded fly ash and metal loaded TiO_2-fly ash composites for the photodegradation of organic pollutants in the presence of UV light and visible light have been conducted in the past. Li et al. [30] utilized the sol-gel method to produce Mo-doped TiO_2 coated on fly ash cenospheres (CTAB-Mo-TiO_2/FAC), which demonstrated 99.75% elimination of methylene blue under visible light. Wang et al. [31] synthesised Fe^{3+}-doped TiO_2 on fly ash cenospheres (Fe–TiO_2/FAC) using the sol-gel method, demonstrating enhanced

photocatalytic activity for methyl blue degradation under visible light, with optimal performance at 450°C and 0.01% Fe doping. Ag-doped TiO_2 supported on fly ash magnetic beads (Ag-TiO_2-FAMB) was synthesized by Li et al. [29] to enhance photocatalytic efficiency and recovery, achieving 98.5% xanthate degradation under visible light. Kanakaraju et al. [32] synthesized a Cu/TiO_2/FA composite using the wet impregnation method to achieve a 99% removal of methyl orange under visible light. However, report of studies utilising Cu-deposited fly ash-TiO_2 composites, for efficient removal of fuchsin blue under visible and solar light is less explored.

The aim of this study is to develop and evaluate the adsorptive and photocatalytic performance of Cu-loaded fly ash-TiO_2 (FT-Cu) composites for removal of FB dye from its aqueous solution under visible/solar light. The objectives of the present work are to determine the role of Cu nanoparticles in enhancing activity of adsorption and photocatalytic degradation of FB dye. Also to determine the photodecomposition pathway, and assess the photostability and recyclability of the composites.

The present investigation elucidates the synthesis of Cu-loaded Fly ash-TiO_2 (FT-Cu) composites with different percentages of copper (0.5,1, 2wt%) by sol-gel, wet impregnation method, and photo-deposition method. The comparative adsorption and photocatalytic degradation of FB dye were studied to evaluate the influence of Cu loading onto FT composite on its photocatalytic performance when exposed to visible light and sunlight. Moreover, the kinetic rate law and the photodegradation pathways of the fuchsin blue dye are also investigated by analysing various reactive oxygen species and identifying intermediate photoproducts using high-resolution mass spectral analysis. This research introduces a cost-effective, non-toxic, and solar light-driven highly efficient photocatalyst that can be recycled and reused, thereby addressing the complexities related to the wastewater treatment process and the recovery of photocatalysts, making it a more environmentally friendly approach.

3.2 Materials and methods

3.2.1 Materials and reagents

Titanium butoxide ($Ti(OC_4H_9)_4$, 97%) and Didecyl dimethyl ammonium chloride ($C_{22}H_{48}ClN$) were procured from Sigma-Aldrich, India. Acetic acid ($C_2H_4O_2$, 99.8%), Ethanol (C_2H_5OH, 99.9%), Cupric nitrate ($Cu(NO_3)_2 \cdot 3H_2O$, 99.5%), isopropyl alcohol (C_3H_8O, 99.5%) and FB dye ($C_{20}H_{19}N_3.HCl$) were sourced from Loba Chemie, India. Fly ash was sourced from the Rajpura Power Plant, India. These reagents were of analytical quality and thus used directly

without further purification. Deionized water (DI) was produced using an ultra-filtration system (Milli-Q, Millipore) with a conductivity of 35 mhos cm^{-1} at 25°C.

3.2.2 Characterization methods of prepared samples

The crystal structure diffraction data were recorded using a Smart Lab SE X-ray diffractometer equipped with Cu-Kα radiation (1.54 Å) and operated at an accelerating voltage of 45 kV. The measurements were conducted over a diffraction angle range of $5° \leq 2\theta \leq 80°$, with a slit width of 10 mm, a step scan size of 0.01, at a scanning speed of 5° per minute. FESEM (JEOL JSM-7600F, JAPAN working at 30kV) was utilized to characterize the morphology of the surface and microstructures of the catalyst. The composition and distribution of elements were identified via energy dispersive spectroscopy (Bruker EDS). High-resolution TEM images were taken by a High-Resolution Transmission Electron Microscope (HRTEM, JEOL JEM - 2100 model,JAPAN). The sample surface area and pore size profile were analyzed with the BET Autosorb iQ (Quantachrome Instruments, version 3.01, U.S.A.) The oxidation states of the elements in the composite were analyzed using X-ray Photoelectron Spectroscopy (XPS) with a Thermo Fisher Scientific NEXSA instrument, UK. Approximately 100–150 mg of the sample was degassed in the presence of helium gas at 200°C for 2 hours to remove moisture. Following degassing, liquid nitrogen was used for adsorption and desorption analysis. The optical properties were assessed using a Diffuse Reflectance Spectrophotometer (JASCO V-750, JAPAN) and $BaSO_4$ as a reference. High-resolution mass spectroscopy (Waters QTOF mass spectrometer equipped with XEVO G2 XS UPLC and coupled to APCI and ESI ionization sources,10 min retention time) was employed to detect degradation products which offered important insights regarding the photocatalytic degradation pathway.

Preparation of Cu deposited fly ash-TiO_2 particles

3.2.3 Cu photo deposited fly ash-TiO_2 (FT- Cu) composite

The synthesis procedures for TiO_2 and fly ash–TiO_2 (FT) composites have been described in detail in Chapter 2 (Sections 2.22 and 2.2.3). The deposition of Cu on the FT composite was carried out using the photo deposition method. A 100 mg sample of the prepared FT composite was dispersed in 10 mL of a 50% aqueous isopropyl alcohol solution in a test tube. Then, the required amount of 0.01 M copper nitrate solution (0.5–2 wt% Cu) was mixed to this FT dispersion and purged with Argon gas for 15 minutes to eliminate dissolved oxygen. The solution in the test tube was enclosed using rubber septa and exposed to a UV light source (125

W Hg arc, 10.4 mW/cm²) when subjected to constant magnetic agitation for 2 hours. After that, grey-coloured Cu-deposited FT composite (FT-Cu) was separated using centrifugation at 8000 rpm for 8 minutes, rinsed with distilled water and ethanol, and dried at room temperature. This approach was repeated to obtain an adequate quantity of FT-Cu composite for photocatalytic applications. The Cu-deposited FT composite catalyst containing 0.5wt%, 1wt% and 2wt% of Cu are named as FT-$Cu_{0.5}$, FT-Cu_1, and FT-Cu_2 respectively [32].

3.2.4 Measurement of point of zero charge (pzc) of composite:

The zero-point charge is an important physicochemical parameter that indicates the pH at which the adsorbent surface has no net charge. This parameter was evaluated using the solid addition method with 0.002 M cetrimide ($C_{19}H_{42}BrN$) and 0.1 M KCl solutions. In this procedure, 25 mL of each solution was placed in separate test tubes, and the initial pH of these solutions was adjusted to 2 to 10 using 0.1 M NaOH and 0.1 M HCl. Next 6 mg of FT-$Cu_{0.5\text{-}2}$ composite was introduced into each test tube that was kept for 3 hours with constant shaking to allow equilibration. The solution underwent filtration, and the final pH was recorded. The zero-point charge was ascertained by plotting the change in pH ($\Delta pH = pH_i - pH_f$) versus the initial pH and finding the intersection point on the graph.

3.2.5 Dark adsorption study of FB dye

The adsorption properties of FT and FT-$Cu_{0.5\text{-}2}$ composites were systematically evaluated using a 10 ml solution of the FB dye pollutant based on the influence of several critical parameters, e.g., the concentration (5 to 30 mg/L) of FB dye, the adsorbent dosage (1-10 mg) and the contact time (30 to 180 min). Under dark conditions, a magnetic stirrer was employed to uniformly mix and agitate multiple test tubes, each containing 10 mL of FB dye solution with varying concentrations and corresponding amounts of adsorbent. After the designated agitation period, the test tubes were withdrawn and subjected to centrifugation to ensure efficient separation of the FT/FT-Cu composite adsorbents from the liquid phase. The residual dye concentration in the supernatant was quantified using a UV–visible spectrophotometer at the characteristic maximum absorbance of FB dye (λ_max = 546 nm), based on previously established calibration curves in accordance with Lambert–Beer's law. The adsorption performance of the adsorbents, expressed as the pollutant mass adsorbed per unit adsorbent mass (mg/g), was calculated using the following formula:

$$\text{Adsorption capacity} = Q_e = (C_o - C_e) \times \frac{V}{W} \quad (1)$$

In this equation, C_o signifies the starting concentration of the FB dye (mg/L), whereas C_e denotes the dye's equilibrium concentration in the solution (mg/L). W indicates the adsorbent mass (g), V is the volume of the FB dye solution (L), and Q_e corresponds to the adsorption capacity of the adsorbent at equilibrium (mg/g)[33]. The percentage of dye absorbed by the adsorbents (R%) was evaluated using the subsequent equation.

$$\% \text{ removal of FB dye} = R\% = \left(\frac{C_o - C_e}{C_o}\right) \times 100 \quad (2)$$

C_0 and C_e represent the initial and equilibrium concentrations, while R% indicates the percentage of FB dye eliminated from the solution.

3.2.6 Photocatalytic degradation study

The photocatalytic degradation was conducted in a test tube containing 10 ml of FB dye (10 ppm) and different photocatalyst (6 mg) dispersion with continuous magnetic stirring and visible light (Wipro Garnet B22 50-Watt LED bulb (wavelength > 360 nm) irradiation for different time (60-240 min) periods. Before exposure to light radiations sample was magnetically agitated for 180 minutes in the dark to ensure that the catalyst and FB dye molecules were in a state of adsorption-desorption equilibrium. After photo-irradiation at various time intervals, the test tube was extracted, and the mixture was subjected to centrifugation for 8 minutes at 8000 rpm. The clear supernatant FB dye solution was analyzed and quantified using a UV-visible spectrophotometer at the FB dye's at λ_{max} = 546 nm using the standard calibration curves shown in **Fig. 3.1**. The absorbance spectra of the FB dye were monitored to assess the degree of degradation, yielding valuable information regarding the efficacy of the photocatalytic process [34]. The photodegradation efficiency was derived using the following formula:

$$\text{Rate of FB degradation } (\%) = \frac{A_o - A_t}{A_o} \times 100 = \frac{C_o - C_t}{C_o} \times 100 \quad (3)$$

In this context, A_0 and C_0 represent the initial absorbance and initial FB dye concentration at time zero while A_t and C_t pertain to the absorbance and the dye concentration at a specific time t, respectively [35,36]

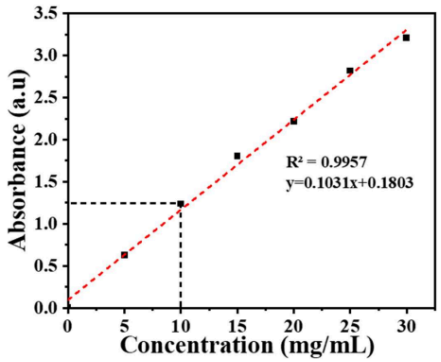

Fig. 3.1 Calibration curve of FB pollutant at different concentrations

3.3 Results and discussion

3.3.1 XRD analysis

The crystal planes and corresponding diffraction angles for the synthesized FT and FT-Cu_1 nanocomposites observed in the XRD spectra are presented in **Fig. 3.2.** The characteristic anatase crystalline phase of TiO_2 is evident from the diffraction peaks at 25.3° (101), 37.9° (004), 48.3° (200), 54.1° (105), 55.1° (211), 62.8° (204), 69.2° (116), 70.3° (220), and 75.4° (215), confirming the presence of anatase TiO_2 consistent with the JCPDS Card No. 21-1272 [37]. The X-ray diffractogram of fly ash reveals four primary crystalline phases: quartz (SiO_2), mullite ($Al_6Si_2O_{13}$), magnetite (Fe_3O_4), and hematite (Fe_2O_3). Characteristic peaks in the XRD profile at 16.45°, 25.98°, and 26.30° align with the mullite phase, while peaks at 20.86°, 26.58°, and 36.55° are attributed to the quartz phase. These phases effectively match with their respective JCPDS cards: mullite (JCPDS card no. 89-2644), quartz (JCPDS card no. 89-1962), and hematite (JCPDS card no. 33-664) [38]. Additionally, the diffractogram exhibits a notable increase in intensity within the 21 and 28° 2θ range, accompanied by relatively low-intensity peaks of quartz and mullite, suggesting a fine particle size and high activity index of the fly

ash. All the peaks identified in the fly ash were also found in the FT composite, with an additional peak at 2θ = 25.3° corresponding to TiO_2. This peak in the FT composite highlights the successful incorporation of TiO_2 onto the fly ash surface, demonstrating the effective formation of the composite. Conversely, in the FT-Cu_1 photocatalyst, no distinct peak for the Cu co-catalyst was detected following the deposition of Cu metal onto the FT composite. Previous research has established that metal nanoparticles with a low weight percentage (<5wt%) are usually not visible in XRD spectra.

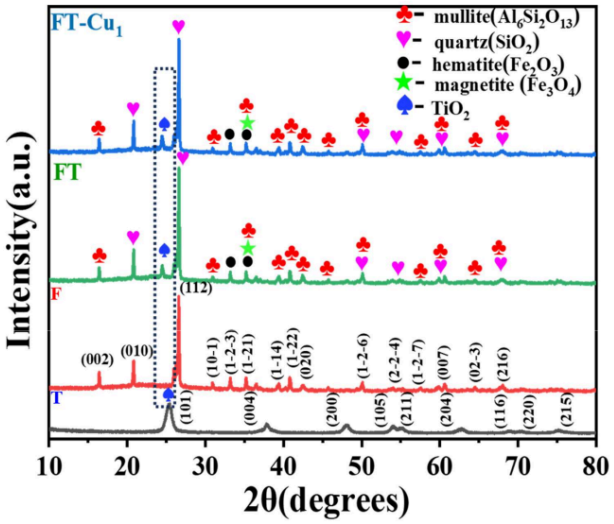

Fig. 3.2 XRD patterns of TiO_2(T), Fly ash (F), FT and FT-Cu_1).

3.3.2 FESEM. HRTEM and EDS analysis

The morphological and microstructural characteristics are illustrated in **Fig. 3.3(a)**; the SEM images of TiO_2 nanoparticles exhibit a spherical morphology. However, the TiO_2 particles tend to agglomerate and form clusters [39]. The Fly ash particles depicted in **Fig. 3.3(b)** demonstrated a spherical morphology and a uniformly smooth surface [40]. The FESEM

images of the FT and the FT-Cu_1 in composite **Fig. 3.3(c-f)** show that the spherical fly ash particles were more thoroughly coated with TiO_2. However, the Cu nanoparticles were not visible in the FESEM images due to their tiny size within the nm range. Nevertheless, the EDS spectra confirmed the presence of oxygen, aluminium, silicon, titanium, iron, and copper within the FT-Cu_1 composite.

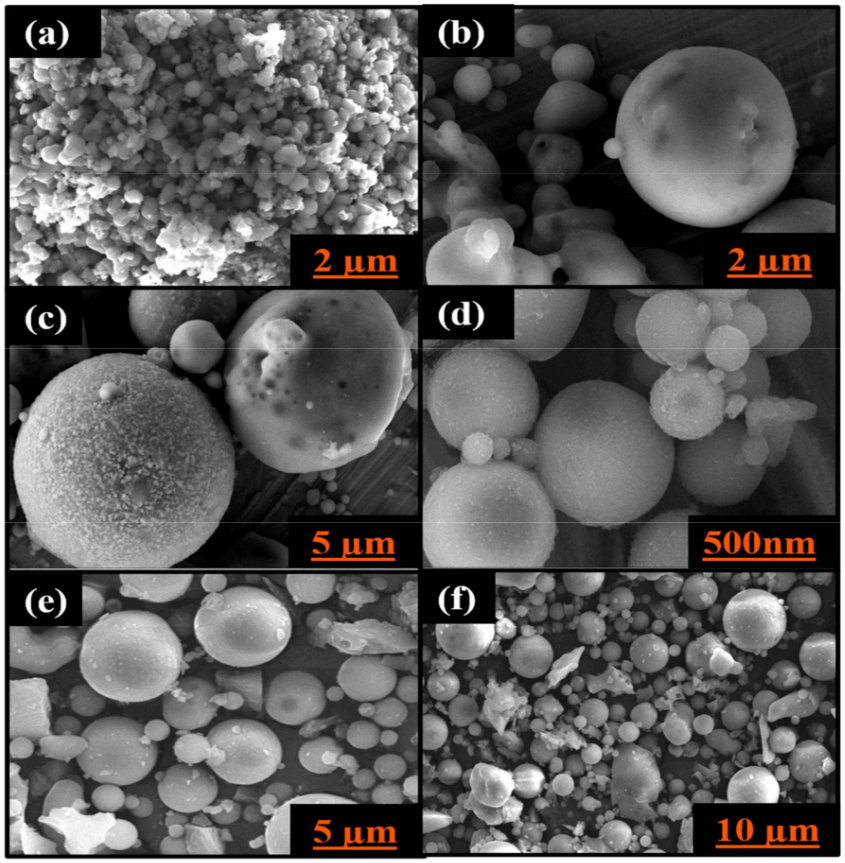

Fig. 3.3 FE-SEM images of (a) TiO_2(b) FA, (c & d) FT, and (e & f) FT-Cu_1 composite

In **Fig. 3.4 (a–c),** the TEM micrographs of the FT-Cu_1 composite at multiple resolutions demonstrate a homogeneous distribution of Cu nanoparticles over the FT surface. The nanoparticles, identifiable as dark spherical domains, exhibit a largely spherical morphology, confirming uniform deposition throughout the composite. The particle size of deposited Cu was observed in the 7 to 17 nm range. Their compact size potentially provides increased active sites, thereby enhancing photocatalytic activity. Moreover, the HRTEM micrographs in **Fig. 3.4(d)** distinctly reveal two distinct sets of lattice fringes of TiO_2 and Cu. One set is attributed to metallic Cu's (111) diffraction plane, characterized by an interplanar spacing of 0.21 nm. In contrast, the other set exhibits a lattice fringe spacing of 0.35 nm, corresponding to the (101) crystal plane of TiO_2. The image shows the lattice fringes for TiO_2 and Cu [41].

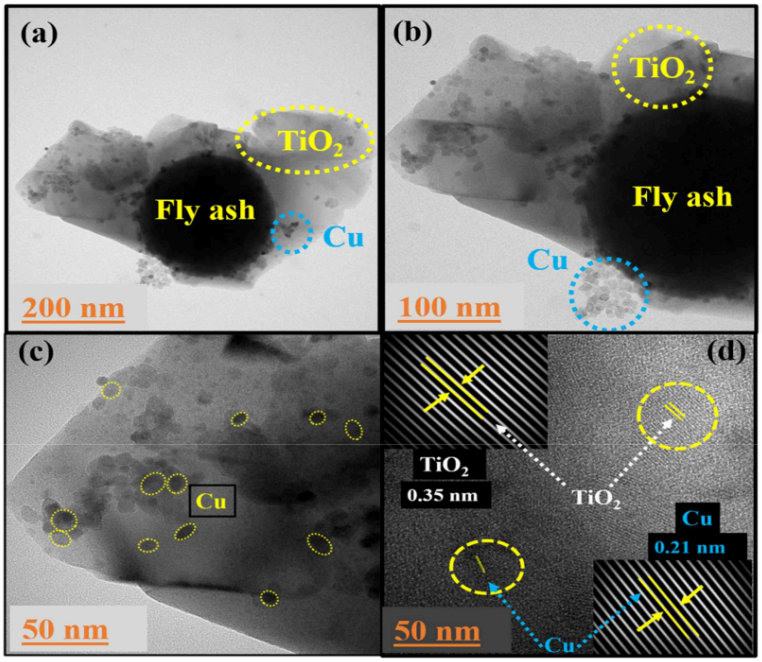

Fig. 3.4 HRTEM images of (a-c) FT-Cu_1 composite and (d) corresponding Lattice fringes

As shown in **Fig. 3.5**, the EDS results provide a quantitative assessment of the elemental composition of the FT-Cu_1 composite. The composite predominantly contains oxygen (55.19%) and silicon (41.65%), consistent with the underlying fly ash–TiO_2 matrix. Minor proportions of aluminum (1.48%), titanium (0.15%), iron (0.17%), copper (1.05%), and magnesium (0.04%) are also detected, validating the elemental distribution within the material.

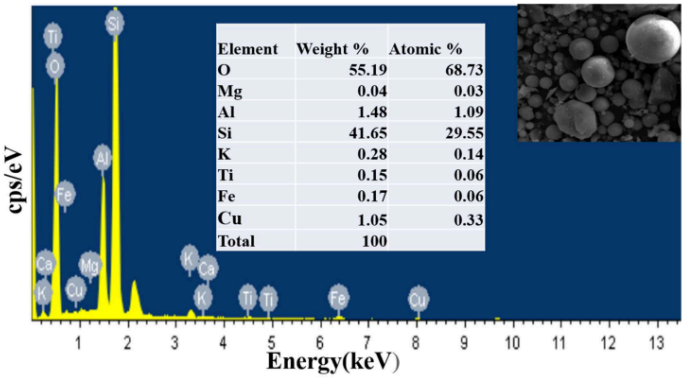

Fig. 3.5 Elemental analysis (EDS) of FT-Cu_1 composite

3.3 Surface area and pore size analysis

The surface characteristics and pore size distributions of the synthesized materials were assessed by analysis of N_2 adsorption-desorption isotherms and the associated BJH pore-size distribution graph of fly ash, FT and FT-Cu_1 composite are depicted in **Fig. 3.6 (a-b)**. The N_2 adsorption–desorption isotherms exhibit type-IV profiles with H3-type hysteresis loops confirming the presence of mesoporous structures characteristic of multilayer adsorption [42]. The pore size distribution further validates mesoporosity, with pore diameters predominantly in the range of 2–10 nm. Incorporation of TiO_2 and copper significantly enhances the surface textural properties of the FT-Cu_1 composite, which displays a higher specific surface area and pore volume compared to the other samples. These improvements promote more efficient adsorption of FB dye and simultaneously enhance photocatalytic activity in both FT and FT-Cu systems by enabling better diffusion and interaction of reactant and product molecules. The

observed enhancements can be attributed to the generation of additional active sites and synergistic structural–functional effects. Detailed values of specific surface area, pore size, and pore volume for all samples are provided in **Table 3.1.**

Table 3.1. Pore volume, surface area and pore diameter of TiO_2, fly ash, FT_3 and FT_5 composites.

Photocatalyst	**BET surface area (m^2/g)**	**Pore volume (cm^3/g)**	**Pore diameter (nm)**
TiO_2	99.703	0.195	12.309
Fly ash	1.347	0.003	3.054
FT	3.268	0.007	3.411
FT-Cu_1	6.725	0.010	8.712

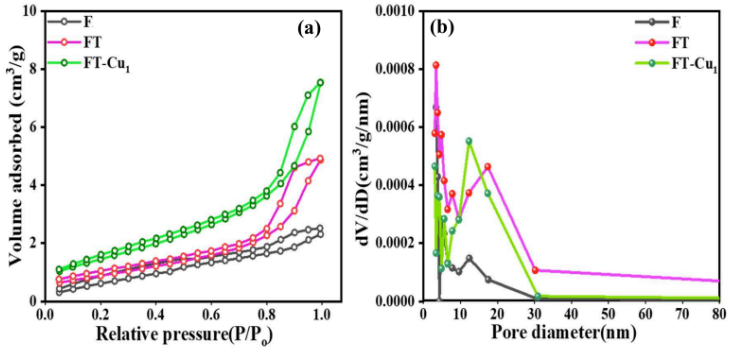

Fig. 3.6 (a) N_2 adsorption-desorption isotherms and (b) BJH plot distribution curves of various (FA, FT, and FT-Cu_1) composites

3.3.4 Optical absorption and band gap analysis

The UV-vis diffuse reflectance spectra for FT and FT-Cu_1 composites with copper concentrations ranging from (0.5- 2 wt%) are shown in **Fig. 3.7(a),** with the corresponding

Tauc plots in **Fig. 3.7(b-d)**. The DRS spectra illustrate peaks at wavelengths under 400 nm in the ultraviolet region, denoting the electron transitions from the valence band, particularly the (2p) orbitals of O^{2-} ions, to the conduction band, involving the (3d) orbitals of Ti^{3+} ions. The FT composite demonstrates enhanced ultraviolet (UV) light absorption, which results in a shift to longer wavelengths. This observed shift can be ascribed to the formation of Si-O-Ti bonds between TiO_2 and fly ash surfaces [43]. This absorption capability was further elevated with Cu loading on FT composites that reduces the bandgap, shifts the absorption edge to the visible light region by creating localized energy levels, forming strong heterojunctions, altering the electronic structure through doping, and synergistically interacting with the fly ash and enhances overall light absorption, thereby improving photocatalytic efficiency and resulting in a significant red shift in the absorption edge of the FT-Cu composite.

The bandgap of the as-prepared composites was determined using Tauc's equation, which is expressed as:

$$\alpha h\nu = A(h\nu - E_g)^n \quad (4)$$

α is defined as the absorption coefficient, $h\nu$ refers to the photon energy, A is a proportionality constant, and E_g signifies the bandgap, corresponding to either a direct or indirect transition (n=0.5 for a direct transition and n=2 for an indirect transition). The band gap values were determined by extrapolating a straight line to intersect the x-axis on the plot of $(\alpha h\nu)^2$ versus $h\nu$ [44]. Based on the analysis, the E_g values were found to be 2.27 eV for FT-Cu_1, followed by 3.12 eV for pure TiO_2, 2.84 eV for fly ash, 2.55 eV for the FT composite, and 2.35 eV for the FT-Cu_2 composite.

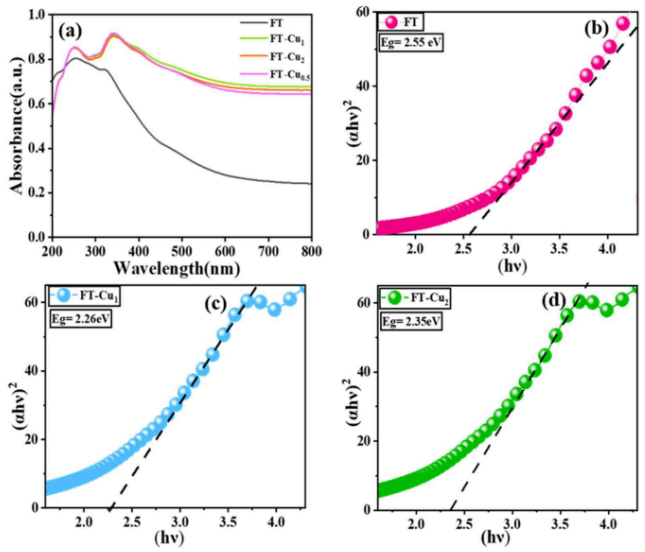

Fig. 3.7 (a) Diffuse reflectance spectra of (b-d) Tauc Plot of FT, FT-Cu_1 and FT-Cu_2 composites.

3.3.5 XPS analysis

X-ray photoelectron spectroscopy (XPS) was conducted to determine the elemental composition and chemical states of the FT-Cu composite as shown in **Fig. 3.8(a-f)**. The XPS analysis of TiO_2 revealed distinct peaks in the Ti 2p and O 1s regions, confirming the existence of titanium and oxygen species in the material. The Ti 2p spectra showed peaks at 458.6 eV ($2p_{3/2}$) and 464.3 eV ($2p_{1/2}$), indicating titanium in the +4 oxidation state, typical of TiO_2, with binding energies consistent with those found in pure TiO_2. The O 1s spectra revealed a dominant peak at 531.7 eV, which corresponds to surface hydroxyl groups or oxygen species associated with C–O bonds [45] . Peaks observed at 102.65 eV in the Si 2p spectra and 74.4 eV in the Al 2p spectra confirmed the presence of silicate species and Al^{3+}, respectively, derived from the fly ash [46,47] Furthermore, the Fe 2p spectra revealed peaks at 710.9 eV ($2p_{3/2}$) and 724.7 eV ($2p_{1/2}$), characteristic of Fe^{3+} in iron oxides [48]. The Cu 2p spectra, as illustrated in **Fig. 3.8(e),** displayed binding energy peaks at 932.9 eV ($2p_{3/2}$) and 952.7 eV ($2p_{1/2}$), with a 6-eV energy separation, indicative of copper in the Cu (0) oxidation state. Moreover, the presence

of a satellite peak in the Cu 2p spectra suggests the coexistence of Cu_2O and CuO, reflecting mixed oxidation states of copper within the composite. These findings demonstrate the effective incorporation of copper within the TiO_2 matrix while retaining essential fly ash components, including silicon, aluminum, and iron, which contribute to the composite's surface chemistry.

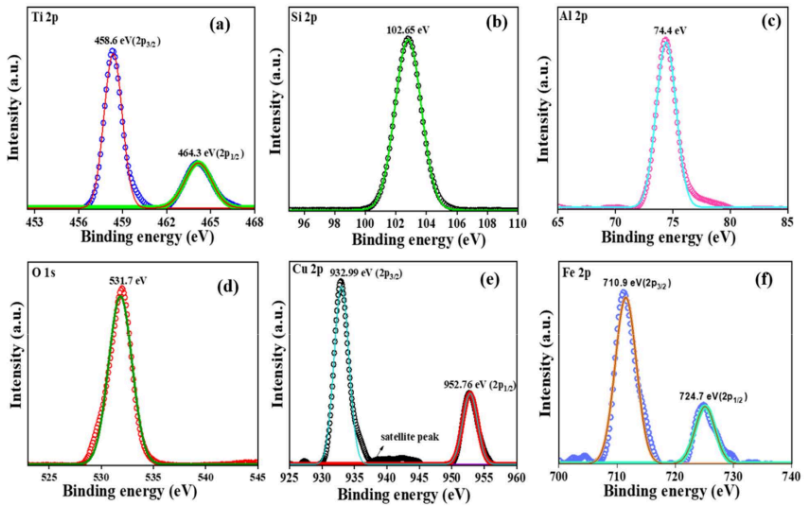

Fig. 3.8. XPS spectra of the synthesized FT-Cu composite: (a) Ti 2p, (b) Si 2p, (c) Al 2p, (d) O 1s, (e) Cu 2p, and (f) Fe 2p.

3.4 Adsorption study

3.4.1 Effect of adsorbent dosage on removal of FB dye

The influence of the FT adsorbent and its composite on the removal efficiency of FB dye is depicted in **Fig. 3.9(a).** The data demonstrate that an increase in adsorbent dosage corresponds to an improvement in removal efficiency. This enhancement is likely attributable to the greater number of available adsorption sites and the increased adsorbent mass. Notably, FT-Cu_1 exhibited significantly higher adsorption efficiency compared to the unmodified FT material. By increasing the catalyst dose from 1 to 6 mg, the percentage removal of FB dye rises from

12 to 60% for FT, 21 to 66% for 0.5wt% FT-$Cu_{0.5}$, 34 to 73% for 2wt% FT-Cu_2 and 44 to 77% for FT-Cu_1 composite. Increasing the adsorbent dose from 5 to 7 mg produces no significant increase in removal efficiency. However, raising the dose over 7 mg reduces efficacy, most likely owing to particle aggregation obstructing the active sites. Thus, the optimal dosage for this experiment was ascertained to be 6 mg of adsorbent.

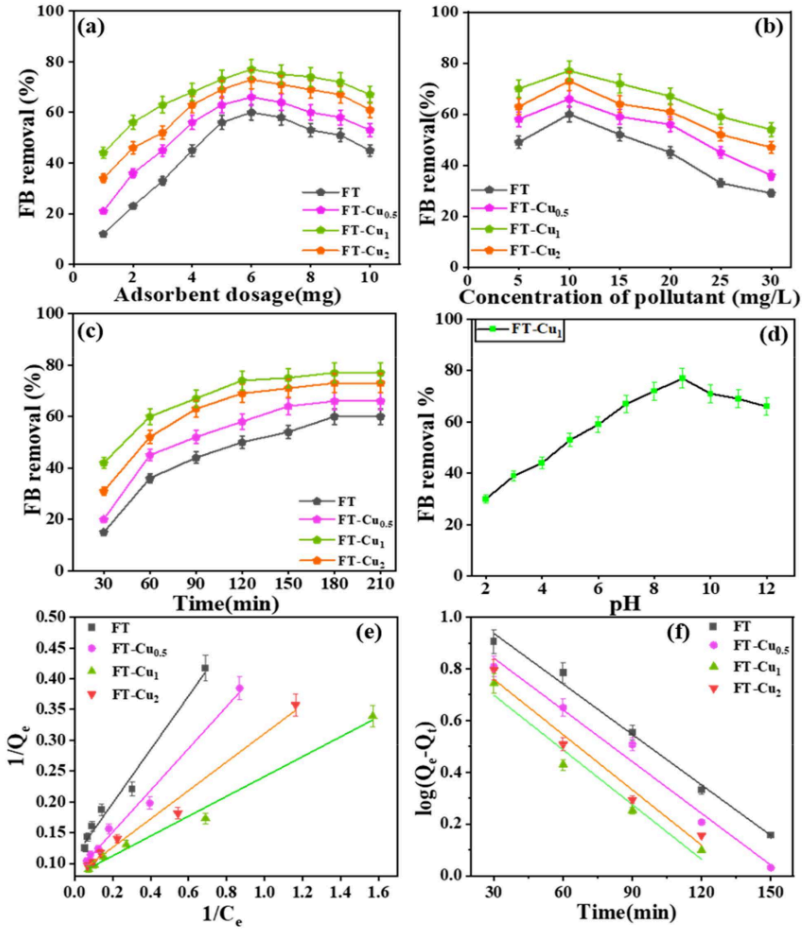

Fig. 3.9 (a) Effect of adsorbent dose on FB removal, (0.006 g/L) (b) Effect of adsorbate concentration, (10mg/L) (c) the effect of contact time, (180 min) (d) effect of pH, (e) Langmuir isotherm adsorption isotherm (f) Pseudo-first-order kinetic model

3.4.2 Impact of initial dye concentration on FB dye removal

In the batch adsorption experiments, the initial FB dye concentration was varied from 5 to 30 mg/L, as shown in **Fig. 3.9(b).** The removal efficiency of the adsorbent decreased with increasing initial dye concentration. At lower dye concentrations, the number of available adsorption sites exceeds the number of dye molecules, resulting in higher removal efficiency. However, beyond a certain concentration threshold, dye molecules outnumber the available adsorption sites, leading to reduced adsorption efficiency. With an increase in FB dye concentration from 5 to 30 mg/L, the percentage removal of dye decreased from 60 to 29% for FT, 66% to 36% for FT-$Cu_{0.5}$, 73% to 47% FT-Cu_2 and 77% to 54%. (FT-Cu_1) composites. This decline in adsorption occurs due to the saturation of active sites with the rise in the FB dye's initial concentration. Therefore, a 10 (ppm) initial concentration of FB dye was taken as an optimum value for further study.

3.4.3 The effect of contact times on removal of FB dye

As shown in **Fig. 3.9(c),** the adsorption of FB dye onto FT and FT-$Cu_{0.5–2}$ gradually improves with increasing contact time at a dye concentration of 10 mg/L. The extended contact period allows more dye molecules to interact with the available adsorption sites, thereby enhancing overall removal efficiency. The adsorption rate decreases when the quantity is raised further until equilibrium is attained after 180 minutes. After 180 minutes, the maximum removal percentage (66, 77, and 73%) was achieved with no further rise in efficiency observed. The dye removal efficacy of the different adsorbents FT and various FT-$Cu_{0.5-2}$ remained consistent between 180 and 210 minutes due to dye saturation of active sites. Compared to FT, and other FT-Cu composites, FT-Cu_1 was the most effective adsorbent that notably removed 77% of FB dye.

3.4.4 The pH effect on FB dye removal

The solution pH plays a crucial role in determining the surface charge of the adsorbent and the ionization state of the dye, both of which significantly impact adsorption efficiency. In this study, adsorption experiments were conducted with an adsorbent dosage of 6 mg at room

temperature, using a fixed adsorbate concentration of 10 ppm and a contact time of 180 minutes. The pH was adjusted using either 0.1M HCl or 0.1M NaOH, and the variation in dye adsorption was analyzed across a pH range of 2 to 12. As shown in **Fig. 3.9(d),** the removal efficiency of FB dye increased gradually with rising pH from 2 to 12. The adsorption behavior of FB dye onto the FT-Cu_1 composite was investigated over this pH range for a duration of 180 minutes. The maximum dye removal efficiency, 77%, was observed at pH 9.

The pH_{pzc} of FT-Cu_1 is 7.4 At lower pH values (acidic conditions), the surface of the FT-Cu_1 composite becomes protonated, acquiring a net positive charge. Simultaneously, the functional groups of the FB dye molecules undergo protonation, leading to a positively charged state for the dye. This results in strong electrostatic repulsion between the positively charged adsorbent surface and the protonated dye molecules.

At higher (alkaline) pH values, the FB dye molecules become either neutral or partially negatively charged due to deprotonation. The FT-Cu_1 composite, possessing a negative surface charge at pH values above its point of zero charge (pHpzc), now engages in electrostatic attraction with the dye molecules, facilitating enhanced adsorption onto the composite surface. The optimal dye removal at pH 9 is due to the enhanced electrostatic interactions between the negatively charged FT-Cu_1 composite (above its pHpzc of 7.4) and the positively charged or partially protonated FB dye molecules. This pH also facilitates secondary interactions, such as hydrogen bonding, between the deprotonated sites on the FT-Cu_1 surface and the dye's functional groups. However, at pH values greater than 9, the dye molecules undergo further deprotonation, becoming neutral or negatively charged, which reduces electrostatic attraction with the negatively charged adsorbent.

3.4.5 Adsorption isotherm studies

Adsorption isotherms are necessary to ascertain the equilibrium interactions between adsorbates and adsorbents. They represent a relationship between the adsorbate concentration in the liquid phase and the amount adsorbed onto the adsorbent surface at a specific temperature. According to the Langmuir isotherm model, the substance forms a monolayer on the surface when each molecule binds to its specific site. The model also states that there are no interactions between the molecules of the adsorbate, indicating that the adsorption of one molecule does not affect the adsorption of any other molecules. The following equation (5) mathematically expresses the Langmuir isotherm:

$$\frac{1}{Q_e} = \left(\frac{1}{K_L Q_{max}}\right) \times \frac{1}{C_e} + \frac{1}{Q_{max}} \qquad (5)$$

$$R_L = \frac{1}{1+K_L C_o} \quad (6)$$

Where Ce (mg/L) is the concentration of adsorbate at equilibrium, Qe (mg/g) is the equilibrium adsorption capacity of the adsorbent, K_L (L/mg) is the Langmuir constant related to the affinity of binding sites, and Q_{max} (mg/g) is the maximum adsorption capacity (mg/g) representing a complete monolayer on the adsorbent surface. C_0 is the initial concentration of the contaminant. [49]. The dimensionless separation factor R_L describes the Langmuir isotherm and demonstrates the favourability of the adsorption process. Adsorption is favourable when the value is 0 to 1 and unfavourable when the value exceeds 1. A value of 1 indicates reversible adsorption, while 0 signifies irreversible adsorption. The graph plotted $1/Q_e$ against $1/C_e$ in **Fig. 3.9(e)** with the intercept and slope used to determine the K_L and Q_{max} values. [50,51]. An empirical model known as the Freundlich isotherm describes heterogeneous surfaces where the heat of adsorption is not distributed uniformly over the surface. The Freundlich isotherm defines the formation of several layers (multilayer adsorption) on a surface, which involves some interaction between the adsorbed molecules. It assumes that the adsorbent surface is assumed to be heterogeneous, indicating significant interactions between the molecules of the adsorbate. The equation represents Freundlich's isotherm:

$$\log Q_e = \log K_F + \left(\frac{1}{n}\right) \log C_e \quad (7)$$

where K_F is the Freundlich constant, which corresponds to adsorption capacity; 1/n is the heterogeneity factor, which is related to adsorption intensity; Q_e (mg/g) is the adsorption capacity at the equilibrium time, and C_e (mg/L) represents the concentration of pollutant in solution at equilibrium [49].Where n>1 indicates a favourable adsorption procedure. The parameters for both models are shown in **Table 3.2**. Langmuir isotherm R^2 values are greater and closer to unity (0.9839-0.99) than Freundlich isotherm R^2 values (0.9405-0.9549), suggesting that the Langmuir model better explains FB dye adsorption. The Freundlich parameter "n>1" in **Table 3.2** indicates that adsorption is non-linear and prefers larger solute concentrations.

Table 3.2. Langmuir and Freundlich adsorption isotherm parameter for FB dye over FT, and various FT-$Cu_{0.5-2}$ composites.

Langmuir model					**Freundlich model**		
Adsorbent	**Q_{max} (mg/g)**	**K_L (L/mg)**	**R_L**	**R^2**	**K_F [mg/g.(L/mg)]$^{1/}$**	**n**	**R^2**

					n		
FT	9.041	0.253	0.1161	0.9839	2.263	2.289	0.9531
FT-Cu$_{0.5}$	12.077	0.243	0.1204	0.9899	2.766	2.083	0.9549
FT-Cu$_1$	25.009	0.495	0.0629	0.99	4.164	2.063	0.9419
FT-Cu$_2$	20	0.345	0.0879	0.9842	3.509	2.283	0.9405

Table 3.3. Kinetic model parameters of adsorption of FB dye over FT-Cu$_{0.5–2}$ composite

(a)	Pseudo-first-order Model			Pseudo-second-order Model		
Adsorbent	**Q_e (mg/g)**	**k_1 (min^{-1})**	**R^2**	**Q_e (mg/g)**	**k_2 (g/mg. min)**	**R^2**
FT	13.548	0.0149	0.9917	9.813	0.0008	0.9805
FT-Cu$_{0.2}$	17.619	0.0154	0.9831	8.613	0.0015	0.9780
FT-Cu$_1$	25.003	0.0161	0.9691	10.384	0.0011	0.9388
FT-Cu$_2$	19.678	0.0163	0.9758	10.351	0.0010	0.9564

3.4.6 Adsorption kinetics

The adsorption kinetics of FB dye on FT-Cu have been evaluated using a pseudo-first-order, pseudo-second-order kinetic model by the following equations (8) and (9).

$$\log(Q_e - Q_t) = \log Q_e - \frac{k_1}{2.303} t \quad (8)$$

$$\frac{t}{Q_t} = \frac{1}{k_2 Q_e^2} + \frac{t}{Q_e} \quad (9)$$

Q_t and Q_e, in mg/g, respectively, indicate the adsorption rates at equilibrium and time t, respectively, whereas k_1 is the first-order rate constant. The second-order rate constant is denoted by k_2. The chemisorption process, in which electrons are transferred from the adsorbent to the adsorbate, is determined to be the rate-limiting phase according to the second-order kinetic model [52,53]. As indicated in **Table 3.3**, the slopes and intercepts of the graphs were used to calculate the parameters for first- and second-order kinetics. The first-order model was closer to unity and had a more significant rate constant value than the second-order model in **Fig. 3.9(f)** This suggests that first-order kinetics govern the adsorption of FB dye onto FT and other FT-Cu composites.

3.5 Photocatalytic studies

3.5.1 Photocatalytic degradation under visible light

Fig. 3.10(a, b) illustrates variations in the absorption spectra due to the FB dye degradation by FT-Cu_1 composite at varying irradiation times under visible light. During adsorption and photocatalytic degradation, the typical maximum absorption peak of FB dye is found at 546 nm, and its absorption intensity steadily decreases with increasing illumination time. In the visible light photodegradation of FB dye resulted in 94% removal by the FT-Cu_1 catalyst, which is significantly higher than the removal rate achieved via adsorption only. After 180 minutes of degradation under visible light, the dye solution shifted from dark pink to colourless, further confirming the significant removal of dye by photocatalytic degradation **(Fig. 3.10).** This suggests that for complete removal of dye, photocatalytic degradation plays a significant role than adsorption whereas, in the absence of a photocatalyst, only 14% removal of FB dye was achieved within 180 minutes under visible light. In **Fig.3.10(a)** the dark adsorption of fuchsin blue dye in the FT-$Cu_{0.5-2}$ composite is driven by the porous nature of fly ash, which offers a high surface area for adsorption through electrostatic and van der waals forces. Copper enhances this by forming coordination bonds and modifying the surface charge of TiO_2, making the composite more attractive to fuchsin dye molecules. Together, these interactions allow for effective dye binding which results in effective removal of dye under dark conditions. The absorption spectra of FB dye after photodegradation by bare FT and FT-Cu exposed to 180 minutes of visible light are shown in **Fig. 3.10(c)**. The photoactivity of the FT composite was significantly increased after 1wt% Cu photo-deposition over fly ash-TiO_2 composite, displaying the highest photocatalytic activity. The time course duration plot **Fig. 3.10(d)** and kinetic graphs **Fig. 3.10(e)** were analyzed to validate the optimal amount of Cu deposition on FT for FB dye degradation under visible light. The photodegradation followed a pseudo-first-order kinetic model, as the reaction rate is only influenced by the concentration of the FB dye without having any change in the concentration of water and oxygen. Additionally, with light intensity kept constant and the amount of FT-Cu composites is fixed (6 mg) and thus negligible in rate variation, as shown in equation (10):

$$\ln (C_o / C_t) = kt \qquad (10)$$

Table 3.4. (a) Kinetic parameter of pseudo first order model of various photocatalysts under visible light (b) Kinetic parameter of pseudo first order model of various photocatalysts under sunlight.

(a)	Pseudo-first-order Model (visible light)	
Photocatalyst	**k_1**	**R^2**
FT	0.0008	0.9922
FT-Cu$_{0.2}$	0.0015	0.9903
FT-Cu$_1$	0.0031	0.9921
FT-Cu$_2$	0.0020	0.9915

(b)	Pseudo-first-order Model (sunlight)	
Photocatalyst	**k_1**	**R^2**
FT	0.0009	0.9944
FT-Cu$_{0.2}$	0.0023	0.9906
FT-Cu$_1$	0.0016	0.9900
FT-Cu$_2$	0.0021	0.9970

Where C_0 is the initial concentration of the FB dye at time zero min and C_t at reaction time t and k is the rate constant (min^{-1}) [54,55].The pseudo-first-order rate constant and square of linear correlation coefficient (R^2) of FT and various FT-Cu composites under visible light and sunlight are shown in **Table 3.4 (a, b).** The rate constant for FT-Cu_1 composites (0.0031 min^{-1}) is higher than that for FT composites (0.0008 min^{-1}), indicating that the presence of copper enhances the photocatalytic activity of TiO_2, potentially due to improved charge separation and increased light absorption. The histogram in **Fig. 3.10 (f)** compares the percentage removal of FB dye by FT and FT-Cu during dark adsorption and degradation under visible light.

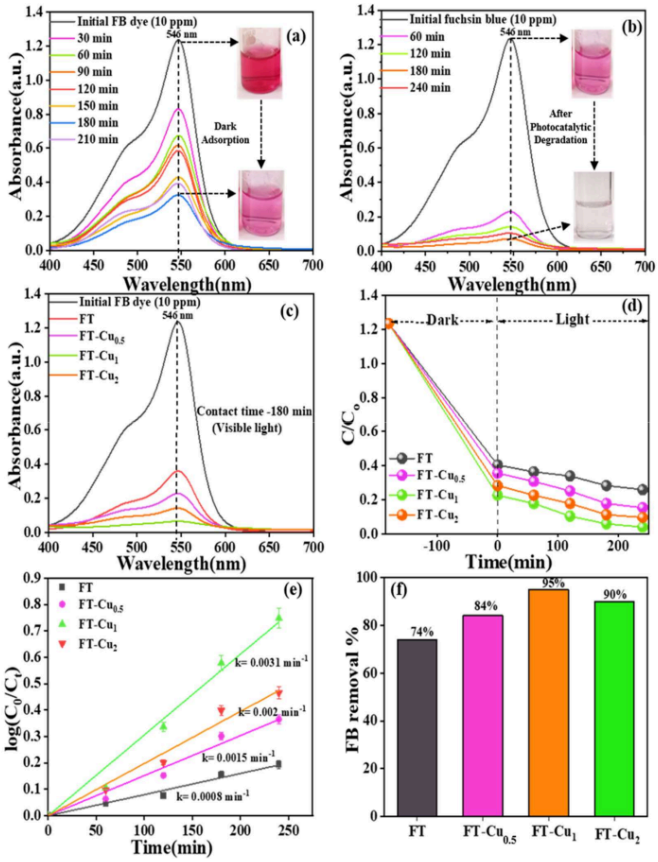

Fig. 3.10. Changes in the colour and absorption spectra of fuchsin blue dye: (a) dark adsorption, (b) photocatalytic degradation by the FT-Cu$_1$ composite at various time intervals, (c) degradation performance of different wt% FT-Cu composites after 180 min, (d) time-dependent kinetic plots, (e) pseudo–first-order kinetic fitting, and (f) FB degradation efficiency of various composites under visible-light irradiation.

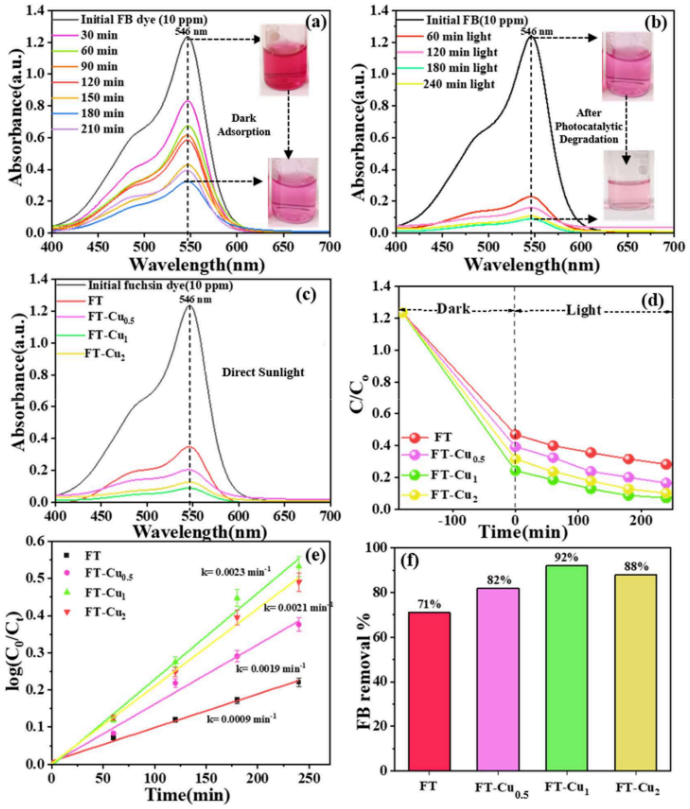

Fig. 3.11 Changes in the colour and absorption spectra of FB dye (a) dark adsorption (b) after photocatalytic degradation by FT-Cu_1 composite under different periods and (c) different wt% Cu-FT composites after 180 min (d) time course kinetic plots (e) Pseudo first-order model and (f) FB degradation efficiency by various composites under direct sunlight irradiation.

3.5.2 Photocatalytic degradation of FB under direct sunlight

To increase the usefulness and applicability of Earth's most abundant energy source,

photocatalytic degradation of FB dye was conducted under direct sunshine. Different test tubes containing 6 mg of catalysts (FT/FT-Cu) and 10 ml FB dye (10 ppm) are kept under sunlight on 21-05-24 for different periods (180 min) with constant magnetic stirring. The ambient temperature fluctuated between 35°C and 40°C. and solar intensity of 670 Wm^{-2}, June, 2024. In **Fig. 3.11(a),** the FB dye absorption spectra change from dark pink to light pink, indicating 77% removal, while **Fig. 3.11(b)** shows 92% removal, and the colour changes from light pink to colourless under sunlight. The UV-visible absorption spectra shown in **Fig. 3.11(c)** illustrate the relative variations in the absorbance of FB dye after it is photodegraded by bare FT and different FT-Cu nanocomposites exposed to sunlight for 180 minutes. The photoactivity of the FT composite was significantly increased by Cu loading; The change in colour of FB dye showed that photocatalytic activity increased after 1 wt% Cu deposition over FT catalysts and declined after that. The time course plot **Fig. 3.11(d)** and kinetic graphs **Fig. 3.11(e)** were shown to confirm further the optimal amount of Cu loading on FT composite for FB degradation. According to the findings, the photodegradation process follows a pseudo-first-order rate law and similarly FT-Cu_1 composites have a higher rate constant value (0.0023 min^{-1}) as compared to FT composite (0.0009 min^{-1}). A histogram in **Fig. 3.11(f)** shows the comparative percentage removal of FB dye by FT and different FT-Cu composites. The 1wt% Cu-loaded FT composite exhibited the highest percentage removal of 92% relative to other Cu-loaded FT catalysts under identical experimental conditions.

3.5.3 Active species detection

In the scavenging experiments, different scavengers were used to investigate the roles of active species in the photocatalytic degradation of FB dye. Argon gas purging was employed to remove dissolved oxygen from the reaction mixture, thereby suppressing the formation of superoxide anion radicals ($O_2^{\cdot -}$), which led to a significant decrease in degradation efficiency to 18%. Ethanol and isopropanol (IPA) were used as hydroxyl radical (·OH) scavengers, reducing the dye degradation efficiency to 17% and 20%, respectively, by neutralizing the reactive species. Furthermore, NH_4SCN acted as a hole (h^+) scavenger, preventing the oxidation of water molecules and reducing the degradation efficiency to 11%. These findings highlight the crucial involvement of superoxide anion radicals, hydroxyl radicals, and holes in the photocatalytic degradation process [56] .The percentage degradation of FB dye by FT-Cu_1 with and without the addition of different scavengers is shown in **Fig. 3.12(a).** EDTA, IPA, and NH_4SCN reduced FB dye degradation from 94% to 17%, 20%, and 11%, respectively.

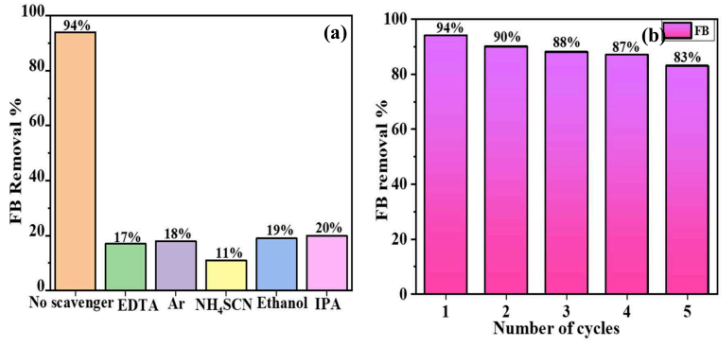

Fig. 3.12 (a) Study the effect of different hole scavenger additions on the FB photocatalytic degradation efficiency and (b) reusability test by FT-Cu_1 under visible light irradiation.

3.6 . Proposed photocatalytic degradation mechanism

The photocatalytic process over FT-Cu_1 has several important stages that improve composite performance and stability. Cu-photo deposited TiO_2 nanoparticles are uniformly spread across the fly ash surface, stabilizing the catalyst and increasing catalytic reaction surface area. Visible light generates electron-hole pairs in TiO_2 in the composite. Holes stay in the valence band while photoexcited electrons enter the conduction band. Cu nanoparticles on TiO_2 capture photoexcited electrons, minimizing electron-hole pair recombination. Charge separation is essential to produce reactive oxygen species (ROS), such as superoxide radicals ($\bullet O_2^-$) and hydroxyl radicals ($\bullet OH$), through interactions with oxygen and water. Copper doping lowers the bandgap of TiO_2, allowing it to absorb visible light and create electron-hole pairs. FB dye molecules on FT/FT-Cu_1 catalysts can be degraded by extremely reactive ROS. This breakdown breaks the dye into smaller, less toxic molecules and can lead to complete mineralization into CO_2, NO_3^-, and H_2O. The porous structure and large surface area of fly ash increase adsorption of dye improving process efficiency [48, 49]. As demonstrated in **Scheme 3.1**, this synergistic interaction creates a more efficient and sustainable photocatalytic system for the breakdown of FB dye.

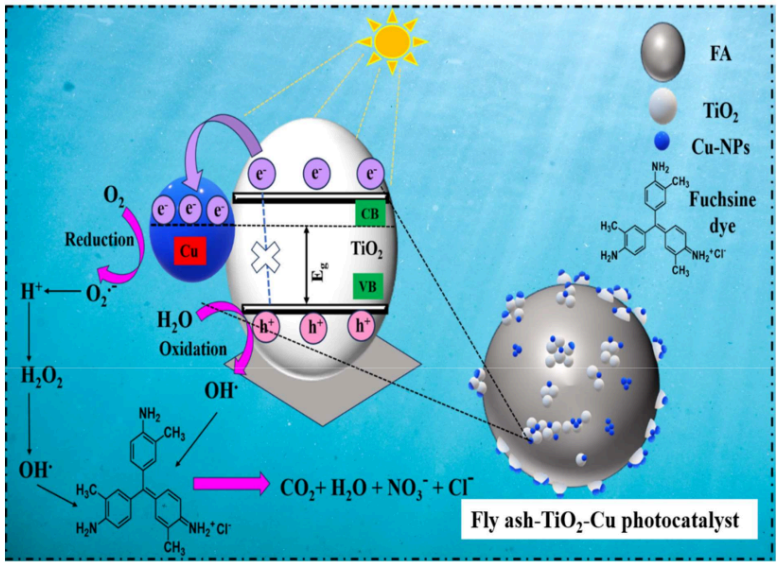

Scheme 3.1. The proposed photodegradation mechanism of FB dye by FT-Cu composite under solar/visible light irradiation.

3.7 Identification of intermediate photoproducts during FB dye degradation pathway

After photocatalytic degradation of FB dye by FT-Cu_1 catalysts under 180 min visible light irradiation, the reaction mixture is subjected to centrifuge and filtered to separate the catalyst powders. The clear supernatant solution is used for HRMS analysis to investigate the various intermediate photoproducts formed after FB dye degradation. The separation of the mass(m)/charge(z) ratio was studied using the HRMS technique to determine the molecular formula. For the FB ion 330, the exact m/z measurement was 330.0928. Mass spectrometry analysis for basic FB dye determined two possible degradation pathways, as shown in **Fig. 3.13(a, b)**. These pathways show how different reactions involving ring-opening reactions, oxidation, demethylation, and hydroxylation can cause basic FB dye molecules to break down into various intermediates and decompose to NO_3^-, CO_2 and H_2O etc.

First, FB (m/z = 365.91) dye is demethylated to produce Product B (m/z = 316.18) through pathway 1. After further demethylation, Product B yields Product C (m/z = 302.17). Product C uses a ring-opening process with reactive oxygen species (•O_2- and •OH) to produce Product

D (m/z = 205.11). Product D is then oxidized to produce 3-Heptynoic acid (m/z = 126.07), which is Product E. Ultimately, Product E 3-Heptynoic acid (m/z = 126.07) mineralizes to form H_2O, CO_2, and a few inorganic ions. In pathway one, the other side of product C (m/z = 302.17) experiences the ring-opening reaction, changes into product H (m/z = 282.16), and then changes again into NO_3, CO_2 and H_2O. Product F forms via Pathway 2, i.e., carbinol of pararosaniline (m/z = 347.21), from Product A (m/z = 330.09), which is the result of ionizing FB dye, through hydroxylation. Product F undergoes oxidation to yield Product G (m/z = 223.14) and finally Product G mineralizes to form H_2O, CO_2, and specific inorganic ions [57].

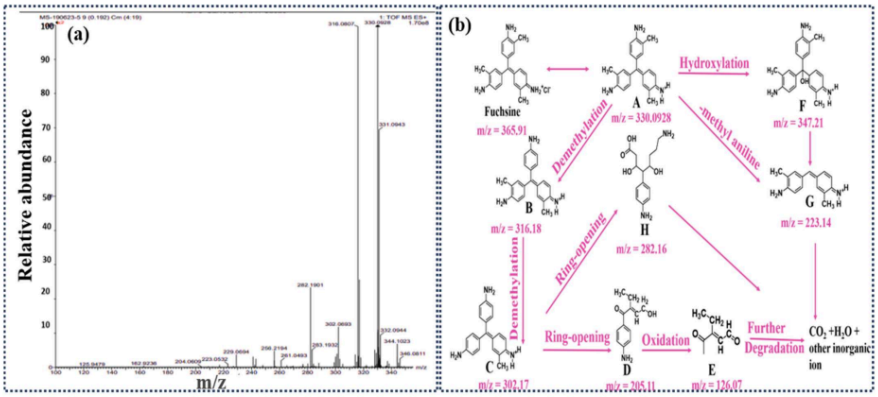

Fig. 3.13 (a) High-Resolution Mass Spectra (HRMS) and (b) identification/degradation pathways of different intermediate photoproducts formed during photocatalytic degradation of FB dye by FT-Cu_1 nanocomposite under 180 min visible light irradiation.

3.8 . Photostability and reusability of prepared photocatalyst

For real-world applications, photocatalyst durability must be assessed along with catalytic performance. The reproducibility and photostability of the synthesized FT-Cu_1 catalyst were tested through consecutive recycling experiments for the photodegradation of FB dye under identical experimental conditions. The catalyst underwent multiple photochemical reactions, and after each cycle, it was centrifuged, washed, and dried before being reused in the next cycle. This process is illustrated in **Fig. 3.12(b),** where the FT-Cu_1 catalyst showed excellent effectiveness when subjected to visible light irradiation in the 1st cycle, degrading the FB dye

94% after 180 minutes. Despite undergoing five continuous cycles of visible irradiation, the degradation efficiency stays relatively close to 83%, and its catalytic performance remains largely unaffected by repeated use, suggesting that the composite degrades the dye effectively and FT-Cu_1 is a reusable catalyst. The decrease in removal efficiency from 94% to 83% can be ascribed to the unavoidable loss of catalyst during the recovery process. Additionally, over the recycling cycles, some unreacted intermediates may have adhered to the catalyst's surface, blocking certain active sites and pores and contributing to the decline in its performance. The 1wt% Cu deposited on fly ash-TiO_2 composite has a strong reusability performance, as evidenced by the consistent degrading efficiency over several cycles. Comparison of percentage removal of Fuchsin blue dye by various composites and Cu- loaded TiO_2-fly ash composites is shown in **Table 3.5.**

To confirm the adsorption and photodegradation of FB on the FT-Cu surface, XPS survey spectra were recorded following the adsorption and degradation processes **(Fig. 3.14).** The analysis revealed notable changes in the FT-Cu composite. After adsorption, the appearance of an N 1s peak at 399 eV confirmed the incorporation of nitrogen from the dye, while an increase in the C 1s peak at 284.6 eV indicated the adsorption of organic dye molecules. Following photodegradation, the disappearance of the N 1s peak signified the breakdown of nitrogen-containing group [58] and the reduction in C 1s peaks, particularly those associated with aromatic structures, confirmed the degradation of the dye into smaller fragments or mineralized products. These results highlight the dual functionality of the FT-Cu composite in effectively adsorbing and degrading fuchsine dye.

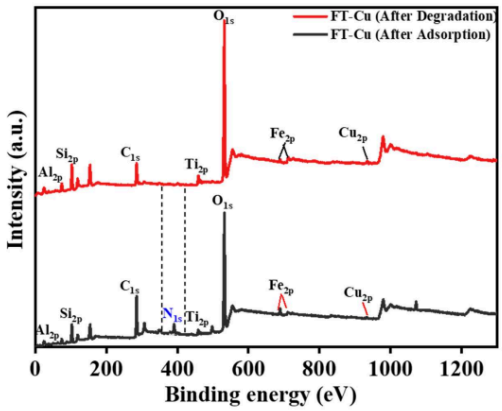

Fig. 3.14. XPS survey spectra of the FT-Cu composite after the adsorption and degradation of fuchsin dye.

Table 3.5. Comparison of percentage removal of fuchsin blue dye by various composites and fly ash-TiO_2-Cu composites.

Adsorbent/Catalyst	**% Removal of FB dye**	**References**
Fe-ZSM-5 zeolite	99.6%	[59]
Sugarcane bagasse	97%	[60]
Mg- Fe TiO_2 nanocomposites	95%	[61]
g-C_3N_4-modified ZnO nanocomposite	70%	[62]
FT-Cu_1 nanocomposite	95%	Present work

3.9 Conclusion

Cu-deposited fly ash-TiO_2 (FT-Cu) composite was synthesized successfully and assessed by different characterization techniques. The FT-Cu composite exhibited superior adsorption due to the presence of fly ash containing other metal oxides and photo-catalytic activity due to the presence of TiO_2 and copper. Among the prepared composites, the maximum adsorptive removal (77%) of FB dye was achieved by FT-Cu_1 composites which followed the Langmuir isotherm confirming monolayer adsorption. 1wt % Cu-deposited fly ash-TiO_2 (FT-Cu_1) attained the maximum removal of 92% of FB dye under solar light and 94% under visible light in less than 180 minutes whereas the (fly ash–TiO_2) FT composite without Cu showed only 71% removal under sunlight and 74% under visible light. It revealed that Cu deposition not only improved the photocatalytic activity of fly ash-TiO_2 catalysts but it also sensitized the absorption of visible/solar light. The XPS results of the FT-Cu composite, including the analysis before and after illumination, provided valuable insights into the interactions between the catalyst and the dye, reinforcing the role of surface chemistry in the photocatalytic process. Furthermore, HRMS results revealed that the composites decomposed the FB dye into smaller molecules. Based on the identification of various degraded photoproducts, band energy analysis, and hole scavenger experiments, a feasible photocatalytic mechanism was proposed where the different reactive oxygen species, OH radical and superoxide anions played a vital contribution in the FB dye degradation process. The resulting Cu-loaded fly ash-TiO_2 composite demonstrated high durability and photostability throughout consecutive degradation cycles. Thus, the synergistic effects of fly ash incorporation and Cu modification within the fly ash–TiO_2 heterostructure highlight its potential as an efficient photocatalyst for complete mineralization of hazardous pollutants in industrial wastewater under natural sunlight, supporting a more environmentally sustainable remediation strategy.

Chapter-4

Fabrication and evaluation of ZSM-5-fly ash–TiO_2–Cu hybrid catalysts for efficient photocatalytic and adsorptive removal of crystal violet dye

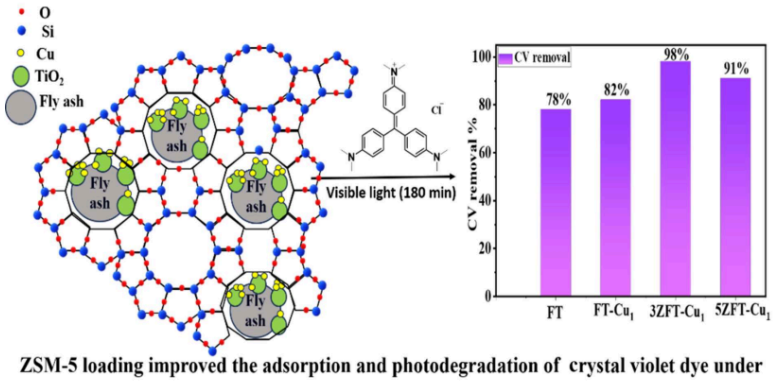

ZSM-5 loading improved the adsorption and photodegradation of crystal violet dye under visible light

Schematic summary

4.1 Introduction

Water contamination from organic dyes is a serious issue that endangers the ecosystem. Industries including paper, plastics, leather, textiles, and pharmaceuticals discharge large volumes of wastewater tainted with dyes into natural water pools. [1,2] The toxic organic dyes often disrupt the ecosystems by lowering the oxygen levels and killing the aquatic life. [3,4]. Human exposure to polluted water can cause a range of health problems. Certain dyes are carcinogenic, mutagenic, and teratogenic, posing long-term risks such as cancer and genetic mutations. Drinking contaminated water can cause gastrointestinal disorders, damage to the kidneys, and liver. [5–7].

Crystal violet (CV) is a dye derived from aniline that has been widely utilized as a disinfectant, a staining agent in biomedical applications, a pH indicator, and a colouring agent in the textile industry [8]. It is a potent mutagen and has been classified as a potential carcinogen. Excessive exposure to CV dye can cause cancer, organ damage, and reproductive disorders over time. Direct skin contact might irritate the skin with respiratory difficulties [9]. Thus, developing efficient, cost-effective, and ecologically sustainable techniques for extracting crystal violet from wastewater is critically important.

Numerous approaches, such as adsorption, electrochemical processes, photocatalytic degradation, and biological methods, have been established to remove organic dyes from wastewater. Adsorption is the most beneficial of these techniques because of its low cost, ease of setup, user-friendliness, low production of harmful byproducts, wide availability of

adsorbent materials, and ease of recovery [10]. However, a key challenge in this process is the saturation of the adsorbent, which must then be either regenerated or replaced. In contrast, photocatalysis can decompose particles that are challenging to remove from treated water through conventional methods completely. The photocatalysis process breaks down various contaminants into harmless compounds like carbon dioxide and water [11]. This technique could remarkably decrease the operation cost due to low energy consumption. Combining photocatalytic decomposition with adsorption would be a practical approach to enhance the degradation of dyes.

Titanium dioxide (TiO_2) is the best-known and widely studied photocatalyst for the degradation of various toxic organic pollutants, particularly due to its high oxidative power upon illumination. It is a non-toxic, chemically inert, low-cost, and biocompatible material with interesting physical, optical, and electrical properties. UV radiation activates TiO_2 and causes ROS, such as superoxide ions and hydroxyl radicals, potent oxidizers that may quickly break down a range of organic contaminants into nontoxic inorganic compounds like CO_2 and H_2O [12]. Despite its potential, the practical use of TiO_2 is hindered by its wide band gap of about 3.2 eV, which confines its photoactivation primarily to the ultraviolet region of the spectrum, which constitutes only about 5% of sunlight. Additionally, the fast recombination of photo-induced electron–hole pairs significantly diminish its overall photocatalytic efficiency [13].

The best way to get around these restrictions is by metal doping. A practical method for enhancing TiO_2 involves doping with transition metals such as nickel (Ni), copper (Cu), and silver (Ag), which induces a substantial modification of its optical absorption characteristics. These metal dopants significantly reduce the band gap of TiO_2 allowing photoexcitation in visible light (red shift) while also preventing the recombination of photogenerated electron-hole pairs [14,15]. It is not easy to produce stable, reasonably priced doped nanomaterials with distinct properties that can efficiently absorb visible light. Among the various transition metals, copper (Cu) is a particularly strong dopant due to its special characteristics and capacity to promote charge separation and transfer. Doping of copper (Cu^{2+}) produces additional energy levels in the TiO_2 band gap, thereby increasing visible light absorption and photocatalytic activity. Moreover, Cu^{2+} ions favour photogenerated electron-hole separation and reduce charge carrier recombination by functioning as electron traps [16,17]. Recent research have emphasised the impact of multi-metal doping and surface modification in increasing photocatalytic stability. Sun et al.[18] developed Cu–Mn catalysts for carbon monoxide (CO) removal using a co-precipitation approach and comprehensively examined the influence of additional metal dopants (Fe, Ce, and Sn), precipitation temperature, and hydrophobic

modification with polyvinyl alcohol (PVA) and polyvinylpyrrolidone (PVP). The catalyst containing Ce prepared at 70 °C showed roughly 50 % greater CO removal efficiency than the other samples and, after PVA/PVP treatment, retained about 85 % removal efficiency under 90 % relative humidity, indicating excellent water resistance.

One technique is to anchor TiO_2 particles onto high-surface-area supports, such as ZSM-5 zeolite, a synthetic aluminosilicate with a well-ordered microporous framework, excellent thermal and chemical stability, and the ability to modify its hydrophilic or hydrophobic characteristics [19]. ZSM-5 not only enhances adsorption by trapping organic pollutants near the photocatalytic surface but also aids in better dispersion of TiO_2 nanoparticles, preventing aggregation and promoting efficient charge transfer. Its shape-selective pore structure and strong adsorption affinity make ZSM-5 particularly effective in capturing dye molecules such as crystal dyes before their degradation [20].

Fly ash, a solid byproduct of burning coal in thermal power plants, is frequently employed as a support material in photocatalytic applications because of its abundance, affordability, and favourable chemical compatibility with metal oxides. Silica, alumina, and other inorganic oxides comprise most of its composition. It forms a structurally rigid and chemically stable matrix that permits the uniform dispersion of photocatalytic particles such as TiO_2. This homogeneous distribution not only prevents nanoparticle aggregation, but it also enhances the composite's surface area and structural robustness, resulting in increased photocatalytic activity [21]. The integration of fly ash with ZSM-5 and Cu-doped TiO_2 results in a multifunctional composite material that offers improved surface area, enhanced pollutant adsorption, enhanced photocatalytic performance when exposed to visible light, and cost-effectiveness.

Over the last few years, several research studies have investigated photo catalytic degradation of organic pollutants under UV and visible light using ZSM-5/TiO_2, TiO_2-supported fly ash, and metal-modified fly ash- TiO_2 composites. Mergenbayeva et al. [22] developed TiO_2 /zeolite composites, TiO_2 /Z-45 (TZ) and TiO_2 /ZSM-5 (TZSM), by mechanical mixing and liquid impregnation processes. These composites were used in the photocatalytic breakdown of sulfamethoxazole (SMX) in water using UV light. Photocatalytic testing revealed that TZSM2600 and TZSM1450 produced 65% and 67% mineralisation of SMX, respectively, after 120 minutes. Al-Wasidi et al. [23] synthesized ZSM-5/TiO_2/Ni photocatalyst to degrade methylene blue dye under ultraviolet light. The ZSM-5/TiO_2/Ni nanocomposite had a maximum degradation efficiency of 99.17% for 50 mL of 15 mg/L methylene blue dye under 140 minutes. Zhu et al. [24] developed a copper (II)-modified ZSM-5/TiO_2 composite using a

sol–gel technique combined with an impregnation method. This composite was applied for the photocatalytic degradation of ammonia gas under visible light conditions. The catalyst containing 0.5wt% Cu exhibited the highest efficiency, removing nearly 94.2% of ammonia within 60 minutes of exposure to visible light. Stojanović et al. [25] synthesized TiO_2/zeolite composites via a solid-state dispersion technique, incorporating synthetic and natural zeolites with P25 TiO_2 and TiO_2 nanocrystals derived from nanotubes. Among the tested materials, the TiO_2 /ZSM-5 (P25) composite demonstrated the most effective photocatalytic performance under simulated solar light, achieving nearly 94% removal of atenolol within 70 minutes.

In the previous work, Cu photo-deposited fly ash-TiO_2 composite was synthesized and its performance was evaluated for removing fuschin blue dye [26]. In the present work, the influence of ZSM-5 zeolite loading on Cu photo deposited fly ash-TiO_2 composite for degradation of crystal violet dye under visible and solar light is investigated. However, the novelty of the present work lies in the design and application of ZSM-5–loaded fly ash–TiO_2–Cu (ZFT-Cu) hybrid composites, which to the best of our knowledge have not been reported earlier. The composite was prepared using the wet impregnation process. A synergistic effect is produced when visible-light-active flyash-TiO_2-Cu and high-surface-area, highly porous ZSM-5 are combined. The novel composite catalyst is used to destroy the CV dye molecules once they have been adsorbed onto the surface of the ZSM-5. Additionally, the photocatalytic degradation of crystal violet under sunlight was investigated to evaluate the impact of ZSM-5 incorporation onto copper photo-deposited TiO_2/fly ash composite. The degradation of crystal violet using ZFT-Cu composites has not been reported elsewhere, thereby establishing the novelty and significance of this research. This study contributes to developing efficient, environmentally friendly, and cost-effective composites for the removal of dye-contaminated wastewater.

4.2 Materials and methods

4.2.1 Materials and reagents

All chemicals were of analytical grade and used as received, without further purification. ZSM-5 was procured from Thermo Fisher Scientific India Pvt. Ltd. Fly ash was collected from the Rajpura Power Plant in India. Deionised water, with a conductivity of 35 µS cm^{1} at 25 °C, was produced using a Milli-Q ultrafiltration system (Millipore). Titanium butoxide ($Ti(OC_4H_9)_4$, 97%) and didecyl dimethyl ammonium chloride ($C_{22}H_{48}ClN$) were obtained from Sigma-Aldrich, India. Loba Chemie, India, supplied acetic acid ($C_2H_4O_2$, 99.8%), ethanol (C_2H_5OH,

99.9%), cupric nitrate trihydrate ($Cu(NO_3)_2 \cdot 3H_2O$, 99.5%), isopropyl alcohol (C_3H_8O, 99.5%), and crystal violet dye ($C_{25}H_{30}ClN_3$).

4.2.2 Techniques Used for Characterizing the Synthesized Samples

Diffraction images were recorded using an X-ray diffractometer (Smart Lab SE) equipped with Cu-Kα radiation (λ = 1.54 Å) and operated at 45 kV to analyze the crystalline structure. Scans were performed across a 2θ range of 5° to 80°, using a 10 mm slit, at a resolution of 0.01° per scan and a scan speed of 5 ° min^{-1}. Field emission scanning electron microscopy (FESEM, JEOL JSM-7600F, JAPAN, operated at 30 kV) was used to examine the surface morphology and microstructure of the catalyst. Elemental composition and spatial distribution were analysed using energy dispersive spectroscopy (Bruker EDS). FTIR spectra of the synthesized samples were obtained using an Agilent FTIR spectrophotometer. The BET Autosorb iQ (Quanta chrome Instruments, version 3.01, USA) was employed to assess the surface area and pore size distribution of the samples. A JASCO V-750 diffuse reflectance spectrophotometer (Japan) was used to determine the optical properties, employing $BaSO_4$ as the standard reference material.

4.2.3 Synthesis of ZSM-5 loaded fly ash-TiO_2-Cu (ZFT-Cu_1) composite

A wet impregnation method was used to produce the ZSM-5 modified fly ash-TiO_2-Cu (ZFT-Cu_1) composites. 500 mg of the Cu-deposited fly ash–TiO_2 (FT–Cu_1) composite, prepared as described in chapter 3 (section 3.2.3), was used for the experiment. On the FT–Cu_1 composite, ZSM-5 was added in varying weight percentages (1wt%, 3wt%, and 5wt%). After a thorough stirring for 2 hours followed by centrifugation process, the components were washed with ethanol and deionized water multiple times to remove any last traces of impurities. After washing, ZSM-5 modified composites were calcined at 400°C to strengthen their structure after being dried for 24 h at 70°C. The substance was ground into a fine powder using a mortar and pestle. 1ZFT-Cu_1, 3ZFT-Cu_1, and 5ZFT-Cu_1 were the end products having loaded with 1wt%, 3wt%, and 5wt% ZSM-5 zeolite onto the fly ash-TiO_2-Cu (ZFT-Cu_1) composite respectively.

4.2.4 Adsorption in Dark and Photocatalytic Studies

Batch adsorption studies were carried out to evaluate the adsorption performance of FT-Cu_1 and (3–5 wt%) ZFT-Cu_1 composites toward crystal violet (CV) dye. A 10 mL CV solution with initial concentrations of 3–15 mg/L was contacted with adsorbent dosages of 1–10 mg for

contact times ranging from 30 to 240 min. The effect of solution pH (2–12) was also examined. All experiments were conducted at room temperature (25 ± 2 °C) under dark conditions with continuous stirring. After adsorption, the suspensions were centrifuged, and the residual CV concentration was measured using a UV–visible spectrophotometer at λ_{max} = 598 nm, as determined from the calibration curve. The adsorption capacity and removal efficiency were calculated using the equations 1 and 2 as described in Chapter 3 (Section 3.2.5) .

Under visible-light, photocatalytic degradation experiments were carried out to evaluate the degradation of crystal violet (CV) dye using FT-Cu_1 and (3–5 wt%) ZFT-Cu_1 composites. The reaction mixtures were irradiated using a Wipro Garnet B22 50-W LED bulb (λ > 360 nm) under continuous magnetic stirring for predetermined time intervals. Prior to light irradiation, the suspensions were stirred in the dark for 180 min to establish adsorption–desorption equilibrium between the catalyst and CV dye molecules. At specified irradiation times, the samples were withdrawn and centrifuged at 8000 rpm for 8 min to separate the photocatalyst. The residual CV dye concentration in the clear supernatant was quantified using a UV–visible spectrophotometer. The photodegradation efficiency was calculated using the equations 3 and 4 as described in chapter 3 (Section 3.2.6).

4.2.5 Adsorption Isotherm Models

To determine the effectiveness of the adsorption process, the data were fitted to various isotherm models, including Langmuir, Freundlich, Temkin, and Dubinin-Radushkevich (D–R) isotherms. The corresponding models are expressed as:

Langmuir isotherm model: $$\frac{1}{Q_e} = \left(\frac{1}{K_L Q_{max}}\right) \times \frac{1}{C_e} + \frac{1}{Q_{max}} \quad (1)$$

Freundlich's isotherm model: $$\log Q_e = \log K_F + \left(\frac{1}{n}\right) \log C_e \quad (2)$$

Temkin isotherm model: $$Q_e = B_T \ln A + B_T \ln C_e \quad (3)$$

Dubinin-Radushkevich (D-R) isotherm model: $$\ln Q_e = \ln Q_m - \beta\varepsilon^2 \quad (4)$$

Here, Q_e (mg/g) is the quantity of pollutant adsorbed at equilibrium, and C_e (mg/L) denotes the pollutant concentration at equilibrium. Q_{max} (mg/g) is the maximum adsorption capacity. The Langmuir constant, K_L (L/mg), signifies the affinity between the substance that adsorbs and the adsorbate that occurs at the active binding sites. To what extent the adsorption process is favoured is determined by the Langmuir isotherm, which is in turn described by the dimensionless separation factor (R_L) [27]. The model constants, K_L and K_F, are obtained by

fitting the experimental data to the linear forms of the isotherms [28]. The quantities A (L/g) and B represent the Temkin isotherm constant and the adsorption heat, respectively. In this context, β is the Dubinin-Radushkevich isotherm constant (mol²/kJ²), and ε is the Polanyi potential.

4.2.6 Adsorption Kinetic Models

The adsorption kinetics were analyzed using pseudo-first-order, pseudo-second-order, intraparticle diffusion, and Elovich models:

Pseudo-first order kinetic model: $\log(Q_e - Q_t) = \log Q_e - \frac{k_1}{2.303} t$ (5)

Pseudo-second order kinetic model: $\frac{t}{Q_t} = \frac{1}{k_2 Q_e^2} + \frac{t}{Q_e}$ (6)

Intra-particle diffusion kinetic model: $Q_t = K_{dif}\sqrt{t} + C_i$ (7)

Elovich kinetic model: $Q_t = \frac{1}{\beta}\ln(\alpha\beta) + \frac{1}{\beta}t$ (8)

Q_t and Q_e denote the adsorption capacity at time t and equilibrium, respectively. C_t and C_o denote the pollutant concentrations at time t (min) and at the initial time, respectively. The rate constant for the pseudo-first-order model is k_1 (min^{-1}), and for the pseudo-second-order model is k_2 (g mg^{-1} min^{-1}). In this model, K_{dif} (mg $g^{-1}min^{-0.5}$) represents the intra-particle diffusion rate constant, whereas C_i (mg g^{-1}) measures diffusion resistance. In the Elovich model, α (mg g^{-1} min^{-1}) represents the initial adsorption rate, while β (g mg^{-1}) is the desorption constant [29]

4.3 Results and discussion

4.3.1 XRD analysis

The XRD image of the synthesised FT, FT-Cu_1, and ZFT-Cu_1 nanocomposites, along with their crystal planes and associated diffraction angles, is shown in **Fig. 4.1**. The FT sample has a diffraction peak at 25.3° of 2θ, which corresponds to the anatase (101) phase. TiO_2 verifies the presence of the anatase phase besides the crystalline phases that are frequently found in fly ash, such as hematite (Fe_2O_3), magnetite (Fe_3O_4), mullite ($Al_6Si_2O_{13}$), and quartz (SiO_2) [30].

The appearance of this peak confirms the successful integration of TiO_2 [31] onto the fly ash surface, signifying effective composite formation. There are no noticeable diffraction peaks in the FT-Cu_1 photocatalysts' XRD patterns that correspond to the Cu co-catalyst. This finding is in agreement with other studies that found that metal nanoparticles at low concentrations (often

less than 5wt%) are often undetected when analysed by XRD [26]. The ZFT-Cu_1 composite similarly lacks distinct peaks associated with ZSM-5, likely attributable to the low loading level of ZSM-5 and the overlap of peaks with the predominant crystalline phases of quartz and mullite in fly ash [32] . The lack of ZSM-5 diffraction peaks in the XRD indicates that the particles are either extensively dispersed within the support matrix or present in a partially amorphous state, notably reducing the diffraction intensity.

4.3.2 FESEM analysis

A uniform dispersion of TiO_2 nanoparticles across the surface of the spherical fly ash particles is revealed by the FE-SEM images of the synthesized composites, which are displayed in **Fig. 4.2 (a, b).** The FT composite predominantly consists of spherical particles characterized by smooth surfaces, affirming successful surface modification. At lower magnification, the boundaries may appear indistinct; however, TiO_2 nanoparticles are likely dispersed across the fly ash particles. The irregular surface roughness indicates a heterogeneous composition of the fly ash [26,33].

The FT-Cu_1 composite shown in **Fig. 4.2 (c, d)** exhibits enhanced surface uniformity in TiO_2-coated fly ash. Cu doping reduces agglomeration, potentially due to enhanced dispersion or interaction with TiO_2 particles, but it is not shown on the surface in FESEM images, due to a smaller nanometre size. This modification may enhance electron mobility or reduce the recombination rate in photocatalytic systems [26]. The FESEM structure of 3ZFT-Cu_1 and 5ZFT-Cu_1 composites is shown in **Fig. 4.3 (a, b)** and **Fig. 4.3 (c, d),** respectively. Both composites coarse and porous surface make them suitable for adsorption and photocatalytic degradation [34]. The presence of cluster particles in the 3ZFT-Cu_1 composites' coarse

structure suggests that the zeolite, fly ash, and TiO_2 were well incorporated.

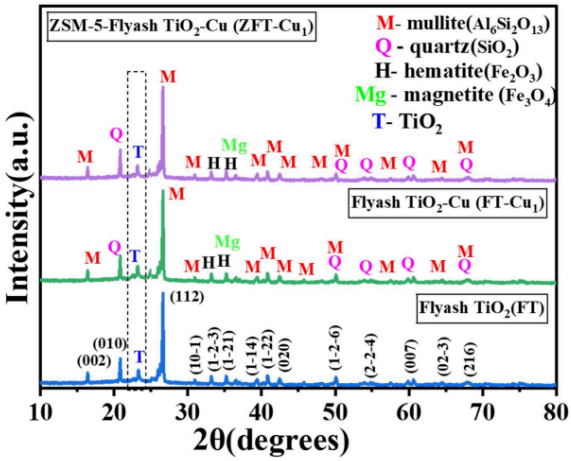

Fig. 4.1 XRD profiles of Fly ash-TiO_2 (FT), Copper loaded fly ash-TiO_2 composite (FT-Cu_1) and ZSM-5 loaded Fly ash- TiO_2- copper composite (ZFT-Cu_1)

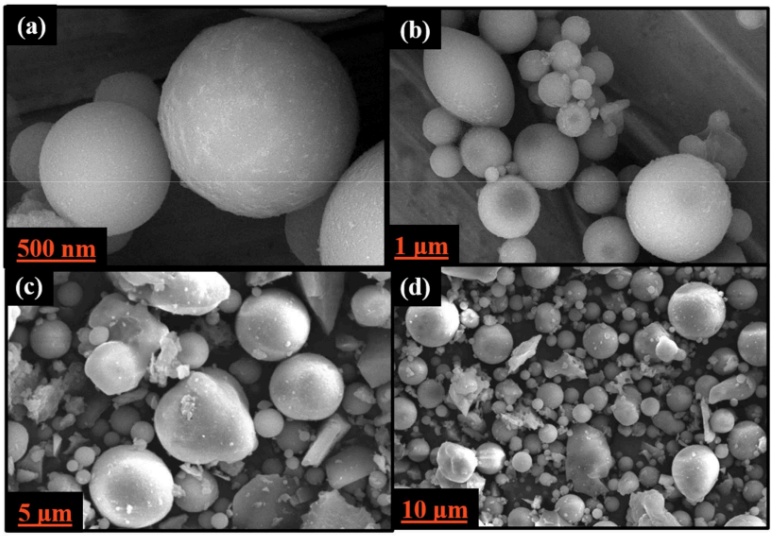

Fig. 4.2 FE-SEM micrographs of (a, b) FT, and (c, d) FT-Cu_I composite

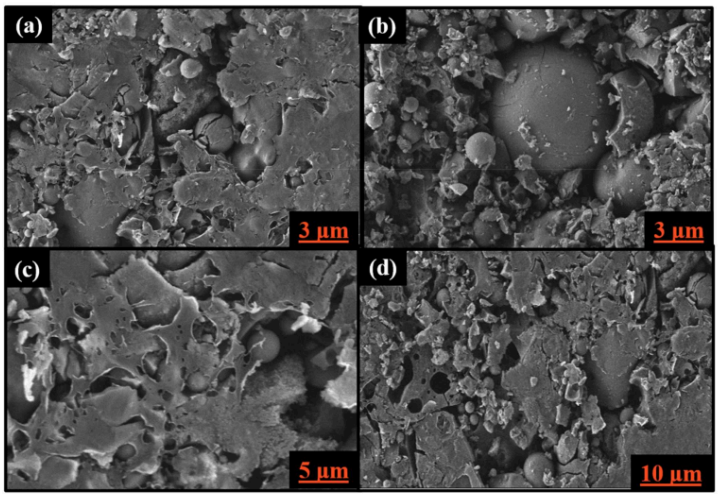

Fig. 4.3 FE-SEM micrographs of (a, b) 3ZFT-Cu_I and (c, d) 5ZFT-Cu_I composite.

4.3.3 EDS analysis

Energy dispersive spectroscopy (EDS) was used to analyse the elemental composition of 3ZFT-Cu_1 composite, which showed the distribution of the elemental composition, as well as their atomic and weight percentages. **Fig. 4.4** shows the elemental composition of the composite as confirmed by the EDS spectra, which show the presence of oxygen (O), silicon (34.07%), aluminium (12.88%), copper (1.05%), iron (1.1%), titanium (4.32%), and sodium (0.82%) in the composite.

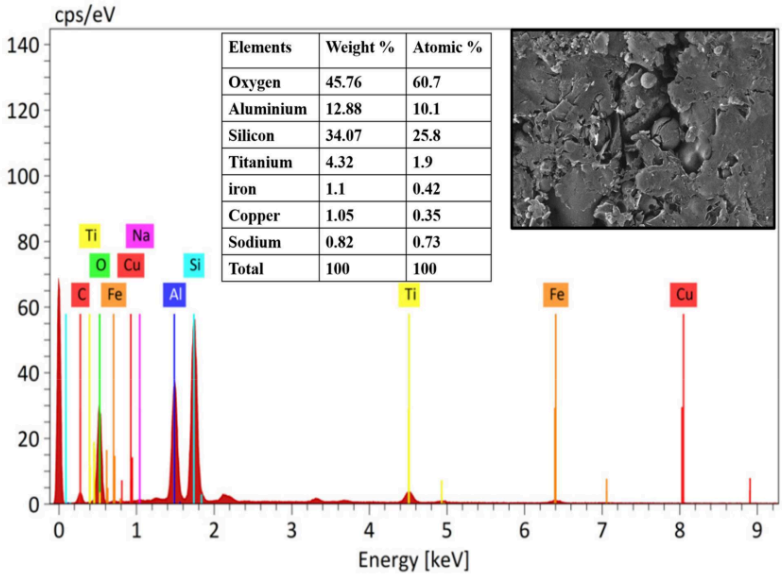

Fig. 4.4 EDS analysis of 3ZFT-Cu_1 composite confirming the presence of constituent elements.

4.3.4 FT-IR analysis

The FTIR spectra of ZSM-5, TiO_2, fly ash, and the Cu-modified composites (1ZFT-Cu_1, 3ZFT-Cu_1, and 5ZFT-Cu_1) are presented in **Fig. 4.5**. For ZSM-5, the typical framework vibrations are evident, with strong bands at 1080–1100 cm^{-1} corresponding to asymmetric T–O–T stretching (T = Si or Al), at 790–800 cm^{-1} for symmetric Si–O–Si stretching, and at 450–500 cm^{-1} attributed to Si–O–Si/Al–O–Si bending [35]. These characteristic peaks persist in the

ZFT-Cu composites, confirming that the zeolite lattice remains intact after compositing and Cu incorporation. TiO_2 displays a broad band below 800 cm^{-1} assigned to Ti–O–Ti vibrations, which is also distinguishable in the composites, signifying the presence of TiO_2 within the hybrid framework [36]. The FTIR profile of fly ash reveals broad Si–O–Si stretching absorptions between 1000–1080 cm^{-1} and a band near 1630–1640 cm^{-1} linked to bending of adsorbed water molecules [37]; both signals are retained in the ZFT-Cu materials. Incorporation of Cu into the composites leads to subtle shifts and variations in the intensities of the ZSM-5 framework peaks, suggesting interaction among ZSM-5, TiO_2, and fly ash components while preserving the fundamental crystalline structure. In addition, all spectra show a broad band around 3400–3450 cm^{-1}, assigned to O–H stretching of surface hydroxyl groups and physisorbed water, which appears more intense in the composites, indicating an increased number of active surface sites. Overall, the FTIR results demonstrate that ZSM-5, TiO_2, and fly ash were successfully integrated with Cu, maintaining the structural integrity of the zeolite and producing composites with potential for enhanced adsorption and photocatalytic performance.

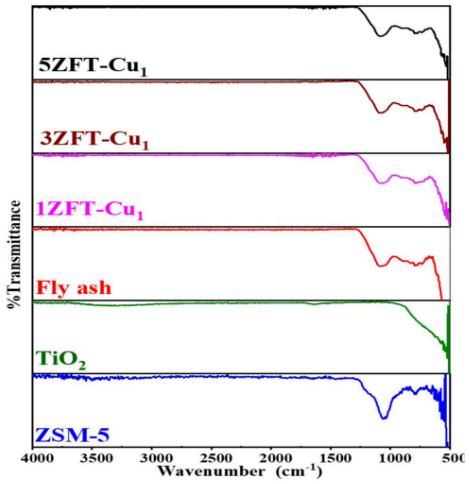

Fig. 4.5 FTIR spectra of TiO_2, fly ash, ZSM-5, and ZSM-5-loaded Fly ash-TiO_2-Cu composites (1ZFT-Cu_1, 3ZFT-Cu_1, 5ZFT-Cu_1)

4.3.5 BET Surface Area and Pore Size Distribution

Fig. 4.6 (a, b) displays the results of the N_2 adsorption-desorption experiments conducted on FT, FT-Cu_1, and 3ZFT-Cu_1 composites using BJH plots for the purpose of evaluating the surface area and pore distribution. Type IV isotherms confirm the existence of mesopores with multilayer adsorption and H_3 hysteresis loops, which are seen in all composites. As compared to FT and FT-Cu_1, 3ZFT-Cu_1 achieves the highest nitrogen adsorption quantity. After ZSM-5 modification, FT-Cu_1 exhibits a greater surface area. The study of the BJH pore distribution, derived from the desorption branch of the nitrogen adsorption–desorption isotherms indicated a more homogeneous mesoporous structure, with a sharp and narrow peak between 4 and 6 nm and a total pore diameter range of 2 to 10 nm. The enhanced adsorption of dye molecules and the greater mass movement during photocatalytic degradation are two potential advantages of the larger pores and more surface features. Our results show that adding ZSM-5 to FT-Cu_1 composites improves their photocatalytic effectiveness when exposed to visible and solar light [38] **Table 4.1** shows the specific surface area, pore diameter, and pore volume data for each sample.

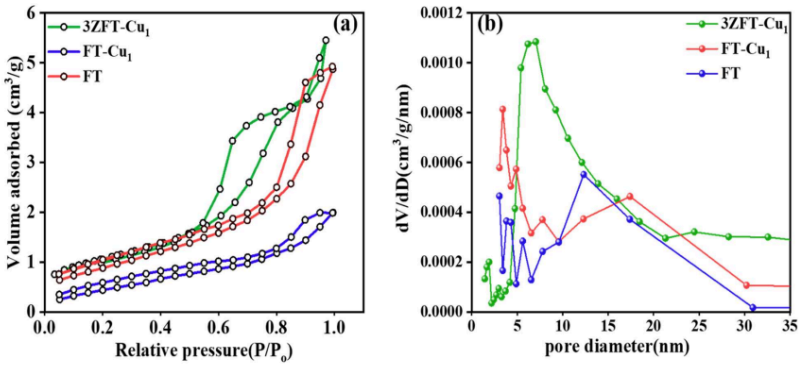

Fig. 4.6. (a) Nitrogen sorption isotherms and (b) Barrett–Joyner–Halenda (BJH) plot of various (FT, FT-Cu_1 and 3ZFT-Cu_1) composites.

Table 4.1. Pore volume, surface area and pore diameter of TiO_2, fly ash, FT, and FT.Cu_1, 3ZFT-Cu_1 and ZSM-5 composites.

Photocatalyst	BET surface area (m^2/g)	Pore volume (cm^3/g)	Pore diameter (nm)
TiO_2	99.703	0.195	12.309
Fly ash	1.347	0.003	3.054
FT	3.268	0.007	3.411
FT-Cu_1	6.725	0.010	8.712
3ZFT-Cu_1	10.562	0.012	11.552
ZSM-5	24.6	0.169	23.74

4.3.6 DRS analysis

Diffuse reflectance spectra (DRS) obtained via UV-vis spectroscopy of TiO_2, FT, FT-Cu_1, and 3ZFT-Cu_1 composites are presented in **Fig. 4.7**. The corresponding Tauc plots of TiO_2, FT, and FT-Cu_1 are shown in **Fig. 4.8(a).** At the same time, **Fig. 4.8(b)** illustrates the Tauc plots of composites containing different ZSM-5 loadings (1–5wt%). Unique absorption peaks can be observed below 400 nm in the DRS spectra. The observed peaks signify the transitions of electrons from O^{2-} (2p) orbitals in the valence band to Ti^{3+}(3d) orbitals in the conduction band. Enhanced UV absorption and a red shift in the FT composite are likely due to formation of Si–O–Ti bonds between TiO_2 and the fly ash surface [39]. The photocatalytic effectiveness of the Cu-loaded TiO_2-fly ash composite is enhanced because the addition of Cu induces localized energy levels and heterojunctions, which in turn decrease the bandgap and move the absorption edge to the visible area [26]. The 3ZFT-Cu_1 composite, although showing improved light absorption compared to the bare FT composite, exhibits a relatively smaller red shift than the Cu-loaded FT composites as determined from the Tauc plot analysis. The data suggest that although the integration of ZSM-5 improves light absorption and promotes charge separation due to its elevated porosity and surface acidity, its effect on bandgap reduction is rather minimal. Thus, the modulation of the bandgap is mostly dictated by copper modification, whereas ZSM-5 has little effect on the electronic transition characteristics [40]. The bandgap energies of the synthesized composites were evaluated using Tauc's method, defined by the

following equation (4):

$$\alpha h\nu = A(h\nu - E_g)^n \quad (12)$$

In the Tauc equation, α signifies the optical absorption coefficient, hν refers to the photon energy, A is a proportionality constant, and Eg signifies the optical bandgap energy. The exponent n characterizes the electronic transition, where n = 0.5 corresponds to a direct allowed transition and n = 2 to an indirect allowed transition. Eg values were estimated by projecting the linear section of the $(\alpha h\nu)^2$ versus hν curve onto the photon energy axis, with the intercept on the x-axis indicating the bandgap. The estimated bandgap (E_g) values were estimated to be 2.3 eV for 3ZFT-Cu_1, 2.2 eV for FT-Cu_1, 3.12 eV for pristine TiO_2, 2.55 eV for the FT composite, 2.36 eV for 5ZFT-Cu_1, and 2.48 eV for 1ZFT-Cu_1 as shown in **Fig. 4.8 (a, b)**

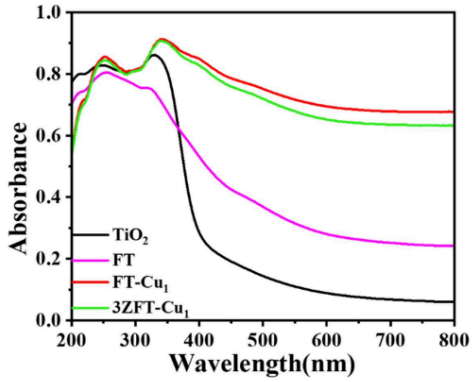

Fig. 4.7 UV-Vis diffuse reflectance spectra of TiO_2, FT, FT-Cu_1 and 3ZFT-Cu_1 samples

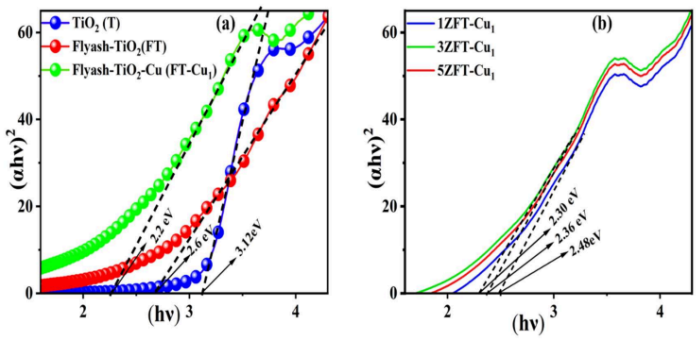

Fig. 4.8 (a) Optical bandgap estimation using Tauc plots for TiO_2, FT and FT-Cu_1 (b) for 1ZFT-Cu_1, 3ZFT-Cu_1 and 5ZFT-Cu_1 composites.

4.4 Adsorption study

4.4.1 Influence of adsorbent dosage on CV dye removal

Fig. 4.9(a) demonstrates the impact of adsorbent dosage on the removal of CV dyes. It is seen that the % removal of CV dye increases with the increase of adsorbent dose of all the composites, including FT, FT-Cu_1, and ZSM-5 integrated composites (1ZFT-Cu_1, 3ZFT-Cu_1, and 5ZFT-Cu_1). This is due to the increased availability of surface-active sites, allowing the dye molecules to interact more efficiently with the adsorbent surface. Among the composites, the 3ZFT-Cu_1 composite exhibited the highest removal efficiency of 71% followed by 5ZFT-Cu_1 (66%), 1ZFT-Cu_1 (61%), FT-Cu_1 (55%), and FT (49%) at 5 mg dose. Composites loaded with ZSM-5 have superior performance compared to those without because of the synergistic interaction between copper and zeolite, which enables efficient dye absorption through the mesoporous nature of zeolite and its enhanced surface area. However, the % removal of CV for all samples decreased when the dose was increased from 5 mg to 10 mg. This is likely because of agglomeration at higher dosages and potential interaction among active sites. The results indicate that 5 mg is the optimal dose for removing CV dye.

4.4.2 Role of initial dye concentration on the removal of CV dye

The impact of initial pollutant concentration on crystal violet dye removal was investigated

using several modified composites, including FT, FT-Cu_I, 1ZFT-Cu_I, 3ZFT-Cu_I, and 5ZFT-Cu_I. **Fig. 4.9(b)** shows that with the increase in dye concentration from 3mg/L to 15 mg/L, a gradual decline in % removal of CV dye was observed. 3ZFT-Cu_I exhibited the highest removal of 71% CV dye at 5mg/L concentration, indicating enhanced active sites availability and synergistic effects due to optimal ZSM-5 loading. In contrast, the FT composite demonstrated the lowest removal efficiency of 49%, highlighting the role of surface modification in improving adsorption performance. As dye concentration rises, the reduction in efficiency may result from the saturation of active adsorption sites, leading to insufficient surface area to accommodate the additional dye molecules.

4.4.3 Impact of contact duration on the removal of CV dye

The effect of contact duration on the removal of CV dye over all the composites is shown in **Fig. 4.9(c).** The % removal of CV dye was shown to increase with increasing contact duration, with all adsorbents reaching a peak at 180 minutes. The enhanced performance is due to the rapid initial uptake of dye molecules onto available active sites of the adsorbents. The combined benefits of porous ZSM-5 and copper-mediated composite (3ZFT-Cu_I) enabled the most effective and quick dye adsorption at 180 minutes, removing 71% of the CV dye. Beyond 180 minutes, the removal efficiency plateaued or slightly declined, indicating that equilibrium had been attained and active sites were saturated.

4.4.4 The effect of solution pH on CV dye removal

The overall adsorption efficiency is affected by solution pH, which is a major factor determining the adsorbent surface charge and ionization behaviour of the dye. The adsorption occurred at ambient temperature using 5 mg of the 3ZFT-Cu_I composite, with a dye concentration of 5 ppm and a contact time of 180 minutes. The pH of the solution was altered from 2 to 12 using 0.1 M HCl and 0.1 M NaOH. **Fig. 4.9(d)** illustrates the influence of pH on the elimination of crystal violet (CV) dye throughout a pH range from 2 to 12. The result shows that with a raise in solution pH, CV removal increases up to pH 9, followed by a decline at higher pH levels. Among all the composites, 3ZFT-Cu_I showed the highest removal efficiency, reaching over 70% at pH 9, indicating a synergistic effect of ZSM-5 and copper incorporation. The removal order at the optimum pH was 3ZFT-Cu_I > 5ZFT-Cu_I > 1ZFT-Cu_I > FT-Cu_I > FT. The superior performance of ZFT-Cu_I composites is ascribed to the increased surface area, active sites, and charge interactions with dye molecules. The point of zero charge

(pH_{pzc}) of the 3ZFT-Cu_1 composite was quantified to be around 7.4. When exposed to acidic circumstances (pH < 7.4), the surface of the composite undergoes protonation, becoming positively charged. The positive charge of the cationic CV dye molecules induces electrostatic repulsion with the adsorbent surface, hence reducing the quantity of dye that may be adsorbed. Conversely, at alkaline pH values (pH > 7.4), the surface of the 3ZFT-Cu_1 composite acquires a negative charge as a result of deprotonation. Although CV dye remains cationic across a broad pH range, the electrostatic attraction between the negatively charged adsorbent and the positively charged dye molecules becomes more favourable, enhancing adsorption.

The enhanced electrostatic interaction between the negatively charged 3ZFT-Cu_1 surface and the cationic CV dye accounts for the optimal dye removal at pH 9. Additionally, hydrogen bonding and $\pi-\pi$ interactions between CV aromatic rings and the adsorbent surface might boost adsorption effectiveness at this pH level. Adsorption of CV dye decreases at pH levels over 9, probably due to greater competition with OH^- ions and partial neutralization of dye molecules, lowering electrostatic attraction.

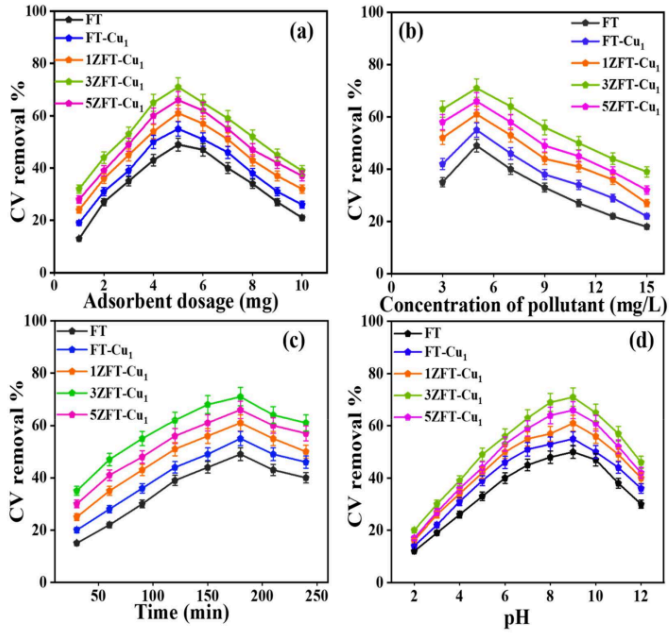

Fig. 4.9 Plots illustrating the impact of (a) adsorbent dose, (0.005 g/L) (b) adsorbate concentration, (5mg/L) (c) the contact time, (time 180 min) and (d) Effect of solution pH on removal of CV dye by FT, FT-Cu_1, 1ZFT-Cu_1, 3ZFT-Cu_1 and 5ZFT-Cu_1composites.

4.4.5 Adsorption isotherm studies

The adsorption of crystal violet (CV) onto FT-Cu_1 and ZFT-Cu_1 composites was analyzed using Langmuir, Freundlich, Temkin, and Dubinin–Radushkevich (D–R) isotherms. The initial fitting of the data was conducted utilizing the Langmuir isotherm model, as outlined in equation (4). This model suggests that adsorption takes place via the establishment of a monolayer over ZSM-Cu-flysh-TiO_2 composite, wherein each molecule occupies a unique adsorption site on the surface. The graph of $1/Q_e$ vs. $1/C_e$ is shown in **Fig. 4.10(a)**. The intercept and slope of this curve determine K_L and Q_{max}.

Adsorption on heterogeneous surfaces is described by the Freundlich isotherm shown in

equation (5), where the adsorption energy varies across locations. It takes surface heterogeneity into account, which in turn considers multilayer adsorption and interactions between adsorbed molecules. Here, 1/n is the heterogeneity factor, which is related to adsorption intensity, and K_F is the Freundlich constant, which stands for adsorption capacity [41]. The plot of log Q_e vs log C_e may be seen in **Fig. 4.10(b).** The results indicate that for the 3ZFT-Cu_I composite, Freundlich isotherm best described the adsorption process, with a correlation coefficient R^2= 0.997, compared to R^2 = 0.982 for the Langmuir model. This suggests that the adsorption occurs predominantly on heterogeneous surfaces rather than through ideal monolayer formation.

According to the Temkin isotherm presented in equation (6), it is suggested that the heat of adsorption diminishes as the number of interactions between the adsorbate and adsorbent increases **(Fig. 4.10(c)).** The heat of adsorption, represented by BT, is calculated using the equation BT = RT / β, where β signifies the maximum binding energy. The value of β was found to be 8.55 kJ/mol suggesting a physisorption process [42]

The Dubinin–Radushkevich (D–R) isotherm model in equation (7), illustrated in **Fig. 4.10(d),** serves as a prevalent tool for differentiating between the mechanisms of physical and chemical adsorption. The adsorption of crystal violet onto ZFT-Cu_I composites yielded low values for the constant β (mol^{-2} kJ^2), resulting in mean free energy values ranging from 0.705 to 1.120 kJ mol^{-1} [43]. The evidence indicates that the adsorption process is primarily governed by physisorption. The specifications for the models, as mentioned above, are presented in **Table 4.2**. Although nonlinear fitting is generally recommended for adsorption and kinetic modelling, linear models were employed in this study for consistency and comparability with previous literature. Overall, the analysis demonstrates that ZSM-5 loading improves adsorption efficiency by offering more active sites and promoting interactions between the dye molecules and the composite surface.

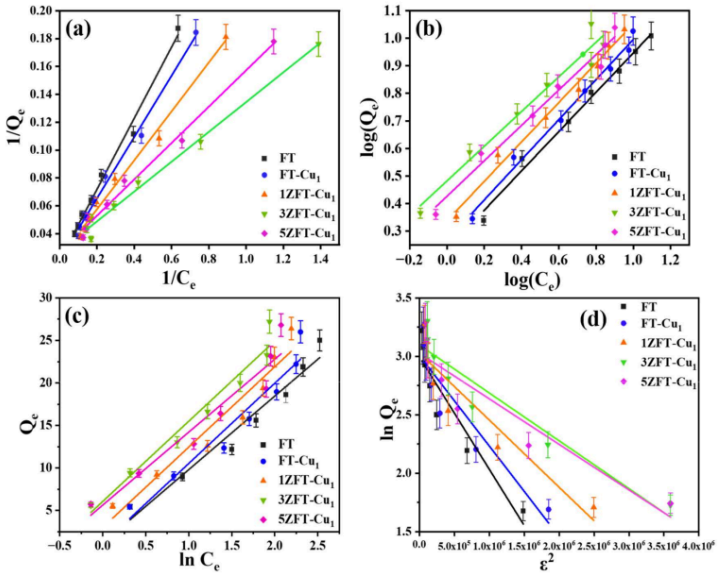

Fig. 4.10 Linear fitting of adsorption isotherm plots for CV dye adsorption over FT, FT-Cu_1, 1ZFT-Cu_1, 3ZFT-Cu_1, and 5ZFT-Cu_1 composites using (a) Langmuir adsorption isotherm, (b) Freundlich adsorption isotherm, (c) Temkin adsorption isotherm, and (d) Dubinin-Radushkevich adsorption isotherm model.

Table 4.2. Isotherm parameter of Langmuir, Freundlich, Temkin and D-R models for adsorption of crystal violet dye by FT and different wt.% ZFT-Cu_1 composites.

	Langmuir isotherm			**Freundlich isotherm**		
Adsorbent	**Q_{max}(mg/g)**	**K_L**	**R^2**	**K_F**	**1/n**	**R^2**
FT	34.48	0.0032	0.995	1.774	1.436	0.9934
FT-Cu_1	35.71	0.0041	0.9931	1.890	1.393	0.99
1ZFT-Cu_1	42.19	0.0056	0.9895	2.329	1.478	0.9916
3ZFT-Cu_1	50	0.0199	0.9829	3.064	1.587	0.997
5ZFT-Cu_1	43.29	0.0048	0.9884	2.802	1.628	0.9826

	Temkin isotherm			D-R isotherm		
Adsorbent	**B (KJ mol^{-1})**	**A (Lmg^{-1})**	**R^2**	**$\beta \times 10^{-8}$ (mol^{-2} kJ^2)**	**E**	**R^2**
FT	0.0109	0.7144	0.958	0.01	0.705	0.8889
FT-Cu_I	0.0093	1.1594	0.934	0.008	0.791	0.8699
1ZFT-Cu_I	0.0089	1.5611	0.9215	0.006	0.913	0.8711
3ZFT-Cu_I	0.0086	2.3622	0.9437	0.004	1.120	0.9151
5ZFT-Cu_I	0.0082	2.1375	0.917	0.004	1.120	0.8648

4.4.6 Adsorption Kinetics study

The experimental kinetic data **(Fig. 4.11)** were analysed using several models, including pseudo-first-order, pseudo-second-order, Elovich and intraparticle diffusion. As shown in **Fig. 4.11(a)**, the pseudo-first-order model (Eq. 9; log(Qe–Qt) vs. t) gave an excellent fit for the adsorption of CV dye on 3ZFT-Cu_I, with an R^2 value of 0.9945 and a rate constant of 0.0225 min^{-1}. In comparison, the pseudo-second-order model (Eq. 10; **Fig. 4.11(b))** yielded an R^2 of 0.9725 and a rate constant of 0.0004 min^{-1}. These results indicate that the adsorption of CV dye onto FT-Cu_I and ZFT-Cu_I composites follows predominantly pseudo-first-order kinetics, suggesting that physisorption is the main adsorption mechanism under the studied conditions. The calculated equilibrium capacities (Q_e), rate constants (k_1 and k_2) and R^2 values for all samples are already summarized in Table 2, which clearly shows the superiority of the pseudo-first-order model over the pseudo-second-order model for these systems.

As shown in **Fig. 4.11(c)** of the Elovich model in equation (11), the adsorbate appears to be removed from solution using chemisorption onto a surface that contains energetically different active sites [44]. The β values ranged from 0.217to 0.240 g mg^{-1}, which are relatively low and suggest that the adsorption process is governed primarily by physisorption rather than chemisorption. Furthermore, although the Elovich model provided a reasonably good fit (R^2 = 0.8868–0.9844), the pseudo-first-order model exhibited higher correlation coefficients (R^2 = 0.8968-0.9962), indicating it more accurately described the adsorption kinetics and thus following the physisorption process.

Fig. 4.11(d) displays the intra-particle diffusion model equation (12) plots for all the composites, including FT, FT-Cu_I, and ZFT-Cu_I (1ZFT, 3ZFT, and 5ZFT). The fact that Q_t and $t_{1/2}$ are linear in all samples suggests that intraparticle diffusion plays a substantial role in adsorption [44]. Intraparticle diffusion is not the only step that determines the rate because the

plots do not go through the origin. The 3ZFT-Cu_1 composite showed the steepest slope and highest intercepts in the figure, meaning that the surface improvements allowed for an increase in intraparticle diffusion capacity; **Table 4.3** shows the values correlating to the various kinetic models. In this study, linear models were used to maintain consistency with prior literature, despite the general recommendation of nonlinear fitting for adsorption and kinetic modelling. These results collectively highlight that the synergistic incorporation of ZSM-5 and copper enhances both adsorption capacity and adsorption kinetics of the fly ash–TiO_2 composites.

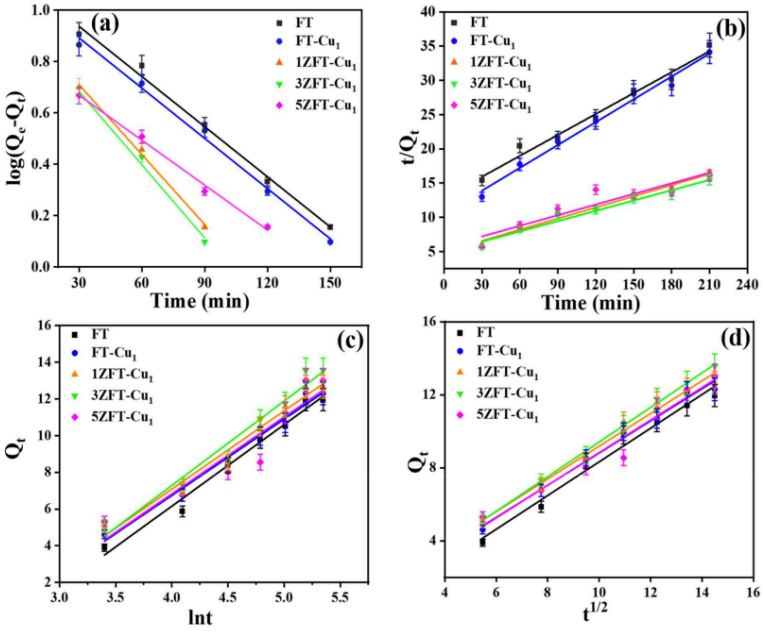

Fig. 4.11 Linear fitted plots of kinetic models for CV dye adsorption over FT, FT-Cu_1, 1ZFT-Cu_1, 3ZFT-Cu_1, and 5ZFT-Cu_1 composites using (a) Pseudo-first-order kinetic model,(b) Pseudo-second-order kinetic model, (c) Elovich kinetic model and, (d) Intra-particle diffusion kinetic model.

Table 4.3 Kinetic parameter of Pseudo-first-order, Pseudo-second-order, Elovich and Intra-particle models for adsorption of crystal violet dye by FT and different wt.% ZFT-Cu_I composites.

	Pseudo-first-order			Pseudo-second-order		
Adsorbent	**Q_e (mg/g)**	**k_1 (min^{-1})**	**R^2**	**Q_e (mg/g)**	**k_2 (min^{-1})**	**R^2**
FT	13.542	0.0149	0.9917	9.813	0.0008	0.9805
FT-Cu_I	17.621	0.0154	0.9941	8.993	0.0017	0.988
1ZFT-Cu_I	19.567	0.0209	0.9962	18.42	0.0005	0.9846
3ZFT-Cu_I	27.003	0.0225	0.9945	20.24	0.0004	0.9725
5ZFT-Cu_I	20.678	0.0213	0.8968	19.30	0.0004	0.8763

	Elovich model			Intra-particle diffusion model		
Adsorbent	**α (mg g^{-1} min^{-1})**	**β (g mg^{-1})**	**R^2**	**K_{ip}**	**C (mg g^{-1})**	**R^2**
FT	0.3252	0.2251	0.9826	0.9227	-0.9018	0.979
FT-Cu_I	0.3850	0.2404	0.9844	0.8824	-0.0172	0.9895
1ZFT-Cu_I	0.4117	0.2347	0.9791	0.8963	0.2202	0.9852
3ZFT-Cu_I	0.3128	0.2347	0.9684	0.9481	0.0712	0.9981
5ZFT-Cu_I	0.3907	0.2385	0.8868	0.8923	0.0956	0.9594

4.5 Photocatalytic studies

4.5.1 Photocatalytic efficacy under visible light irradiation

Photocatalytic degradation of crystal violet (CV) dye under visible light using a Wipro Garnet B22 50-Watt LED bulb equipped with a cut-off filter (wavelength > 360 nm) by ZFT-Cu_I composites containing ZSM at various weight percentages (1, 3, and 5wt%) is illustrated in **Fig. 4.12.** **Fig. 4.12(a)** displays the UV-vis absorption spectra of CV dye (5 ppm) with the 3ZFT-Cu_I composite at different irradiation periods (60-240 minutes), showing a maximum absorption peak at 589 nm. The visual evidence shows that 98% of the CV dye has been removed, and the decomposition of the dye has been noticeable, with a noticeable shift from a violet to a colourless dye solution, and a significant decrease in the distinctive absorption peak at 589 nm. In **Fig. 4.12(b)**, after being exposed for 180 minutes under visible light. ZSM-5-fly ash-TiO_2-Cu composites (1ZFT-Cu_I, 3ZFT-Cu_I, and 5ZFT-Cu_I) are compared to FT and FT-Cu_I in terms of their photocatalytic activity. The 3ZFT-Cu_I composite has the best degradation

efficiency, with the largest drop in absorbance, compared to the other materials.

Fig. 4.12(c) displays concentration profiles (C/C_0) that change over time; this data sheds information on the degradation kinetics in both dark and visible light. Under illumination, the 3ZFT-Cu_1 catalyst demonstrates a steep drop in CV concentration. **Fig. 4.12(d)** shows the results of the kinetic analysis, which provide a pseudo-first-order model in equation (13) for the degradation process. This model is mainly controlled by the concentration of CV dye and is defined by the following equation:

$$\ln (C_o/C_t) = kt. \quad (13)$$

C_0 is the CV dye concentration at 0 minutes, C_t is the concentration at time t, and k is the rate constant. This indicates the breakdown rate remains unchanged regardless of variations in the content of water or oxygen [45]. When the light intensity and amount of photocatalyst are held constant, the rate changes are considered insignificant. According to the rate constant obtained from the linear plots, 3ZFT-Cu_1 has the highest rate constant ($k = 0.0054\ min^{-1}$), which is greater than FT composite ($k = 0.0013\ min^{-1}$) shown in **Table 4.4.** suggesting that the combination of Cu doping, ZSM-5, and fly ash has a synergistic effect that improves charge separation and light absorption.

Table 4.4. Kinetic parameter of pseudo first order model of different wt.% ZFT-Cu_1 composites under visible and under sunlight.

	Pseudo-first-order (visible light)		Pseudo-first-order(sunlight)	
Photocatalyst	**k_1**	**R^2**	**k_1**	**R^2**
FT	0.0013	0.9927	0.0012	0.9943
FT-Cu_1	0.0015	0.9948	0.0014	0.9915
1ZFT-Cu_1	0.0019	0.9907	0.0019	0.9926
3ZFT-Cu_1	0.0054	0.995	0.0044	0.998
5ZFT-Cu_1	0.0024	0.9938	0.0023	0.9952

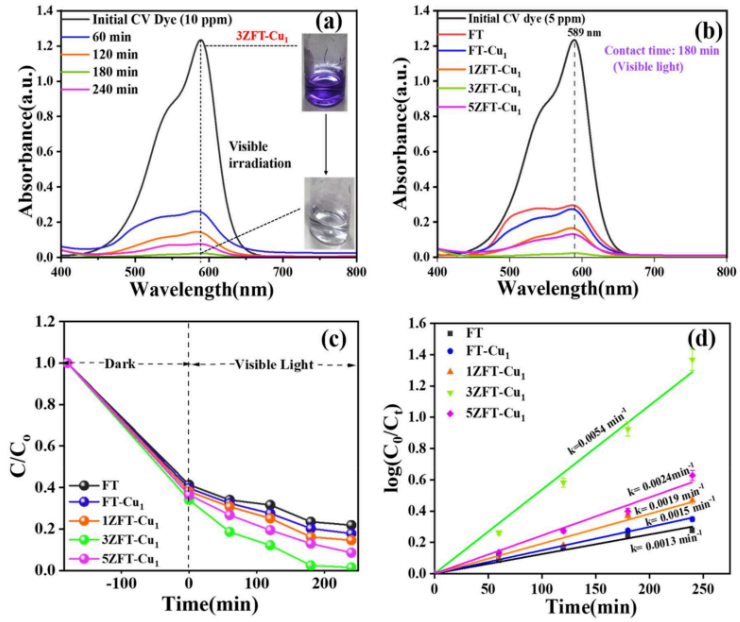

Fig. 4.12 (a) Absorption spectra and visual colour changes of CV dye during photocatalytic degradation under visible light by 3ZFT-Cu_1 composite over different time periods (b) Absorption spectra of CV dye after 180 min of visible light by different wt% ZFT-Cu_1 composites, (c) time dependent kinetic plots (d) Pseudo first-order kinetic fitting illustrating the degradation efficiency by various composites under visible light irradiation.

4.5.2 Photocatalytic degradation under direct sunlight

The photocatalytic performance of ZFT-Cu_1 composites was thoroughly investigated under natural sunlight for the degradation of crystal violet (CV) dye. The experiments were conducted on 20 May 2025 in (Patiala, Punjab) wherein 5 mg of each composite was dispersed in 10 mL of 5 ppm CV dye solution and exposed to sunlight for 180 minutes under constant magnetic stirring. The solar light intensity during the process averaged 620 W/m², and the ambient temperature remained between 34 and 38°C.

As depicted in **Fig. 4.13(a),** the time-dependent absorption spectra and corresponding visual

colour changes of the dye solution indicate the gradual photodegradation of CV dye by the 3ZFT-Cu_1 composite. The intense violet colour of the dye faded significantly with increasing irradiation time, eventually turning nearly colourless after 180 minutes, suggesting substantial breakdown of the dye molecules. **Fig. 4.13(b)** compares the photocatalytic performance of ZFT-Cu_1 composites with different ZSM-5 loadings. The composite with 3wt% ZSM-5 loading (3ZFT-Cu_1) demonstrated the highest photocatalytic efficiency, achieving around 95% degradation of CV dye when subjected to solar irradiation. The improvement is due to the combined effects of Cu doping and ZSM-5 incorporation, which enhance surface area, dye adsorption, and charge carrier mobility.

The degradation kinetics are further elaborated in **Fig. 4.13(c),** which shows the time course plots of dye concentration over 180 minutes. The 3ZFT-Cu_1 composite demonstrated the steepest decline, indicating the most rapid degradation rate among all tested samples. The kinetic behaviour of the composites follows a pseudo-first-order model, as shown in **Fig. 4.13(d)**. The calculated rate constant for 3ZFT-Cu_1 was found to be 0.0044 min^{-1}, notably higher than other composites, underscoring its excellence photocatalytic performance under solar light. The pseudo-first-order kinetic constants, along with the corresponding R^2 values for FT and ZFT-Cu_1 composites under visible and solar light irradiation, are presented in Table 3. These findings support that the 3ZFT-Cu_1 composite is a highly efficient photocatalyst for the solar-assisted degradation of crystal violet dye and holds strong potential for application in sustainable wastewater treatment technologies**.**

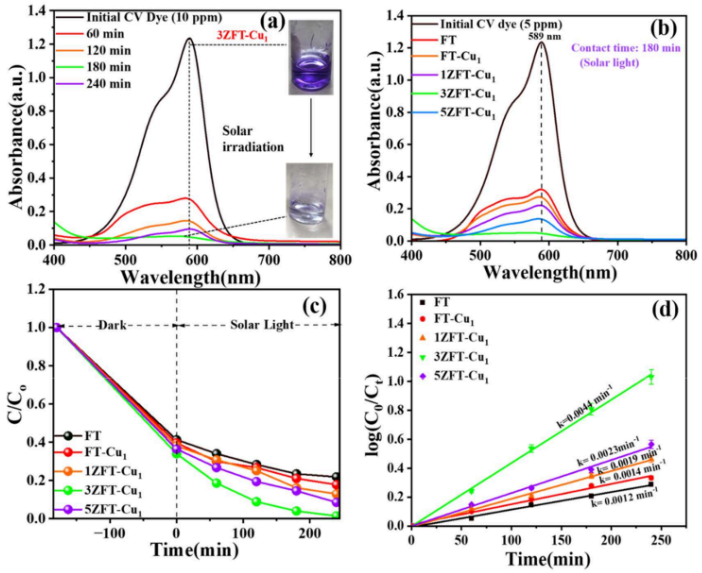

Fig. 4.13 (a) Absorption spectra and visual colour changes of CV dye during photocatalytic degradation under solar light by 3ZFT-Cu_1 composite over different time periods and (b) Absorption spectra of CV dye after 180 min of solar light by different wt% ZFT-Cu_1 composites, (c) time dependent kinetic plots (d) Pseudo first-order kinetic fitting illustrating the degradation efficiency by various composites under solar light irradiation.

4.6 Detection of active species

The experiment aimed to determine the main reactive species involved in the degradation process. **Fig. 4.14(a)** shows the function of different scavengers in the photocatalytic degradation of crystal violet (CV) dye using the 3ZFT-Cu_1 composite. The degradation efficiency reached a peak of 98% without any scavenger, demonstrating the exceptional photocatalytic activity of the composites used. The introduction of EDTA, recognized as a hole (h^+) scavenger, reduced degradation efficiency to 19%, indicating that photogenerated holes

are vital to the degradation mechanism. Similarly, the introduction of argon (Ar), which removes dissolved oxygen and consequently suppresses the formation of superoxide radicals (O_2-) [46] , resulted in a 20% degradation rate, indicating the involvement of superoxide radicals.

The presence of ammonium thiocyanate (NH_4SCN), an electron scavenger, resulted in a degradation efficiency of 15%, underscoring the role of electrons in the redox reactions. Adding ethanol and isopropanol, functioning as hydroxyl radical (.OH) scavengers, resulted in 22% and 21% degradation efficiencies, respectively. This signifies that hydroxyl radicals significantly contribute to the breakdown process. The significant decrease in photocatalytic performance with the introduction of each scavenger indicates that various reactive species, such as holes, electrons, superoxide radicals, and hydroxyl radicals, play a role in the degradation mechanism of CV dye removal by the 3ZFT-Cu_1 composites under visible light.

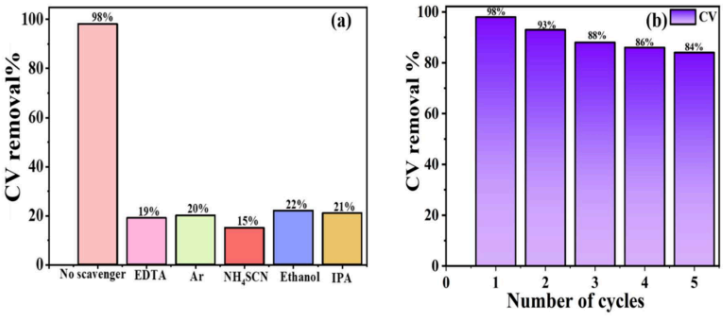

Fig. 4.14. (a) Effect of different hole scavengers on the photocatalytic degradation efficiency of FB dye using the 3ZFT-Cu_1 composite, (b) Reusability performance of the 3ZFT-Cu_1 composite over multiple photocatalytic cycles under visible light irradiation.

4.7 Proposed photocatalytic degradation mechanism

As shown in **Scheme 4.1**, the photocatalytic degradation of crystal violet (CV) dye using a ZSM-5-loaded-flyash-TiO_2-Cu (ZFT-Cu_1) composite occurs through a combined process of adsorption, charge separation, and reactive species production when exposed to visible or solar light. The extensive surface area and porous structure of ZSM-5 facilitate the adsorption of CV molecules onto the catalytic surface, increasing the dye concentration at the active sites. In

addition, the interconnected micropores of ZSM-5 also provide pathways for charge migration, enhancing charge separation efficiency. Exposure to visible light induces Cu doping, hence decreasing the band gap of TiO_2 and enhancing its photon absorption within the visible spectrum. Photoexcitation causes the formation of electron-hole pairs (e^-/h^+). Electrons are transported from the conduction band of TiO_2 to Cu^{2+}, which is then reduced to Cu^+, suppressing charge recombination and promoting interfacial charge separation. In this context, the Cu sites act as effective electron traps that further suppress electron–hole recombination, thereby prolonging the lifetime of photogenerated charge carriers and facilitating subsequent redox reactions. Electrons reduce dissolved oxygen (O_2) to form superoxide radicals (O^{2-}), whereas photogenerated holes in the valence band oxidize surface-adsorbed water or hydroxyl ions to produce hydroxyl radicals ($\cdot OH$) [47] . Both radicals exhibit high reactivity and facilitate the progressive oxidative degradation of the CV dye into simpler intermediates, which ultimately decompose into CO_2, H_2O, and inorganic ions. Furthermore, the fly ash matrix adds stability and offers additional adsorption sites. This cooperative behaviour of ZSM-5, Cu, and TiO_2 is consistent with recent studies on the optimization of Cu-doped photocatalysts by surface modification [18] and with catalytic shunt mechanisms proposed for multi-component catalysts [48] , which together support the enhanced charge separation and reactive species formation observed in this work. So, improved CV dye degradation efficiency under visible light irradiation is guaranteed by the combined impacts of ZSM-5 textural features, Cu electron trapping function, and TiO_2 photocatalytic activity.

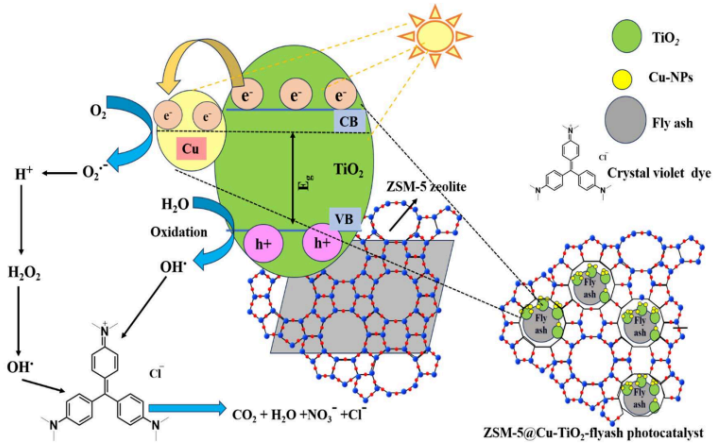

Scheme 4.1. The proposed photodegradation mechanism of CV dye by ZFT-Cu composite

under solar/visible light irradiation.

4.8 Reusability and photostability of the prepared photocatalyst

The 3ZFT-Cu_1 composite was tested for its photostability and reusability by exposing it to visible light for five cycles of crystal violet (CV) dye photocatalytic degradation. For each reusability test, 5 mg of the composite was dispersed in 10 mL of 5 ppm CV dye solution and irradiated with a visible light source (300 W Xe lamp, $\lambda > 420$ nm) for 180 minutes under constant magnetic stirring to maintain uniform suspension and efficient photon–catalyst interaction. After every cycle, the used catalyst was separated by centrifugation, regenerated using water and ethanol as desorbing agents to remove the adsorbed dye molecules, and dried at 80 °C for 6 h before reuse. The catalyst weight was measured after each run and showed only negligible loss (<3%) across the five cycles, confirming good structural stability.

As shown in **Fig. 4.14(b),** after reaching 95% in the first cycle, the CV removal effectiveness dropped to 84% in the fifth cycle. The 3ZFT-Cu_1 composite has remarkable photocatalytic stability and structural longevity, as seen by this little performance drop. The slight decrease is because the catalyst is lost somewhat during the washing and recovery processes between cycles, with minor surface fouling and possible blockage of active sites also contributing. But this didn't diminish the remarkable degrading efficiency of the composite, which bodes well for its future reusability in real-world wastewater treatment applications. These results validate that the catalyst maintains its structural integrity and functionality even after several reuses, demonstrating excellent stability, recyclability, and sustained photocatalytic activity under repeated operating conditions.

4.9 Comparative discussion with reported photocatalysts

The ZSM-5/Fly ash-TiO_2/Cu composite exhibits comparable or superior photocatalytic performance toward organic pollutants compared to the catalysts reported in **Table 4.5** [22,49–54], owing to the synergistic effect of Cu, porous ZSM-5, and fly ash support, which enhances adsorption and light absorption.

In addition to its superior activity toward dye degradation, the ZSM-5/Fly ash–TiO_2/Cu composite also shows strong potential for scale-up and broader environmental application. Its preparation by wet impregnation and calcination, combined with the use of low-cost fly ash as a support, makes the material cost-effective and compatible with large-scale or pilot-scale implementation. Moreover, the composite's high surface area, porous structure and visible-

light activity indicate that it can be extended beyond dyes to the removal of other classes of organic pollutants such as antibiotics [55] , phenolic compounds [56]and pesticides [57]. These attributes highlight its promise as a sustainable and economically viable photocatalyst for diverse wastewater treatment scenarios.

The use of fly ash-composite photocatalysts provides major environmental advantages by converting plentiful industrial waste into a valuable resource for pollution removal. However, integrating metals into the composite could potentially causes leaching, ICP–OES analysis showed minimal release of Fe and Al after five photocatalytic cycles, with Fe decreasing from 1.20 ppm to 0.45 ppm and Al from 1.56 ppm to 0.65 ppm, indicating the material's stability. The catalyst not only removes pollutants but also degrades them, reducing the overall toxicity of the treated water. The low metal leaching is supported by the minor decline in removal efficiency during reusability tests, indicating that the composites remain stable and can be reused effectively.

Table 4.5 Comparative photocatalytic performance of different reported catalysts for the degradation of various pollutants.

Photocatalyst	Pollutant	Light Source	Key Features / Improvements	Removal Efficiency	Reference
TiO_2/Analcime zeolite	Methyl Orange	UV	High surface area, larger pore volume, uniform TiO_2 dispersion, more active sites	≈94.7 % removal of MO in 60 min	[50]
CuO/TiO_2/ZSM-5	Methyl Orange	UV/Visible	Defective ZSM-5: active sites & adsorption; CuO: electron trapping; extended visible-light absorption	≈99 % removal of MO in 60 min	[51]
Fe_3O_4@TiO_2@zeolite	Levofloxacin	Dark (adsorption)	Magnetic separation, high surface area, TiO_2 adsorption	≈96.5 % adsorption of levofloxacin	[52]
TiO_2/ZSM-5 (TZSM)	Sulfamethoxazole (SMX)	UV	Mechanical mixing, impregnation, improved mineralization	≈67 % SMX degradation within 120 min	[53]

Photocatalyst	Pollutant	Light Source	Key Features / Improvements	Removal Efficiency	Reference
Ag_2O@Y Zeolite	Ranitidine	Sunlight	Calcination, simultaneous adsorption & photocatalysis	Ag_2O–zeolite systems achieve ~97.51	[54]
TiO_2/Fe_2O_3/Zeolite	Cyanide	UV	Impregnation enhanced structural stability	≈89 % cyanide removal within 90 min	[55]
CuO/Ag-Zeolite	Methylene Blue	Dark (adsorption + antibacterial)	CuO/Ag modification, antibacterial	≈99 % MB adsorption in 30–60 min (dark)	[56]
ZSM-5/Flyash/TiO_2-Cu (This work)	Crystal violet	Visible/Solar light	Synergistic effect of Cu, porous ZSM-5, fly ash support, enhanced adsorption & light absorption	98% degradation under visible light	This work

5.0 Conclusion

In the present study ZSM-5-loaded fly ash-TiO_2-Cu (ZFT-Cu_1) composites was successfully synthesized using the wet impregnation method for the removal of Crystal Violet dye and characterized by XRD, FESEM, FTIR, UV-Vis DRS and BET analysis. The crystal violet (CV) dye was degraded by this catalyst under visible and solar light irradiation. The modified composite catalyst (3ZFT-Cu_1) containing 3wt% ZSM-5 zeolite showed the best photocatalytic activity among all prepared catalysts with a maximum dye removal efficiency of 98% under visible light and 95% under solar light whereas the FT-Cu catalyst showed only 80% and 76% removal under visible and solar light, respectively. The integrated effects of Cu doping, the large surface area, porosity of fly ash, the higher crystallinity and light absorption caused by ZSM-5 inclusion are responsible for this increased efficiency. The catalyst loss was the major reason of the little decrease, yet even after five cycles, the composites maintained 84% removal efficiency. The Freundlich isotherms were found to have a better fit for the experimental data of adsorption than the Langmuir isotherm, indicating that multilayer adsorption is taking place. whereas the kinetic investigations demonstrated pseudo-first-order behaviour. Free radical production dominated the degradation route, as shown by scavenger experiments. The findings indicate that 3ZFT-Cu_1 composites serve as recyclable, stable, and effective photocatalysts

under visible and solar light, presenting an environmentally sustainable solution for treating wastewater contaminated with dyes.

Conclusion and Future prospects

The utilization of semiconductor-based photocatalysts for environmental remediation has gained considerable attention, and the present thesis focuses on advancing this concept through the development of sustainable, waste-derived materials. Fly ash–TiO_2 composites were first fabricated to exploit the synergistic benefits of a low-cost industrial by-product with a proven photocatalyst. The incorporation of fly ash enhanced the surface area, adsorption capacity, and dispersion of TiO_2, thereby improving pollutant–catalyst interaction and overall photocatalytic performance. To further extend the light absorption capability and suppress electron–hole recombination, copper was introduced into the TiO_2–fly ash framework. The Cu-modified composites exhibited significantly improved photocatalytic efficiency under visible and solar irradiation, confirming the role of metal loading in facilitating charge separation and broadening the photo-response region. Building upon this, ZSM-5 was incorporated into the Cu/TiO_2–fly ash system to create a multifunctional composite with superior porosity, enhanced adsorption–photocatalysis coupling, and better structural stability. The resulting ZSM-5–Cu/TiO_2–fly ash material demonstrated excellent dye removal efficiency, recyclability, and robustness, highlighting its strong potential as a cost-effective photocatalyst for wastewater treatment. Overall, this work establishes that the strategic integration of fly ash, metal modification, and porous supports such as ZSM-5 can significantly enhance photocatalytic activity, providing an environmentally friendly pathway for harnessing solar energy to degrade organic pollutants.

Future studies should focus on optimizing ZSM-5 and metal content to maximize adsorption–photocatalysis synergy, conducting long-term stability and regeneration tests, and performing pilot-scale experiments with real wastewater. In addition, advanced analytical techniques such as gas chromatography–mass spectrometry (GC–MS) should be employed to track degradation pathways and accurately identify intermediate species, providing deeper mechanistic insight. Further development of ternary or quaternary nanohybrids, along with their integration into continuous-flow or immobilized reactor systems, could translate these materials into robust,

scalable technologies for environmental remediation.

miss

ORIGINALITY REPORT

15%	%	15%	%
SIMILARITY INDEX	INTERNET SOURCES	PUBLICATIONS	STUDENT PAPERS

PRIMARY SOURCES

1	Mohd. Shkir, Atif M. Ali. "Novel 2D/3D BiOBr/TiO2 S-scheme heterostructures photocatalyst fabrication for remarkable ciprofloxacin degradation under solar light", FlatChem, 2025 Publication	<1%
2	Guanghui Li, Changye Mang, Lang Xing, Pengxu Cao, Yongfeng Cai, Jun Luo, Hao Jiang. "Surfactant-assisted synthesis of Mo-doped TiO2/FAC (fly ash cenosphere) for degradation of methylene blue dye under visible light irradiation", Colloids and Surfaces A: Physicochemical and Engineering Aspects, 2022 Publication	<1%
3	Rezika Bakri, Hakima Bozetine, Sabrina Aziri, Yacina Djebra, Nabila Berkane, Dyhia Aberkane, Toufik Hadjersi, Abdeltif Amrane. " Microwave synthesis of green /carbon nanocomposite with enhanced photocatalytic activity under and solar light ", Journal of the Chinese Chemical Society, 2025 Publication	<1%
4	G. León, F. García, B. Miguel, J. Bayo. "Equilibrium, kinetic and thermodynamic studies of methyl orange removal by adsorption onto granular activated carbon", Desalination and Water Treatment, 2015 Publication	<1%

5	Erdal Eren. "Adsorption Performance and Mechanism in Binding of Azo Dye by Raw Bentonite", CLEAN - Soil, Air, Water, 2010 Publication	<1%
6	R. Arunkumar, R. Venkataraghavan, K. Chithra. "A one-step facile synthesis of ZnO@fly ash from refuse-derived waste for adsorption-photocatalytic degradation of methylene blue", Cleaner Water, 2025 Publication	<1%
7	Haitao Lin, Waqed H. Hassan, Hayder A. Abbood, Sarminah Samad et al. "Designing a novel Ti3C2 MXene-bridged Z-scheme photocatalyst for effective H2 generation and removal of non-biodegradable norfloxacin: Optimization and mechanism insights", Journal of Alloys and Compounds, 2025 Publication	<1%
8	Savneet Kaur, Rajeev Jindal, Jaspreet Kaur Bhatia. "Synthesis and RSM-CCD optimization of microwave-induced green interpenetrating network hydrogel adsorbent based on gum copal for selective removal of malachite green from waste water", Polymer Engineering & Science, 2018 Publication	<1%
9	Khalid H. A. Elkhider, Ihsanullah Ihsanullah, Mukarram Zubair, Mohammad Saood Manzar et al. "Synthesis, Characterization and Dye Adsorption Performance of Strontium Ferrite decorated Bentonite-CoNiAl Magnetic Composite", Arabian Journal for Science and Engineering, 2020 Publication	<1%

10	Devagi Kanakaraju, Muhamad Hazim bin Ya, Ying-Chin Lim, Andrea Pace. "Combined Adsorption/Photocatalytic dye removal by copper-titania-fly ash composite", Surfaces and Interfaces, 2020 Publication	<1%
11	Bello, Olugbenga Solomon, Mohd Azmier Ahmad, and Banjo Semire. "Scavenging malachite green dye from aqueous solutions using pomelo (Citrus grandis) peels: kinetic, equilibrium and thermodynamic studies", Desalination and Water Treatment, 2014. Publication	<1%
12	Jhilly Dasgupta, Anuj Kumar, Dalia Dasgupta Mandal, Tamal Mandal, Siddhartha Datta. "Removal of phenol from aqueous solutions using adsorbents derived from low-cost agro-residues", Desalination and Water Treatment, 2015 Publication	<1%
13	Sushmita Banerjee, Ravindra Kumar Gautam, Puja Rai, Mahesh Chandra Chattopadhyaya. "Adsorptive removal of toxic dyes from aqueous phase using notorious weed Lantana camara (Linn.) as biosorbent", Research on Chemical Intermediates, 2016 Publication	<1%
14	Mohit Pathak, Olga Sacco, Antonietta Mancuso, Vincenzo Vaiano et al. "Enhanced photocatalytic degradation of organic pollutants in water by g-C3N4/N-TiO2/Y1.97SiO5:Ce0.03 heterostructure", Chemical Engineering Journal, 2025 Publication	<1%

15	M. Ghaedi, A. Amiri Pebdani, B. Sadeghian, R. Sahraei, A. Daneshfar, C. Duran. "SYNTHESIS AND CHARACTERIZATION OF CADMIUM SULFIDE NANOPARTICLE–LOADED ACTIVATED CARBON AS A NOVEL ADSORBENT FOR EFFICIENT REMOVAL OF REACTIVE ORANGE 12", Chemical Engineering Communications, 2013 Publication	<1%
16	Mobin Safarzadeh Khosrowshahi, Shiva Abdolhosein Hariri, Mohammad Rahimi, Hosein Banna Motejadded Emrooz, Farzaneh Shemirani. "Green synthesis of a ZnO/ZnS-decorated magnetic porous carbon hybrid for enhanced rhodamine B adsorption and photodegradation: A combined DFT and experimental study", Sustainable Materials and Technologies, 2025 Publication	<1%
17	Sadegh Karimi, Mohammad Javad Dianat, Atefeh Ghasemi, Ramon Martinez-Manez, Maryam Farrokhnia, Leila Abdollahi. "Efficient removal of Ofloxacin antibiotic from aqueous solution via CuCo modified Al-MCM-41: An experimental and theoretical study", Environmental Science: Nano, 2025 Publication	<1%
18	Kawan F. Kayani, Darya Sh. Hamad, Nian N. Mohammad, Sewara J. Mohammed, Harez Rashid Ahmed, Mohammed Ali Salih. "Uses, Toxicity, and Removal of Fuchsin Dye from Wastewater Using Low-Cost Adsorbents", Desalination and Water Treatment, 2025 Publication	<1%

19	Li, Haiyan, Jinfeng Liu, Junjie Qian, Qiuye Li, and Jianjun Yang. "Preparation of Bi-doped TiO2 nanoparticles and their visible light photocatalytic performance", Chinese Journal of Catalysis, 2014. Publication	<1%
20	Yang, Bo, Zhang Tian, Bin Wang, Zebin Sun, Li Zhang, Yaopeng Guo, Haizhen Li, and Shiqiang Yan. "Facile synthesis of Fe3O4/hierarchical-Mn3O4/graphene oxide as a synergistic catalyst for activation of peroxymonosulfate for degradation of organic pollutants", RSC Advances, 2015. Publication	<1%
21	Vadivel, S., V.P. Kamalakannan, Keerthi, and N. Balasubramanian. "d-Pencillamine assisted microwave synthesis of Bi2S3 microflowers/RGO composites for photocatalytic degradation—A facile green approach", Ceramics International, 2014. Publication	<1%
22	S. E. Agarry, O. O. Ogunleye, O. A. Ajani. "Biosorptive Removal of Cadmium (II) Ions from Aqueous Solution by Chemically Modified Onion Skin: Batch Equilibrium, Kinetic and Thermodynamic Studies", Chemical Engineering Communications, 2015 Publication	<1%
23	Surikumaran, Hemavathy, Sharifah Mohamad, and Norazilawati Sarih. "Molecular Imprinted Polymer of Methacrylic Acid Functionalised β-Cyclodextrin for Selective Removal of 2,4-Dichlorophenol", International Journal of Molecular Sciences, 2014. Publication	<1%

24	Baoting Tan, Jia Yan, Xujie Cao, Zhilong Song. "Enhanced Photocatalytic Degradation of Organic Pollutants Using Z-Scheme CN/WO3 Composites under Visible Light Irradiation", Ceramics International, 2025 Publication	<1 %
25	Liu, Z.. "Microemulsion synthesis, characterization of bismuth oxyiodine/titanium dioxide hybrid nanoparticles with outstanding photocatalytic performance under visible light irradiation", Applied Surface Science, 20120201 Publication	<1 %
26	V.O. Njoku, M. Asif, B.H. Hameed. "2,4-Dichlorophenoxyacetic acid adsorption onto coconut shell-activated carbon: isotherm and kinetic modeling", Desalination and Water Treatment, 2014 Publication	<1 %
27	Ardiansyah Taufik, Rosari Saleh. "Synergistic effect between ternary iron–zinc–copper mixed oxides and graphene for photocatalytic water decontamination", Ceramics International, 2017 Publication	<1 %
28	Masanori Hirano. "Photoactive and Adsorptive Niobium-Doped Anatase (TiO2) Nanoparticles: Influence of Hydrothermal Conditions on their Morphology, Structure, and Properties", Journal of the American Ceramic Society, 1/2006 Publication	<1 %
29	Tan, I.A.W.. "Enhancement of basic dye adsorption uptake from aqueous solutions using chemically modified oil palm shell	<1 %

activated carbon", Colloids and Surfaces A: Physicochemical and Engineering Aspects, 20080401
Publication

30 Xiaona Li, Hui Yuan, Xie Quan, Shuo Chen, Shijie You. "Effective adsorption of sulfamethoxazole, bisphenol A and methyl orange on nanoporous carbon derived from metal-organic frameworks", Journal of Environmental Sciences, 2018 <1%
Publication

31 Amkelwa Mpelane, David M. Katwire, Henry H. Mungondori, Pardon Nyamukamba, Raymond T. Taziwa. "Application of Novel C-TiO2-CFA/PAN Photocatalytic Membranes in the Removal of Textile Dyes in Wastewater", Catalysts, 2020 <1%
Publication

32 Muneeb Ur Rahman, Faiqa Nadeem, Muhammad Usman, Muhammad Shahzaib, Hina Ramzan, Nimra Nadeem, Zhiping Zhang, Nadeem Tahir. "Enhanced charge transferring through defects-mediated metal-carbon nanocomposites for efficient dye degradation under visible light", Journal of Water Process Engineering, 2025 <1%
Publication

33 Vanja Gilja, Zvonimir Katančić, Ljerka Kratofil Krehula, Vilko Mandić, Zlata Hrnjak-Murgić. "Efficiency of TiO2 catalyst supported by modified waste fly ash during photodegradation of RR45 dye", Science and Engineering of Composite Materials, 2019 <1%
Publication

34	Onal, Y.. "Elucidation of the naproxen sodium adsorption onto activated carbon prepared from waste apricot: Kinetic, equilibrium and thermodynamic characterization", Journal of Hazardous Materials, 20070930 Publication	<1 %
35	S. Sambakanya, P. Nyamukamba, D.M. Katwire, H.H. Mungondori, P. Mukumba, O. Okoh. "Synthesis and Application of Novel Coal Fly Ash Supported C-Doped TiO2-SnO2 Photocatalytic Nanocomposite for the Removal of Dyes in Water", Asian Journal of Chemistry, 2020 Publication	<1 %
36	Rabia Rehman, Muhammad Rashid, Mehwish Akram, Amara Dar, Zahrah T. Al-thagafi, Reem I. Alsantali, Maha E. Al-Hazemi. "Mechanistic study to enhance sorptive efficiency of Saussurea lappa lignocellulosic waste by chemical modification to detoxifying crystal violet dye by adsorption", International Journal of Biological Macromolecules, 2026 Publication	<1 %
37	A. Hashem. "Utilization of Sawdust-Based Materials as Adsorbent for Wastewater Treatment", Polymer-Plastics Technology and Engineering, 6/1/2006 Publication	<1 %
38	Kamal Kumar Paul, P. K. Giri. " Role of Surface Plasmons and Hot Electrons on the Multi-Step Photocatalytic Decay by Defect Enriched Ag@TiO Nanorods under Visible Light ", The Journal of Physical Chemistry C, 2017 Publication	<1 %

39	Varsha Yadav, Poorn Prakash Pande, Arbind Chaurasiya, Shailja Rai, Aradhana Chaudhary, Kopal Kashaudhan. "Fabrication and analysis of copper oxide–based hydrogel nanocomposite for the extraction of MB dye from wastewater", Colloid and Polymer Science, 2025 Publication	<1%
40	A.N. Ökte, D. Karamanis. "A novel photoresponsive ZnO-flyash nanocomposite for environmental and energy applications", Applied Catalysis B: Environmental, 2013 Publication	<1%
41	Reda M. Mohamed, Adel A. Ismail, Amal S. Basaleh, Huda A. Bawazir. "Controllable synthesis of PtO modified mesoporous Co3O4 nanocrystals as a highly effective photocatalyst for degradation of Foron Blue dye", Journal of Photochemistry and Photobiology A: Chemistry, 2022 Publication	<1%
42	Xu, H.. "Preparation and characterization of TiO"2 bulk porous nanosolids", Materials Letters, 200506 Publication	<1%
43	Renuka R. Gonte, Gauri Shelar, K. Balasubramanian. "Polymer–agro-waste composites for removal of Congo red dye from wastewater: adsorption isotherms and kinetics", Desalination and Water Treatment, 2013 Publication	<1%
44	Ruixue Fan, Funing Zhang, Luqi Wang, Yunqing Liu, Jinghua Liu. "One-step fabrication of C-modified TiO2 composite	<1%

photocatalysts for enhanced visible light photocatalytic performance", Results in Engineering, 2026
Publication

45 Asma S. Al-Wasidi, Fawaz A. Saad, Salwa AlReshaidan, Ahmed M. Naglah. "Facile Synthesis of ZSM-5/TiO2/Ni Novel Nanocomposite for the Efficient Photocatalytic Degradation of Methylene Blue Dye", Journal of Inorganic and Organometallic Polymers and Materials, 2022 <1 %
Publication

46 Venkatkarthick, R., D. J. Davidson, S. Ravichandran, S. Vengatesan, G. Sozhan, and S. Vasudevan. "Eco-friendly and facilely prepared silica modified amorphous titania (TiO2–SiO2) electrocatalyst for the O2 and H2 evolution reactions", Catalysis Science & Technology, 2015. <1 %
Publication

47 Yukun Zhong, Xueliang Mu, U Kei Cheang. "High-performance and selective adsorption of ZIF-8/MIL-100 hybrids towards organic pollutants", Nanoscale Advances, 2022 <1 %
Publication

48 Azmi, Nur Hidayah, Umi Fazara Md. Ali, Fahmi Muhammad Ridwan, Khairuddin Md Isa, Nurul Zufarhana Zulkurnai, and Mohamed Kheireddine Aroua. "Preparation of activated carbon using sea mango (Cerbera odollam) with microwave-assisted technique for the removal of methyl orange from textile wastewater", Desalination and Water Treatment, 2016. <1 %
Publication

49	E.A. Moawed, M.F. El-Shahat. "Equilibrium, kinetic and thermodynamic studies of the removal of triphenyl methane dyes from wastewater using iodopolyurethane powder", Journal of Taibah University for Science, 2018 Publication	<1%
50	Fangyu Gan, Zhenpeng Li, Qingrong Yao, Shasha Jiang et al. "Modulating polarization and conduction loss for optimized electromagnetic wave absorption performance of FeNi/ZnO/C/Ni3ZnC0.7 composites", Chemical Engineering Journal, 2024 Publication	<1%
51	S. Alfadhli, Syed Khasim, A.A.A. Darwish, Khoulod Al-nahdi, Mervat Abdelkader, Raghad Gamal, Taymour A. Hamdalla. "Facile green synthesis of silver doped NiO nanoparticles using aloe vera latex for efficient energy storage and photocatalytic applications", Heliyon, 2025 Publication	<1%
52	Suzuki, Y.. "Removal of heavy metals from aqueous solution by nonliving Ulva seaweed as biosorbent", Water Research, 200505 Publication	<1%
53	Darshan Malik, Nandita Narayanasamy, V A Pratyusha. "Essential Laboratory Techniques and Biochemical Analysis", CRC Press, 2025 Publication	<1%
54	Syieluing Wong, Nurul Atiqah Najlaa Yac'cob, Norzita Ngadi, Onn Hassan, Ibrahim M. Inuwa. "From pollutant to solution of wastewater pollution: Synthesis of activated carbon from textile sludge for dye	<1%

adsorption", Chinese Journal of Chemical Engineering, 2017
Publication

55	A. Suguna, C. Sridevi, M. Parthibavarman, C.S. Manikandababu, K. Ramachandran, R. BoopathiRaja. "Design and fabrication of Zeolite Socony Mobil-5 incorporated ZnO composite for enhanced visible light photocatalytic performance", Chemical Physics Impact, 2024 Publication	<1 %
56	Huang, Ruihua, Qian Liu, Lujie Zhang, and Bingchao Yang. "Utilization of cross-linked chitosan/bentonite composite in the removal of methyl orange from aqueous solution", Water Science & Technology, 2015. Publication	<1 %
57	Leila Haroonabadi, Shahram Sharifnia. "Efficient photocatalytic water splitting of BiFeO3–BaTiO3 as a perovskite based n-n heterojunction toward H2 evolution without using sacrificial agent", International Journal of Hydrogen Energy, 2024 Publication	<1 %
58	Mawra Kokab, Ismat Bibi, Farzana Majid, Shagufta Kamal et al. "Solar light-based photocatalysis for organic pollutant degradation: Mechanistic understanding of double Z-scheme dynamics in ZnO/Fe2O3-doped NiCo2O4", Solar Energy, 2025 Publication	<1 %
59	Poonam Benjwal, Manish Kumar, Pankaj Chamoli, Kamal K. Kar. " Enhanced photocatalytic degradation of methylene blue and adsorption of arsenic( ) by reduced	<1 %

graphene oxide (rGO)–metal oxide (TiO /Fe O) based nanocomposites ", RSC Advances, 2015
Publication

60	Govindasamy Vijayakumar. "Removal of Congo Red from Aqueous Solutions by Perlite", CLEAN - Soil Air Water, 04/2009 Publication	<1 %
61	Jinlong Cui, Chengui Zhang, Yalong Li, Yang Liu, Weijun Jiang, Yuhui Wen, Zhenxi Wang, Zhonghua Yu, Xiangrong Ren, Zhifu Zhang. "Low-content Pt or Au loaded TiO2-CeO2 catalysts for efficient selective hydrogenation of cinnamaldehyde under UV and visible light", Applied Surface Science, 2026 Publication	<1 %
62	Manoj Kumar Sahu, Raj Kishore Patel. "Removal of safranin-O dye from aqueous solution using modified red mud: kinetics and equilibrium studies", RSC Advances, 2015 Publication	<1 %
63	Ali Hashem, Hussein Ahmed Hussein, Mansour Ahmed Sanousy, Ebtisam Adam, Elhady Elbay Saad. "Monomethylolated Thiourea – Sawdust as a New Adsorbent for Removal of Hg (II) from Contaminated Water: Equilibrium Kinetic and Thermodynamic Studies", Polymer-Plastics Technology and Engineering, 2011 Publication	<1 %
64	Iqra Liaquat, Ruba Munir, Naseer Ahmed Abbasi, Bushra Sadia et al. "Exploring zeolite-based composites in adsorption and photocatalysis for toxic wastewater treatment: Preparation, mechanisms, and	<1 %

future perspectives", Environmental Pollution, 2024
Publication

65	Muhammad Imran Din, Umar Farooq, Makshoof Athar, M. Latif Mirza. " Environmentally benevolent urea modified as a high capacity biosorbent for removal of Pb(II) ions: metal uptake modeling and adsorption efficiency ", Desalination and Water Treatment, 2013 Publication	<1%
66	Nilay Baylan, İrem İlalan, İsmail İnci. "Copper Oxide Nanoparticles as a Novel Adsorbent for Separation of Acrylic Acid from Aqueous Solution: Synthesis, Characterization, and Application", Water, Air, & Soil Pollution, 2020 Publication	<1%
67	Eren, Z.. "Equilibrium and kinetic mechanism for Reactive Black 5 sorption onto high lime Soma fly ash", Journal of Hazardous Materials, 20070508 Publication	<1%
68	Minbeom Kim, Hyeonseo Kim, Jaehyun Byun, Eunmok Yang, Heechul Choi. "Gravity-driven removal of tetracycline from water using a hierarchically porous adsorptive nanofibrous membrane system functionalized with metal–organic framework", Water Research, 2026 Publication	<1%
69	Mohd Rafatullah, Othman Sulaiman, Rokiah Hashim, Anees Ahmad. "Removal of cadmium (II) from aqueous solutions by adsorption using meranti wood", Wood Science and Technology, 2010 Publication	<1%

70	S. Kavitha, R. Selvakumar, K. Swaminathan. "Polyvinyl Pyrrolidone K25 Modified Fungal Biomass as Biosorbent for As(V) Removal from Aqueous Solution", Separation Science and Technology, 2008 Publication	<1 %
71	Yuan, S.. "Synthesis of thermally stable mesoporous TiO"2 and investigation of its photocatalytic activity", Microporous and Mesoporous Materials, 20080415 Publication	<1 %
72	Z. İlbay, S. Şahin, Ö. Kerkez, Ş. S. Bayazit. "Isolation of naproxen from wastewater using carbon-based magnetic adsorbents", International Journal of Environmental Science and Technology, 2015 Publication	<1 %
73	Linyuan Lian, Xi Wang, Peng Zhang, Jinsong Zhu et al. "Highly Luminescent Zero-Dimensional Organic Copper Halides for X-ray Scintillation", The Journal of Physical Chemistry Letters, 2021 Publication	<1 %
74	Muhammad Shafiq, Abdulrahman Ali Alazba, Muhammad Tahir Amin. "Eco-friendly nanocomposite of manganese-iron and plant waste derived biochar for optimizing Pb2+ adsorption: A response surface methodology approach", Desalination and Water Treatment, 2025 Publication	<1 %
75	Shamik Chowdhury, Papita Saha. "Adsorption Thermodynamics and Kinetics of Malachite Green onto Ca(OH)2-Treated Fly Ash", Journal of Environmental Engineering, 2011	<1 %

Publication

76	Shumaila Fatima, Mahwish Iqbal, Haq Nawaz Bhatti, Norah Alwadai, Maryam Al Huwayz, Arif Nazir, Munawar Iqbal. "Kinetics and thermodynamics studies of nickel manganite nanoparticle as photocatalyst and fuel additive", Heliyon, 2024 Publication	<1 %
77	Alaa A. Mizhir, Ali A. Abdulwahid, Hadi S. Al-Lami. "Adsorption of carcinogenic dye Congo red onto prepared graphene oxide-based composites", Desalination and Water Treatment, 2020 Publication	<1 %
78	Ghorai, T.K.. "Photocatalytic oxidation of organic dyes by nano-sized metal molybdate incorporated titanium dioxide (M"xMo"xTi"1"-"xO"6) (M=Ni, Cu, Zn) photocatalysts", Journal of Molecular Catalysis. A, Chemical, 20070801 Publication	<1 %
79	Jamal Mabrouki. "Integration of Advanced Systems in Environmental Science and Water Desalination", CRC Press, 2026 Publication	<1 %
80	M.O. Aremu, A.O. Arinkoola, I.A. Olowonyo, K.K. Salam. "Improved phenol sequestration from aqueous solution using silver nanoparticle modified Palm Kernel Shell Activated Carbon", Heliyon, 2020 Publication	<1 %
81	Maciej Fronczak, Przemysław Strachowski, Waldemar Kaszuwara, Michał Bystrzejewski. "Magnetic composite adsorbents of phenolic compounds with superior corrosion	<1 %

resistance", Separation Science and Technology, 2018
Publication

82 Patricio Paredes, Erwan Rauwel, David Stephen Wragg, Laetitia Rapenne, Isabelle Gélard, Protima Rauwel. "A comparative study of Cu-based nanoparticles and their spin-coated films: photocatalytic degradation mechanisms and efficiencies towards malachite green and neutral red azo dyes", Environmental Science and Pollution Research, 2024 <1%
Publication

83 Tong, T.. "Preparation of Ce-TiO"2 catalysts by controlled hydrolysis of titanium alkoxide based on esterification reaction and study on its photocatalytic activity", Journal of Colloid And Interface Science, 20071101 <1%
Publication

84 Chairat, M.. "An adsorption and kinetic study of lac dyeing on silk", Dyes and Pigments, 200503 <1%
Publication

85 Jayaraja Silvaraja, Noor Yahida Yahya, Muzakkir Mohammad Zainol, Yong Siang Lee. "Preliminary investigations of sustainable magnetic catalyst-based biochar derived spent coffee ground for biodiesel production from waste cooking oil", Cleaner Chemical Engineering, 2025 <1%
Publication

86 Savneet Kaur, Rajeev Jindal. "Synthesis of interpenetrating network hydrogel from (Gum Copal alcohols-collagen)-co-poly(acrylamide) and acrylic acid: Isotherms and Kinetics study <1%

for removal of methylene blue dye from aqueous solution", Materials Chemistry and Physics, 2018
Publication

87 Ur Rehman, Muhammad Saif, Ilgook Kim, Naim Rashid, Malik Adeel Umer, Muhammad Sajid, and Jong-In Han. "Adsorption of Brilliant Green dye on biochar prepared from lignocellulosic bioethanol plant waste", CLEAN - Soil Air Water, 2015. <1%
Publication

88 Van Hai Nguyen, Van Chien Nguyen, Thuy Chinh Nguyen, Do Mai Trang Tran et al. "Treatment of Yellow Phosphorus Slag and Reuse of It as an Absorbent of Chromium (VI) Ions and Methylene Blue", Journal of Chemistry, 2020 <1%
Publication

89 Zhang, W.. "Microwave hydrothermal synthesis and photocatalytic activity of AgIn"5S"8 for the degradation of dye", Journal of Solid State Chemistry, 201010 <1%
Publication

90 Zhenfei Fu, Wenmei Ma, Shiwen Du, Shilong Suo, Yuanyuan Li, Ziwu Han, Yumin Wang, Jiapeng Fang, Hu Xu, Pengfei Fang. "Regulating carrier transport in dual Z-scheme heterojunction KNbO3/MoSe2/Zn2In2S5 by dual piezoelectric polarization electric field", Applied Surface Science, 2026 <1%
Publication

91 A. Niyogi, J. K. Pati, M. K. Panigrahi, D. Panda, M. Chakarvorty, G. Parthasarathy. "Raman, Infrared, and Chemical Characterization of Fly <1%

Ash-Generated Spherules", Journal of Applied Spectroscopy, 2018
Publication

92	A.A. Hebeish, M.M. Abdelhady, A.M. Youssef. "TiO2 nanowire and TiO2 nanowire doped Ag-PVP nanocomposite for antimicrobial and self-cleaning cotton textile", Carbohydrate Polymers, 2013 Publication	<1 %
93	Cheng, W.. "Removal of malachite green (MG) from aqueous solutions by native and heat-treated anaerobic granular sludge", Biochemical Engineering Journal, 20080501 Publication	<1 %
94	Qingxiang Yang, Ran Lu, ShuangShuang Ren, Congtao Chen, Zhijun Chen, Xiaoyan Yang. "Three dimensional reduced graphene oxide/ZIF-67 aerogel: effective removal cationic and anionic dyes from water", Chemical Engineering Journal, 2018 Publication	<1 %
95	Samir El Atouani, Zahira Belattmania, Abdeltif Reani, Soufiane Tahiri et al. "Brown Seaweed Sargassum muticum as Low-Cost Biosorbent of Methylene Blue", International Journal of Environmental Research, 2018 Publication	<1 %
96	Santosh Arade, Sagar Balgude, Jitendra Kounsalye, Dattatray Hingane, Paresh More. "Magnetically separable Cu0.5Ni0.5MnFeO4@GO nanocomposites for efficient methylene blue removal", Journal of Materials Science: Materials in Electronics, 2024 Publication	<1 %

97 Xiu Wang, Kai Huang, Ying Chen, Jiafa Liu, Shan Chen, Jianlei Cao, Surong Mei, Yikai Zhou, Tao Jing. "Preparation of dumbbell manganese dioxide/gelatin composites and their application in the removal of lead and cadmium ions", Journal of Hazardous Materials, 2018 <1%
Publication

98 Yan Ma, Zhihuan Zhao, Jimin Fan, Zhanyong Gu, Bin Zhang, Shu Yin. "Ag-TON nanospheres coupled with fly ash cenospheres for wastewater treatment under visible light irradiation", Water Science and Technology, 2018 <1%
Publication

99 Yari, Saeed, Saeed Abbasizadeh, Seyyed Ebrahim Mousavi, Mojtaba Saei Moghaddam, and Abdolsamad Zarringhalam Moghaddam. "Adsorption of Pb(II) and Cu(II) ions from aqueous solution by an electrospun CeO2 nanofiber adsorbent functionalized with mercapto groups", Process Safety and Environmental Protection, 2015. <1%
Publication

100 Yinhua Jiang, Leiqun Guo, Wenli Zhang, Fei Dai, Yun Yan, Fumei Zhang, Hongyan Lv. " Preparation of zinc tetraaminophthalocyanine sensitized TiO hollow nanospheres and their enhanced photocatalytic properties under visible light ", Desalination and Water Treatment, 2013 <1%
Publication

101 Zhou, Hui, Yan Fang Feng, Yong Hong Wu, and Lin Zhang Yang. "Mung Bean Shell (*Vigna radiata* L. Wilczek) - A Novel Cost-Effective <1%

Adsorbent for Removing Methylene Blue from Aqueous Solutions", Advanced Materials Research, 2012.
Publication

---

102 A. Muthukrishnaraj, J. Manokaran, M. Vanitha, K.V. Thiruvengadaravi, P. Baskaralingam, N. Balasubramanian. " Equilibrium, kinetic and thermodynamic studies for the removal of Zn(II) and Ni(II) ions using magnetically recoverable graphene/Fe O composite ", Desalination and Water Treatment, 2014 <1 %
Publication

---

103 Aksu, Z.. "Investigation of biosorption of Gemazol Turquise Blue-G reactive dye by dried Rhizopus arrhizus in batch and continuous systems", Separation and Purification Technology, 200602 <1 %
Publication

---

104 Aydin, H.. "Adsorption of acid dyes in aqueous solutions by shells of bittim (Pistacia khinjuk Stocks)", Desalination, 20060905 <1 %
Publication

---

105 Balkaya, Nilgün, and Hasan Cesur. "A kinetic study on cadmium adsorption from aqueous solutions by pre-conditioned phosphogypsum", Desalination and Water Treatment, 2015. <1 %
Publication

---

106 Lanting Wang, Yanhua Xie, Jinglong Yang, Xueqian Zhu, Qili Hu, Xiaoyun Li, Zhuang Liu. "Insight into mechanisms of fluoride removal from contaminated groundwater using lanthanum-modified bone waste", RSC Advances, 2017 <1 %
Publication

107	Meriem Belhachemi, Fatima Addoun. "Comparative adsorption isotherms and modeling of methylene blue onto activated carbons", Applied Water Science, 2011 Publication	<1 %
108	Ming Ge. "Photocatalytic degradation of methyl orange using ZnO/TiO2 composites", Frontiers of Environmental Science & Engineering in China, 09/2009 Publication	<1 %
109	Pravesh Ravi, Jitendra Kumar Katiyar, C Shravan Kumar. "Wear and Corrosion Performance of Nickel Phosphorous/Nickel Boron Nano Composite Duplex Coating", Tribology International, 2025 Publication	<1 %
110	S. K. Mehta, J. P. Gaur. "Use of Algae for Removing Heavy Metal Ions From Wastewater: Progress and Prospects", Critical Reviews in Biotechnology, 2008 Publication	<1 %
111	Sen, Sudip Kumar, Madan Mohan Das, Partha Bandyopadhyay, R.R. Dash, and Sangeeta Raut. "Green process using hot spring bacterium to concentrate alumina in coal fly ash", Ecological Engineering, 2016. Publication	<1 %
112	Xiaowang Lu. "Photocatalytic Nanomaterials for Environmental Purification", Catalysts, 2025 Publication	<1 %
113	Dongqiu Zhao, Xiaowei Huang, Baoli Tian, Shaomin Zhou, Yuncai Li, Zuliang Du. "The effect of electronegative difference on the electronic structure and visible light	<1 %

photocatalytic activity of N-doped anatase TiO2 by first-principles calculations", Applied Physics Letters, 2011
Publication

---

114 Ferrero, F.. "Dye removal by low cost adsorbents: Hazelnut shells in comparison with wood sawdust", Journal of Hazardous Materials, 20070402
Publication

<1 %

---

115 Harshala Parab. "Use of Agro-Industrial Wastes for Removal of Basic Dyes from Aqueous Solutions", CLEAN - Soil Air Water, 12/2009
Publication

<1 %

---

116 Khraisheh, M.A.M.. "Effect of OH and silanol groups in the removal of dyes from aqueous solution using diatomite", Water Research, 200503
Publication

<1 %

---

117 Luminita Andronic, Luminita Isac, Sara Miralles-Cuevas, Maria Visa, Isabel Oller, Anca Duta, Sixto Malato. "Pilot-plant evaluation of TiO2 and TiO2-based hybrid photocatalysts for solar treatment of polluted water", Journal of Hazardous Materials, 2016
Publication

<1 %

---

118 M.J. Ahmed, Md. Azharul Islam, M. Asif, B.H. Hameed. "Human hair-derived high surface area porous carbon material for the adsorption isotherm and kinetics of tetracycline antibiotics", Bioresource Technology, 2017
Publication

<1 %

---

119 Ruksana Sirach, Pragnesh N. Dave. "Artificial neural network modelling and experimental

<1 %

investigations of malachite green adsorption on novel carboxymethyl cellulose/β-cyclodextrin/nickel cobaltite composite", Heliyon, 2024
Publication

120 WANG, H.. "Bioaccumulation of heavy metals by Phragmites australis cultivated in synthesized substrates", Journal of Environmental Sciences, 2009 <1%
Publication

121 Yoldaş Seki, Kadir Yurdakoç. "Adsorption of Promethazine hydrochloride with KSF Montmorillonite", Adsorption, 2006 <1%
Publication

122 Ahmed El Nemr. "Pomegranate husk as an adsorbent in the removal of toxic chromium from wastewater", Chemistry and Ecology, 2007 <1%
Publication

123 K. Ahmadi, M. Ghaedi, A. Ansari. "Comparison of nickel doped Zinc Sulfide and/or palladium nanoparticle loaded on activated carbon as efficient adsorbents for kinetic and equilibrium study of removal of Congo Red dye", Spectrochimica Acta Part A: Molecular and Biomolecular Spectroscopy, 2015 <1%
Publication

124 Rozada, F.. "Activated carbons from sewage sludge and discarded tyres: Production and optimization", Journal of Hazardous Materials, 20050930 <1%
Publication

125 C. Namasivayam, R. T. Yamuna, D. J. S. E. Arasi. "Removal of procion orange from <1%

wastewater by adsorption on waste red mud", Separation Science and Technology, 2002
Publication

126 Jenny D. Nerona, Nekah Celine M. Abella, Ghalib Al-Ghazie C. Jundam, Rey P. Gumaling. "Response surface and artificial neural network modeling for optimization of process parameter in Cu(II) adsorption uptake of sodium-activated Philippine natural zeolite", Journal of Water Process Engineering, 2024 <1%
Publication

127 Alila, S.. "Sorption potential of modified nanocrystals for the removal of aromatic organic pollutant from aqueous solution", Industrial Crops & Products, 201103 <1%
Publication

128 Ezechi, Ezerie Henry, Shamsul Rahman bin Mohamed Kutty, Amirhossein Malakahmad, and Mohamed Hasnain Isa. "Characterization and optimization of effluent dye removal using a new low cost adsorbent: Equilibrium, kinetics and thermodynamic study", Process Safety and Environmental Protection, 2015. <1%
Publication

129 A. Hameed, Iqbal M.I. Ismail, M. Aslam, M.A. Gondal. "Photocatalytic conversion of methane into methanol: Performance of silver impregnated WO3", Applied Catalysis A: General, 2014 <1%
Publication

130 Baojun Jia, Wei Yang, Aili Zhang, Jiti Zhou. "Treatment of Nitrobenzene-Loaded Wastewater via Electrochemical Heterogeneous Catalytic Processes", 2009 3rd <1%

International Conference on Bioinformatics and Biomedical Engineering, 2009
Publication

131	Benshun Ma, Xiao Chen, Jianing Wang, Wei Xu, Lijian Song, Meng Gao, Juntao Huo, Jun-Qiang Wang. "High thermal stability of amorphous TiO2 enhanced by OH", Journal of Non-Crystalline Solids, 2025 Publication	<1 %
132	Cristina-Veronica Gherasim, Gelu Bourceanu, Daniel Timpu. "Experimental and modeling studies of lead (II) sorption onto a polyvinyl-chloride inclusion membrane", Chemical Engineering Journal, 2011 Publication	<1 %
133	Hall, Joseph Karl. "Advancing Multi-Scale Network and Agent-Based Computational Lung Models: Potential for Personalized Prediction of Disease Progression", Boston University Publication	<1 %
134	Heo, Dong Uk, Joo Bin Lee, Yoon Deok Han, Jinsoo Joo, Hosuk Lee, Hosun Lee, and Dong Hoon Choi. "Self-Assembled Monolayers Made of 6-(5-((6-((5-hexylthiophen-2-yl)ethynyl)-9,10-bis(phenylethynyl)anthracen-2-yl)ethynyl)thiophen-2-yl)hexyl 3-(Triethoxysilyl)Propylcarbamate for Ultrathin Film Transistors", Langmuir, 2012. Publication	<1 %
135	Hu, J.. "Removal of 1-naphthylamine from aqueous solution by multiwall carbon nanotubes/iron oxides/cyclodextrin composite", Journal of Hazardous Materials, 20110115 Publication	<1 %

136	Jingfei Luan, Zhigang Zou, Minghui Lu, Guoyou Luan, Yanfeng Chen. "Structural and photocatalytic properties of the new solid photocatalyst In2BiTaO7", Research on Chemical Intermediates, 2006 Publication	<1 %
137	Lin, F.Q.. "In situ source-template-interface reaction route to hollow ZrO"2 microspheres with mesoporous shells", Journal of Colloid And Interface Science, 20080715 Publication	<1 %
138	Madhava Rao, M.. "Removal of copper and cadmium from the aqueous solutions by activated carbon derived from Ceiba pentandra hulls", Journal of Hazardous Materials, 20060228 Publication	<1 %
139	Nagwa Burham, Mahmoud Sayed. "Adsorption Behavior of Cd2+ and Zn2+ onto Natural Egyptian Bentonitic Clay", Minerals, 2016 Publication	<1 %
140	Onal, Y.. "Kinetics of adsorption of dyes from aqueous solution using activated carbon prepared from waste apricot", Journal of Hazardous Materials, 20061011 Publication	<1 %
141	Sen, T.K.. "Removal of cadmium metal ion (Cd^2^+) from its aqueous solution by aluminium oxide (Al"2O"3): A kinetic and equilibrium study", Chemical Engineering Journal, 20080901 Publication	<1 %

142	Sibel Tunali, Adnan Ozcan, Zerrin Kaynak, A. Safa Ozcan, Tamer Akar. " Utilization of the L. Waste biomass for decolorization of the textile dye Acid Red 57: determination of equilibrium, kinetic and thermodynamic parameters ", Journal of Environmental Science and Health, Part A, 2007 Publication	<1 %
143	Asem A. Atia, Ahmed M. Donia, Rashad A. Hussien, Rama T. Rashad. "Efficient adsorption of malathion from different media using thermally treated kaolinite", Desalination and Water Treatment, 2012 Publication	<1 %
144	Auttawit Thoumrungroj, Suchalee Wongtongprapun, Soontorn Tuntithavornwat, Chonticha Saisawang et al. "Photocatalytic Gold Recovery from Industrial Gold Plating Effluent by ZnO Nanoparticles: Optimum Condition and Possible Applications", ACS Omega, 2023 Publication	<1 %
145	Banerjee, S.S.. "Effect of quaternary ammonium cations on dye sorption to fly ash from aqueous media", Journal of Colloid And Interface Science, 20061115 Publication	<1 %
146	Bangda Wang, Yuexi Zhou, Lei Li, Hui Xu, Yinglong Sun, Yunsan Du, Yi Wang. " In Situ Synthesis of TiO -Doped Mesoporous Silica from Coal Fly Ash for the Photocatalytic Degradation of Dyes ", Industrial & Engineering Chemistry Research, 2018 Publication	<1 %

147 Brice Takam, Elie Acayanka, Georges Y. Kamgang, Merlin T. Pedekwang, Samuel Laminsi. "Enhancement of sorption capacity of cocoa shell biomass modified with non-thermal plasma for removal of both cationic and anionic dyes from aqueous solution", Environmental Science and Pollution Research, 2017 <1%
Publication

148 Bulut, Y.. "A kinetics and thermodynamics study of methylene blue adsorption on wheat shells", Desalination, 20060610 <1%
Publication

149 Darshana Morankar, Kajal Barhate, Navnath Hatvate. "ZSM-5 zeolite: Structural features, catalytic properties, and multidisciplinary applications in organic synthesis, material science, and environmental remediation", Coordination Chemistry Reviews, 2026 <1%
Publication

150 Doulati Ardejani, F.. "Adsorption of Direct Red 80 dye from aqueous solution onto almond shells: Effect of pH, initial concentration and shell type", Journal of Hazardous Materials, 20080301 <1%
Publication

151 Lee, Lai Yee, Daniel Zhao Bing Chin, Xin Jiat Lee, Nishanth Chemmangattuvalappil, and Suyin Gan. "Evaluation of Abelmoschus esculentus (lady's finger) seed as a novel biosorbent for the removal of Acid Blue 113 dye from aqueous solutions", Process Safety and Environmental Protection, 2015. <1%
Publication

152	Moonis Ali Khan, Zeid Abdullah ALOthman, Mu. Naushad, Mohammad Rizwan Khan, Mohammad Luqman. "Adsorption of methylene blue on strongly basic anion exchange resin (Zerolit DMF): kinetic, isotherm, and thermodynamic studies", Desalination and Water Treatment, 2013 Publication	<1%
153	Sujaree Kaewgun. "Enhancing Photocatalytic Activity of Polymorphic Titania Nanoparticles by NMP Solvent-based Ambient Condition Process", Catalysis Letters, 07/2008 Publication	<1%
154	Tsai, W.T.. "Adsorption of organic compounds from aqueous solution onto the synthesized zeolite", Journal of Hazardous Materials, 20090730 Publication	<1%
155	Vimal Chandra Srivastava, Indra Deo Mall, Indra Mani Mishra. "Modelling Individual and Competitive Adsorption of Cadmium(II) and Zinc(II) Metal Ions from Aqueous Solution onto Bagasse Fly Ash", Separation Science and Technology, 2006 Publication	<1%
156	Wei, G.. "Controlled assembly of protein-protected gold nanoparticles on noncovalent functionalized carbon nanotubes", Carbon, 201003 Publication	<1%
157	Yaoji Tang, Dong Ma, Linhui Zhu. "Sorption Behavior of Methyl Violet onto Poly(acrylic acid-co-acrylamide)/Kaolin Hydrogel Composite", Polymer-Plastics Technology and Engineering, 2014	<1%

Publication

158 Ahlam I. Al-Sulami, Nuha Y. Elamin, Eman Aldosari, Yasmeen G. Abou El-Reash, M. O. Farea, E. M. Abdelrazek, A. Rajeh. " Enhanced Structural, Optical, and Electrical Properties of Polymer Composites Induced by Nanohybrids ", Polymer Engineering & Science, 2025 <1%
Publication

159 Altenor, S.. "Adsorption studies of methylene blue and phenol onto vetiver roots activated carbon prepared by chemical activation", Journal of Hazardous Materials, 20090615 <1%
Publication

160 Amit Bhatnagar, A. K. Minocha, Eva Kumar, Mika Sillanpää, Byong-Hun Jeon. " Removal of Phenolic Pollutants from Water Utilizing (Mango) Seed Waste and Cement Fixation ", Separation Science and Technology, 2009 <1%
Publication

161 Bao, Ningzhong, Liming Shen, and Kazumichi Yanagisawa. "Textural and Catalytic Properties of Combinational Micro-Mesoporous Octatitanate Fibers Prepared by Solvothermal Soft Chemical Process", The Journal of Physical Chemistry B, 2004. <1%
Publication

162 Ebbinghaus, S.G.. "Perovskite-related oxynitrides - Recent developments in synthesis, characterisation and investigations of physical properties", Progress in Solid State Chemistry, 200912 <1%
Publication

163 Fang, Yongling, Zhongyu Li, Song Xu, Dandan Han, and Dayong Lu. "Optical properties and photocatalytic activities of spherical ZnO and <1%

flower-like ZnO structures synthesized by facile hydrothermal method", Journal of Alloys and Compounds, 2013.
Publication

---

164 G ANNADURAI, R JUANG, D LEE. "Use of cellulose-based wastes for adsorption of dyes from aqueous solutions", Journal of Hazardous Materials, 2002 <1 %
Publication

---

165 J. Ru, H. J. Liu, J. H. Qu, A. M. Wang, R. H. Dai, Z. J. Wang. "Selective removal of organochlorine pesticides (OCPs) from aqueous solution by triolein-embedded composite adsorbent", Journal of Environmental Science and Health, Part B, 2007 <1 %
Publication

---

166 Jasmin Shah, Md. Rasul Jan, Md. Zeeshan, Mehwish Iqbal. "Solid phase extraction and removal of 2,4-dichlorophenol from aqueous samples using magnetic graphene nanocomposite", Separation Science and Technology, 2016 <1 %
Publication

---

167 Jiao Zhao, Qiang Huang, Meiying Liu, Yanfeng Dai, Junyu Chen, Hongye Huang, Yuanqing Wen, Xiaoli Zhu, Xiaoyong Zhang, Yen Wei. "Synthesis of functionalized MgAl-layered double hydroxides via modified mussel inspired chemistry and their application in organic dye adsorption", Journal of Colloid and Interface Science, 2017 <1 %
Publication

---

168 John Karuga, Yusufu A. C. Jande, Hee T. Kim, Cecil K. King'ondu. "Fish Swim Bladder-Derived Porous Carbon for Defluoridation at <1 %

Potable Water pH", Advances in Chemical Engineering and Science, 2016
Publication

169	Letícia G. da Trindade, Marcelo Assis, Josiane C. Souza, Aline B. Trench et al. "Improving the photocatalytic dye degradation performance and bactericidal properties of Brazilian Amazon Kaolin-waste by adding ZnO and Ag3PO4", Journal of Alloys and Compounds, 2024 Publication	<1 %
170	Li, Y.. "Characterization of natural sphalerite as a novel visible light-driven photocatalyst", Solar Energy Materials and Solar Cells, 200808 Publication	<1 %
171	Lu Jianbo, Sun Liping, Zhao Xinhua, Lu Bin, Li Yinlei, Zhang Lei. "Removal of Phosphate from Aqueous Solution Using Iron-Oxide-Coated Sand Filter Media: Batch Studies", 2009 International Conference on Environmental Science and Information Application Technology, 2009 Publication	<1 %
172	Mine Özdemir. "Recovery of boron from borax sludge using solid–liquid extraction followed by ion exchange with amberlite resin", Environmental Progress, 07/2007 Publication	<1 %
173	Nanfeng Zheng, Xianhui Bu, Hiep Vu, Pingyun Feng. "Open-Framework Chalcogenides as Visible-Light Photocatalysts for Hydrogen Generation from Water", Angewandte Chemie International Edition, 2005 Publication	<1 %

174	Ram Ashok Konale, Nilesh Keshavrao Mahale, Sopan Tukaram Ingle. "Nano-zeolite-graphene oxide composite for calcium hardness removal: isotherm and kinetic study", Water Practice and Technology, 2020 Publication	<1 %
175	Sajjad Khezrianjoo, Hosakere Doddarevanna Revanasiddappa. "Effect of operational parameters and kinetic study on the photocatalytic degradation of m-cresol purple using irradiated ZnO in aqueous medium", Water Quality Research Journal, 2016 Publication	<1 %
176	Saule Mergenbayeva, Zhanibek Abitayev, Milana Batyrbayeva, John Vakros et al. "TiO2/Zeolite Composites for SMX Degradation under UV Irradiation", Catalysts, 2024 Publication	<1 %
177	Tao Lv, Kexin Wei, Ting Wang, Xiao Wang, Zuguang Liu. "Synergistic catalysis for converting α-pinene to camphene via carbon-based solid acid derived from eucalyptus wood", Molecular Catalysis, 2025 Publication	<1 %
178	Thayyath S. Anirudhan, Priya Senan, Padmajan S. Suchithra. "Evaluation of Iron(III)-Coordinated Amino-Functionalized Poly(Glycidyl Methacrylate)-Grafted Cellulose for Arsenic(V) Adsorption from Aqueous Solutions", Water, Air, & Soil Pollution, 2011 Publication	<1 %
179	V Paramarta, A Taufik, R Saleh. " Magnetically Separable Fe O /SnO /Graphene Adsorbent for Waste Water Removal ", IOP Conference	<1 %

Series: Materials Science and Engineering, 2017
Publication

180	Yu, Mengqi. "Mixing and Segregation of Granular Flows in a 3D Tumbler", Northwestern University, 2020 Publication	<1 %
181	Zhu, L.. "Functionalized periodic mesoporous organosilicas for selective adsorption of proteins", Applied Surface Science, 20120701 Publication	<1 %
182	Cho, Y.. "Visible light-induced reactions of humic acids on TiO"2", Journal of Photochemistry & Photobiology, A: Chemistry, 20020531 Publication	<1 %
183	Daud Hussain, M. Fuzail Siddiqui, Tabrez A. Khan. " Preparation of NiFe O /polythiophene nanocomposite and its enhanced adsorptive uptake of Janus green B and Fuchsin basic from aqueous solution: Isotherm and kinetics studies ", Environmental Progress & Sustainable Energy, 2019 Publication	<1 %
184	Di Li, Yuan Zhang, Chunyan Gao, Qi Wen, Xinguo Ma, Fang Song, Jun Zhou. "Photocatalysis and peroxymonosulfate activation by dual Z-scheme g-C3N4/PDI/Co-Fe Prussian blue analogue for doxycycline hydrochloride removal", Journal of Environmental Chemical Engineering, 2025 Publication	<1 %
185	Doina Bilba, Nicolae Bilba, Gabriela Moroi. "Removal of Mercury (II) Ions from Aqueous Solutions by the Polyacrylamidoxime	<1 %

Chelating Fiber", Separation Science and Technology, 2007
Publication

186	Du, Xian, Hui Ling Du, Xiang Shi, Jin Wang, and Jiao Jiao He. "Photocatalytic Activity of Solar-Light-Active N-Doped TiO_2 by Sol-Gel Combustion Method", Materials Science Forum, 2014. Publication	<1 %
187	Fatemeh Donyagard, Ali Reza Zarei, Hadi Rezaei-Vahidian. "Application of magnetic carbon nanocomposites to remove melanoidin from aqueous media: kinetic and isotherm studies", Research on Chemical Intermediates, 2017 Publication	<1 %
188	Hardiljeet K. Boparai, Meera Joseph, Denis M. O'Carroll. "Kinetics and thermodynamics of cadmium ion removal by adsorption onto nano zerovalent iron particles", Journal of Hazardous Materials, 2011 Publication	<1 %
189	Jianjun Ding. "Synthesis of CaIn2O4 Rods and Its Photocatalytic Performance Under Visible-light Irradiation", Catalysis Letters, 06/2009 Publication	<1 %
190	Jing Zhang, Xuejiang Wang, Yunjie Bu, Xin Wang et al. "Remediation of diesel polluted water through buoyant sunlight responsive iron and nitrogen co-doped TiO 2 coated on chitosan carbonized fly ash", Chemical Engineering Journal, 2016 Publication	<1 %
191	Karima Derdour, Chafia Bouchelta, Amina Khorief Naser-Eddine, Mohamed Salah	<1 %

Medjram, Pierre Magri. "Removal of Cr(VI) from aqueous solutions by using activated carbon supported iron catalysts as efficient adsorbents", World Journal of Engineering, 2018
Publication

192 Kim, H.R.. "Preparation and photocatalytic properties of Cr/Ti hollow spheres", Materials Chemistry & Physics, 20080315 <1%
Publication

193 Kunlanan Kiatkittipong, Jason Scott, Rose Amal. "Hydrothermally Synthesized Titanate Nanostructures: Impact of Heat Treatment on Particle Characteristics and Photocatalytic Properties", ACS Applied Materials & Interfaces, 2011 <1%
Publication

194 Kustova, M.Yu.. "Direct NO decomposition over conventional and mesoporous Cu-ZSM-5 and Cu-ZSM-11 catalysts: Improved performance with hierarchical zeolites", Applied Catalysis B, Environmental, 20060911 <1%
Publication

195 Kyzas, George, and Eleni Deliyanni. "Mercury(II) Removal with Modified Magnetic Chitosan Adsorbents", Molecules, 2013. <1%
Publication

196 Lei Zuo, Ning Yang, Weiwei Xia, Xianghua Zeng, Rongxing Cao. "Z-scheme NiS@ZnCdS heterostructures and their boosted photocatalytic H2 evolution", Applied Surface Science, 2025 <1%
Publication

197 M. Salman Naeem, Saima Javed, Vijay Baheti, Jakub Wiener, M. Usman Javed, Syed Zameer <1%

Ul Hassan, Adnan Mazari, Jawad Naeem. "Adsorption Kinetics of Acid Red on Activated Carbon Web Prepared from Acrylic Fibrous Waste", Fibers and Polymers, 2018
Publication

198 Min Zhong, Qi Zeng, Xinyi Xie, Cuilian Zhu, Xiaoqin Ye, Lili Liu, Shupeng Guo, Pengju Yang. "Nanochannel-confined J-aggregates with spontaneous symmetry breaking for efficient red/near-infrared hydrogen production", Chemical Engineering Journal, 2025 <1%
Publication

199 Muhammad Zahid, Nimra Nadeem, Noor Tahir, Farid-Un-Nisa et al. "Hybrid nanomaterials for water purification", Elsevier BV, 2020 <1%
Publication

200 Naga Babu A., Krishna Mohan G.V., Kalpana K., Ravindhranath K.. "Removal of fluoride from water using H 2 O 2 -treated fine red mud doped in Zn-alginate beads as adsorbent", Journal of Environmental Chemical Engineering, 2018 <1%
Publication

201 Nagarethinam Kannan, Mariappan Meenakshi Sundaram. "Kinetics and mechanism of removal of methylene blue by adsorption on various carbons—a comparative study", Dyes and Pigments, 2001 <1%
Publication

202 Ohnuki, T.. "Mechanisms of uranium mineralization by the yeast Saccharomyces cerevisiae", Geochimica et Cosmochimica Acta, 20051115 <1%
Publication

203	Pankaj Chamoli, Tulika Srivastava, Alekha Tyagi, K.K. Raina, Kamal K. Kar. "Urea and cow urine-based green approach to fabricate graphene-based transparent conductive films with high conductivity and transparency", Materials Chemistry and Physics, 2020 Publication	<1%
204	Payal Maiti, B.C. Meikap. "Mechanism and adsorptive removal of Pb (II) by torrefied/pyrolyzed functionalized bio-adsorbent in batch application and life cycle assessment", Separation and Purification Technology, 2025 Publication	<1%
205	Prabhat Kumar Singh, Sushmita Banerjee, Arun Lal Srivastava, Yogesh Chandra Sharma. "Kinetic and equilibrium modeling for removal of nitrate from aqueous solutions and drinking water by a potential adsorbent, hydrous bismuth oxide", RSC Advances, 2015 Publication	<1%
206	Rais Ahmad, Khalid Ansari. "Enhanced sequestration of methylene blue and crystal violet dye onto green synthesis of pectin modified hybrid (Pect/AILP-Kal) nanocomposite", Process Biochemistry, 2021 Publication	<1%
207	S. Venkatesan, S. Suresh, J. Arumugam, P. Ramu, N. Pugazhenthiran, R. Jothilakshmi, K.M. Prabu. "Sunlight assisted degradation of methylene blue dye by zinc oxide nanoparticles green synthesized using Vitex negundo plant leaf extract", Results in Chemistry, 2024 Publication	<1%

208 Shaozheng Hu, Anjie Wang, Xiang Li, Yao Wang, Holger Löwe. "Hydrothermal Synthesis of Ionic Liquid [Bmim]OH-Modified TiO2 Nanoparticles with Enhanced Photocatalytic Activity under Visible Light", Chemistry - An Asian Journal, 2010 <1%
Publication

209 Shi, L.n.. "Removal of Chromium (VI) from wastewater using bentonite-supported nanoscale zero-valent iron", Water Research, 201101 <1%
Publication

210 Sunil G. Shelar, Vilas K. Mahajan, Sandip P. Patil, Gunvant H. Sonawane. "Effect of doping parameters on photocatalytic degradation of methylene blue using Ag doped ZnO nanocatalyst", SN Applied Sciences, 2020 <1%
Publication

211 Wassana Yantasee. "Removal of Heavy Metals from Aqueous Solution Using Novel Nanoengineered Sorbents: Self-Assembled Carbamoylphosphonic Acids on Mesoporous Silica", Separation Science and Technology, 1/10/2003 <1%
Publication

212 Weiren Dai, Pan Luo, Bo Xu, Guihong Lan, Haiyan Qiu, Teng Zhang. "Efficient removal of chlorpyrifos from water using acrylic resin P(MA-SMA-St): Adsorption behavior, kinetics, thermodynamics, molecular simulations, and DFT calculations", Journal of Environmental Chemical Engineering, 2025 <1%
Publication

213 Weng, C.H.. "Adsorption characteristics of copper(II) onto spent activated clay", <1%

Separation and Purification Technology, 20070401
Publication

214 Zengyu Yao. "Biosorption of Methylene Blue from Aqueous Solution Using a Bioenergy Forest Waste: *Xanthoceras sorbifolia* Seed Coat", CLEAN - Soil Air Water, 08/05/2009 <1%
Publication

215 Akpan, U.G.. "The advancements in solgel method of doped-TiO"2 photocatalysts", Applied Catalysis A, General, 20100226 <1%
Publication

216 Ashwani Kumar Sahu, Indra Deo Mall, Vimal Chandra Srivastava. "STUDIES ON THE ADSORPTION OF FURFURAL FROM AQUEOUS SOLUTION ONTO LOW-COST BAGASSE FLY ASH", Chemical Engineering Communications, 2007 <1%
Publication

217 Pandian Ganesan, Jothinathan Lakshmi, Ganapathy Sozhan, Subramanyan Vasudevan. "Removal of manganese from water by electrocoagulation: Adsorption, kinetics and thermodynamic studies", The Canadian Journal of Chemical Engineering, 2013 <1%
Publication

218 R. Daghrir, P. Drogui, D. Robert. "Photoelectrocatalytic technologies for environmental applications", Journal of Photochemistry and Photobiology A: Chemistry, 2012 <1%
Publication

219 Afkhami, A.. "Modified maghemite nanoparticles as an efficient adsorbent for <1%

removing some cationic dyes from aqueous solution", Desalination, 20101130
Publication

220	B. K. Nandi, A. Goswami, A. K. Das, B. Mondal, M. K. Purkait. "Kinetic and Equilibrium Studies on the Adsorption of Crystal Violet Dye using Kaolin as an Adsorbent", Separation Science and Technology, 2008 Publication	<1 %
221	Hasnain Isa, M.. "Low cost removal of disperse dyes from aqueous solution using palm ash", Dyes and Pigments, 2007 Publication	<1 %
222	Khadije Badvi, Vahid Javanbakht. "Enhanced photocatalytic degradation of dye contaminants with TiO2 immobilized on ZSM-5 zeolite modified with nickel nanoparticles", Journal of Cleaner Production, 2021 Publication	<1 %
223	Lin, Lin, Zhongfang Lei, Li Wang, Xiang Liu, Yi Zhang, Chunli Wan, Duu-Jong Lee, and Joo Hwa Tay. "Adsorption mechanisms of high-levels of ammonium onto natural and NaCl-modified zeolites", Separation and Purification Technology, 2013. Publication	<1 %
224	Nibedita Paul, Dambarudhar Mohanta. " Effective optoelectronic and photocatalytic response of Eu -doped TiO nanoscale systems synthesized via a rapid condensation technique ", Journal of Materials Research, 2013 Publication	<1 %
225	Srihari, V.. "Comparative studies on adsorptive removal of phenol by three agro-	<1 %

based carbons: Equilibrium and isotherm studies", Ecotoxicology and Environmental Safety, 200809
Publication

226 Yunhai Wu, Ligen Cha, Yiang Fan, Peng Fang, Zhu Ming, Haitao Sha. "Activated Biochar Prepared by Pomelo Peel Using H3PO4 for the Adsorption of Hexavalent Chromium: Performance and Mechanism", Water, Air, & Soil Pollution, 2017 <1%
Publication

Exclude quotes	Off	Exclude matches	< 3 words
Exclude bibliography	Off		

miss

GRADEMARK REPORT

FINAL GRADE

/0

GENERAL COMMENTS

PAGE 1

PAGE 2

PAGE 3

PAGE 4

PAGE 5

PAGE 6

PAGE 7

PAGE 8

PAGE 9

PAGE 10

PAGE 11

PAGE 12

PAGE 13

PAGE 14

PAGE 15

PAGE 16

PAGE 17

PAGE 18

PAGE 19

PAGE 20

PAGE 21

PAGE 22

PAGE 23

PAGE 24

PAGE 25

PAGE 26

PAGE 27

PAGE 28

PAGE 29

PAGE 30

PAGE 31

PAGE 32

PAGE 33

PAGE 34

PAGE 35

PAGE 36

PAGE 37

PAGE 38

PAGE 39

PAGE 40

PAGE 41

PAGE 42

PAGE 43

PAGE 44

PAGE 45

PAGE 46

PAGE 47

PAGE 48

PAGE 49

PAGE 50

PAGE 51

PAGE 52

PAGE 53

PAGE 54

PAGE 55

PAGE 56

PAGE 57

PAGE 58

PAGE 59

PAGE 60

PAGE 61

PAGE 62

PAGE 63

PAGE 64

PAGE 65

PAGE 66

PAGE 67

PAGE 68

PAGE 69

PAGE 70

PAGE 71

PAGE 72

PAGE 73

PAGE 74

PAGE 75

PAGE 76

PAGE 77

PAGE 78

PAGE 79

PAGE 80

PAGE 81

PAGE 82

PAGE 83

PAGE 84

PAGE 85

PAGE 86

PAGE 87

PAGE 88

PAGE 89

PAGE 90

PAGE 91

PAGE 92

PAGE 93

PAGE 94

PAGE 95

PAGE 96

PAGE 97

PAGE 98

PAGE 99

PAGE 100

PAGE 101

PAGE 102

PAGE 103

PAGE 104

PAGE 105

PAGE 106